DEVELOPMENT AND CHARACTERIZATION OF NOVEL REDUCTION-OXIDATION ACTIVE MATERIALS FOR TWO-STEP SOLAR THERMOCHEMICAL CYCLES

A Dissertation
Presented to
The Academic Faculty

by

H. Evan Bush

In Partial Fulfillment
of the Requirements for the Degree
Doctor of Philosophy in the
G. W. Woodruff School of Mechanical Engineering

Georgia Institute of Technology
August 2019

DEVELOPMENT AND CHARACTERIZATION OF NOVEL REDUCTION-OXIDATION ACTIVE MATERIALS FOR TWO-STEP SOLAR THERMOCHEMICAL CYCLES

Approved by:

Dr. Peter G. Loutzenhiser, Advisor (ME)
G. W. Woodruff School of Mechanical
Engineering
Georgia Institute of Technology

Dr. Thomas Orlando (CHEM)
School of Chemistry and Biochemistry
Georgia Institute of Technology

Dr. Sheldon Jeter (ME)
G. W. Woodruff School of Mechanical
Engineering
Georgia Institute of Technology

Dr. Devesh Ranjan (ME)
G. W. Woodruff School of Mechanical
Engineering
Georgia Institute of Technology

Dr. Satish Kumar (ME)
G. W. Woodruff School of Mechanical
Engineering
Georgia Institute of Technology

Date Approved: May 02, 2019

ACKNOWLEDGEMENTS

I thank my advisor, Dr. Peter Loutzenhiser, for his guidance and support throughout my graduate research. I also thank my committee members, Dr. Sheldon Jeter, Dr. Satish Kumar, Dr. Thomas Orlando, and Dr. Devesh Ranjan, for their consideration and advice during my thesis proposal and defense. To my colleagues and visiting researchers in the Solar Fuels and Technology Lab, Malavika Bagepalli, Ashley Clendenen, Gianmarco De Dominicis, Robby Gill, Iacopo Guscetti, Alex Muroyama, Garrett Schieber, Karl-Philipp Schlichting, Saverio Sparacio, and Justin Yarrington: your friendship and insights have improved my research and made this work even more rewarding and enjoyable. I thank Andrew Schrader for countless fascinating and insightful technical conversations throughout our five years in the lab. Finally, I thank my parents, my sister Micaela, and my fiancée Kara for their encouragement, support, and love, especially during my time at Georgia Tech. It is that which is most important, and without which the rest couldn't have occurred.

for Lucille Bush

TABLE OF CONTENTS

LIST OF TABLES

LIST OF FIGURES

xiii

LIST OF SYMBOLS AND ABBREVIATIONS

A	undetermined constant, area
a	planar constant, semi-minor axes length
B	particle deformation parameter
b	planar constant, semi-minor axes length
C	solar concentration ratio (relative to 1 kW·m^{-2}), gas concentration
c	specific heat, planar constant, semi-minor axes length
d	diameter, differential change operator
D	maximum particle size for oxidation of magnetite to maghemite
E	residence time distribution
E_a	apparent activation energy
F	Fourier transform function operator, fractional function
f	kinetic model equation/conversion dependence, function operator
f_v	solid volume fraction
G	irradiation, molar Gibbs property/free enthalpy
H	molar enthalpy
h	kinetic O_2 pressure dependence, convective heat transfer coefficient
I	radiative intensity
$\bar{\bar{\mathbf{I}}}$	identity matrix
J	radiosity
k	rate constant/kinetic temperature dependence, conductivity
k_c	deformation-dependent term: porous media conductivity ratio
k_0	apparent pre-exponential/frequency factor
L	length, empirical sublattice interaction polynomial function
M	molar mass
$\bar{\bar{\mathbf{M}}}_{p \rightarrow t}$	projective transformation (mapping) matrix
m	mass, partial pressure-dependence rate constant
N	integer number
n	number of moles, Avrami-Erofe'ev rate constant, normal direction
Nu	Nusselt number
P	electrical power input
p	pressure, unknown model parameter
Pr	Prandtl number
Q	heat
Q_{ext}	extinction efficiency
r	reaction/temporal conversion rate, position, straight-line distance
r^2	coefficient of determination
R	random number, universal gas constant
Ra	Rayleigh number
S	molar entropy, source
SSE	sum of squared errors/residual sum of squares
T	temperature
t	time, coordinate direction, tangential direction

u	coordinate direction
V	volume, slab transmittance
W	work
x	nonstoichiometry, position
y	position, site fraction, B-site Al-dopant concentration
z	position

Greek Letters

α	conversion, absorptivity, hematite
β	TGA heating rate, scattering extinction coefficient
γ	maghemite, correction factor
Δ	spatial/temporal difference operator
δ	nonstoichiometry
∂	partial derivative operator
ε	emissivity
ζ	proportionality constant
η	efficiency
θ	angle, thermophysical property
κ	power-to-radiation conversion
λ	wavelength, Chi-squared random variable
μ	placeholder variable: particle conductivity ratio,
ν	sublattice stoichiometric coefficient
ξ	electric potential
ρ	density, reflectivity
σ	Stefan-Boltzmann constant, standard deviation
τ	space time, transmissivity
υ	stoichiometric coefficient
φ	N2 molar purity
$\chi 2$	Chi-squared distribution
ψ	azimuth angle
Ω	solid angle
ω	weighting factor

Subscripts

∞	equilibrium value, environment
0	environment/dead state (298.15 K and 1 bar), initial value
δ	partial derivative with respect to δ
air	air, approximated as a 21% O_2–N_2 concentration ideal gas mixture
c	camera
cavity	calorimeter cavity
Co_3O_4	cobalt(II,III) oxide
Coil	calorimeter cavity cooling coil
comp	cycle air compressor (for re-oxidizer) stage
conv	convection
CoO	cobalt(II) oxide/reduced Co_3O_4

cool	receiver outlet O2 cooling/quench stage
cool	receiver outlet O_2 cooling/quench stage
cycle	combined thermochemical and Air Brayton cycle
dep	dependent
diaphragm	calorimeter inner diaphragm surface
e	electrical
eff	total effective
eq	thermodynamic equilibrium
err	error
exhaust	air stream exiting turbine
exp	exposure
f	fluid
g	gas state
h	heat
H_2O	water
i	cell, general index variable, incoming, end member index variable
in	inlet
ind	independent
j	general index variable, fitted parameter index variable
k	summation index
L	length
loss	re-radiative and convective thermal losses
m	maximum
O_2	oxygen/sample bed evolved oxygen, value per mol O_2 produced
oct	octahedrally-configured
out	outlet
ox	oxidized
p	particle, pixel coordinates
pm	porous media
r	radiation, reflected, experimental measurement index variable
reactor	cycle solar receiver/reactor (reduction) stage
red	reduced
recover	Fe_2O_3/Fe_3O_4 particle stream exiting re-oxidizer
rerad	reradiation
s	solid, surface, specular, sample index variable
separator	cycle air separator (oxidation) stage
solar	solar input, solar reactor
step	step change value
surface	calorimeter outer surface
surr	surroundings
t	thermal, target coordinates
tet	tetrahedrally-configured
turbine	Air Brayton cycle turbine stage
vac	cycle vacuum pump (for solar receiver/reactor) stage
visible	visible wavelength spectrum
w	wall

Superscripts/Accents

$\hat{}$	unit vector, model estimate
$\circ$	degree, standard atmospheric conditions
$\cdot$	time rate of change
$'$	integration variable
$''$	flux
$'''$	volumetric term
$-$	vector, mean value
$=$	matrix
$*$	normalization
-1	inverse
2-, 4+, 3+	ionic charge/oxidation state
n	Redlich-Kister term order
p	timestep index
T	transpose
P	perovskite structure

Acronyms

AN	nth-order Avrami-Erofe'ev nucleation-limited model
CALPHAD	calculation of phase diagrams
CCD	charge-coupled device
CEF	compound energy formalism
CSP	concentrating solar power
CSTR	continuously-stirred tank reactor
DCNV	deconvolved array
DFT	density functional theory
FC	flow controller
FCC	face-centered cubic or cubic close-packed crystalline structure
GC	gas chromatography/chromatographer
HCP	hexagonal close-packed crystalline structure
HFSS	high-flux solar simulator
ID	inner diameter
MIEC	mixed ionic-electronic conductor
MCRT	Monte Carlo ray tracing
MS	mass spectrometry/spectrometer
ND	neutral density filter
OD	outer diameter
RTD	residence time distribution
SS	stainless steel
TC	thermocouple
TCES	thermochemical energy storage
TGA	thermogravimetric analysis/analyzer
UFR	upward flow reactor
XRD	X-ray diffractometry

SUMMARY

Solar thermochemistry enables concentrating solar technologies to store or produce energy and materials in new, more versatile ways. In this work, binary and perovskite metal oxide candidates for high-temperature reduction-oxidation (redox) thermochemical cycles were synthesized and characterized to determine their potential for solar applications.

First, the experimental infrastructure required to study rapidly reacting, high temperature metal oxides was developed. A high flux solar simulator (HFSS) capable of rapid heating was coupled to an upward flow reactor (UFR) to thermally reduce oxide samples, and O_2 product gas flows were measured to calculate thermal reduction rates. The radiative input from the HFSS was characterized and coupled to computational models of the UFR to predict gas dynamics and redox sample heating. Dispersion modeling was used to correct temporal O_2 measurements downstream of reducing samples. Thermal reduction experiments with the well-studied binary oxide pair Co_3O_4/CoO were performed to validate the computational models.

Next, the UFR and a thermogravimetric analyzer (TGA) were used to evaluate candidate materials. Fe_2O_3/Fe_3O_4 were kinetically characterized via TGA and evaluated in thermodynamic cycle models. The results suggested the oxides were promising candidates for solar thermochemical electricity production. Al-doped $SrFeO_{3-\delta}$ was synthesized and reaction models were developed with TGA to predict equilibrium nonstoichiometry and redox thermodynamics. The results were incorporated into a thermodynamic cycle model, and redox cycling experiments were performed in the UFR. The analyses determined that the oxides were well-suited to air separation for NH_3 production.

CHAPTER 1. INTRODUCTION

1.1   Motivation

Anthropogenic global warming presents a significant challenge to modern ways of life, and decreasing greenhouse gas (GHG) emissions sits at the forefront of current mitigation strategies. Modern renewable technologies, including solar electricity production, can address growing energy demands and reduce energy and transportation emissions [1-3], but they are not without obstacles. Three major deficiencies of the solar resource—*i.e.*, the sunlight incident on the earth's surface—are its relative diluteness, its unequal distribution, and its intermittencies due to local weather and the time of day.

Concentrated solar power (CSP) technologies can address the first of these deficiencies, by intensifying low terrestrial solar fluxes (1 kW·m^2) hundreds to thousands of times. Concentrating technologies can also address the second and third drawbacks of solar energy if they are unpaired from direct electric generation and instead used for solar thermochemical processes. Solar fuels (H_2 and CO), generated via H_2O/CO_2 splitting [1][4-7] or solar gasification of carbonaceous materials [2-4], can be stored and used on demand, or further processed to conventional, transportable liquid fuels by established catalytic processes [8]. Thermochemical energy storage (TCES) [9-11] captures sunlight in the bonds/potentials of chemical compounds and then releases it for off-sun electricity production. These processes effectively intermittency-proof and de-localize the solar resource, allowing it to be used around the clock and around the globe.

Significant greenhouse gas emissions (GHG) originate not just from the energy and transportation sectors, but from industry and agriculture as well. With solar thermochemistry, sunlight can be used to not only to produce and store energy, but also to perform chemical work and produce chemical products. Proposed processes include the solar thermochemical production of metals and metalloids [5, 6] and the separation of air to produce pure gases or nitrogen fertilizers [7].

Two-step solar thermochemical cycles based on reduction/oxidation (redox)-active materials, schematically depicted in Figure 1.1, are promising pathways for solar thermochemistry. The first, endothermic reduction step is described by the chemical equation:

$$MO_{ox} + \Delta H_{red} \rightarrow MO_{red} + \upsilon O_{2\,(g)} \qquad (1.1)$$
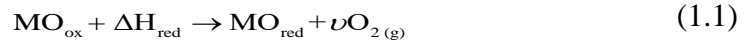
where υ is a stoichiometric coefficient, MO_{ox} is a metal oxide and MO_{red} is the compound at a lower oxidation state: another oxide or a pure metal. This reaction may be used for energy storage due to its endothermicity, or for the production of a metal product, sometimes with the aid of a reducing agent.

The second, exothermic oxidation step varies depending on the application. For TCES or solar air separation, the reduction step is followed by:

$$MO_{red} + \upsilon O_{2\,(g)} \rightarrow MO_{ox} + \Delta H_{ox} \qquad (1.2)$$

where the reaction closes the cycle, releases stored solar energy, and produces an O_2-deficient airstream. This step may be coupled with a power cycle for electricity generation

or used to produce pure streams of O_2 and N_2 from air. For solar fuels production, the oxidation is instead performed via one of:

$$
\begin{aligned}
MO_{red} + \upsilon H_2O_{(g)} &\rightarrow MO_{ox} + \upsilon H_{2\,(g)} \\
MO_{red} + \upsilon CO_{2\,(g)} &\rightarrow MO_{ox} + \upsilon CO_{(g)}
\end{aligned}
\tag{1.3}
$$
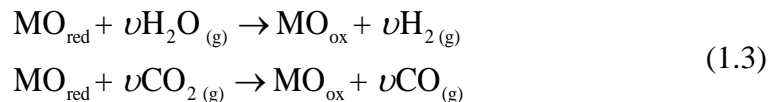
for an overall two-step reaction equivalent to $H_2O_{(g)} \rightarrow H_{2(g)} + 0.5O_{2(g)}$ for water-splitting or $CO_{2(g)} \rightarrow CO_{(g)} + 0.5O_{2(g)}$ for carbon dioxide splitting, without the extremely high temperatures required for the single-step thermal dissociations.
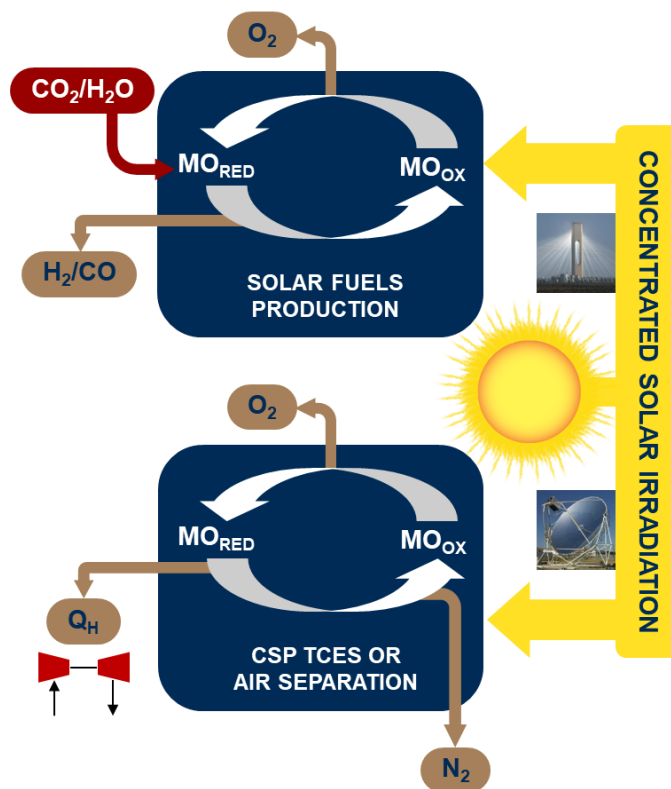
Figure 1.1 Schematic of two-step solar thermochemical cycles via redox-active metal oxides for solar fuels production (top) and CSP thermochemical energy storage and electricity production and/or air separation (bottom).

Because proposed two-step TCES, solar air separation, and solar fuels schemes employ similar reaction types and families of materials, there is some commonality in how

material candidates are evaluated. These criteria include temperatures at which the reduction and oxidation steps become thermodynamically favorable, energy storage density in the form of the redox enthalpy, chemical reaction rates, reaction cyclability, resistance to attrition, compatibility with containment materials, and cost/rarity.

However, differing solar thermochemical applications lead to variation in the relative importance of each of these metrics. For example, for TCES, reduction enthalpy is a particularly important parameter, as it influences the attainable capacity factor, power block size, and hours of storage for a concentrating solar power (CSP) plant. For solar air separation, the reduction enthalpy is similarly important, but is ideally minimized rather than maximized. For solar fuels production, the reduction enthalpy plays a still-important but less obvious role [8]. Furthermore, differences between the thermodynamics of the first and second reactions make certain redox materials well-suited to one application but not necessarily the other.

Many binary metal oxide pairs are appealing for thermodynamic processes, and some undergo thermal reduction and oxidation at reasonably quick rates. However, many binary metal oxides exhibit prohibitively slow kinetics at anticipated operating conditions [9] due to significant and unavoidable crystalline structural changes during reduction and oxidation. These limitations create a need to identify new redox-active materials with faster reaction kinetics. Mixed ionic and electronic conducting (MIEC) redox-active materials have been recently examined as a viable alternative to binary metal oxides due to their rapid kinetics and continuous reducibility [10]. MIEC materials have been shown to maintain their crystalline structure for large deviations from stoichiometry δ, increasing

4

reduction extents and thus energy storage density. The rapid kinetics of MIECs are related to the conduction of both electrons and oxygen ions through the sublattice.

MIECs with a perovskite structure have the ideal chemical form ABO_3, depicted structurally in Figure 1.2, where A and B are metal cation sites in the ideal cubic perovskite. Via selection of A- and B-site metals, as well as partial substitution or doping of the lattice with other metal species, a wide solution space is established for the design of perovskite materials. This creates potential for oxides with thermodynamic and kinetic properties that are finely tuned to their solar thermochemical applications.
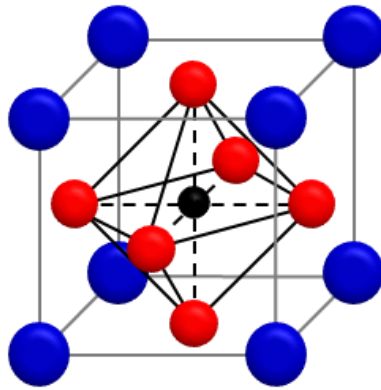
Figure 1.2 Unit cell of the ideal cubic perovskite crystalline structure ABO_3, including A-site cations (blue), a B-site cation (black), and oxygen anions (red).

The reduction of a perovskite oxide, assuming an initially-stoichiometric form, is:

$$ABO_3 + \Delta H_{red} \rightarrow ABO_{3-\delta} + \frac{\delta}{2} O_{2\,(g)} \tag{1.4}$$
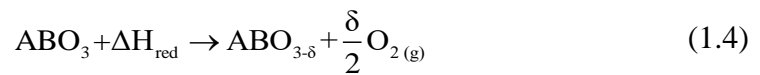
where B-site cations are typically reduced to satisfy electroneutrality for the oxygen vacancies produced by O_2 formation, while the A-site cations remain electrically unchanged, but influence the potential B-site oxidation states and the transport of oxygen ions through the sublattice.

5

For these rapidly-reacting materials, slow heating rates and gas changeovers make it impossible to observe kinetic limitations and therefore extract meaningful kinetic models via the same experimental methods used for binary metal oxides, which are typically limited in temperature range and/or heating rate. This drives the need to design and fabricate infrastructure that combines high temperatures, rapid heating rates, and high-frequency temporal measurements to examine reaction behaviors. Ideally, such infrastructure should also closely resemble the heat transfer modes and rates expected in the intended concentrating solar processes.

1.2   Objectives

The purpose of this study is to identify and evaluate new and state-of-the-art redox active metal oxide materials for solar thermochemistry. Many binary metal oxides are commercially available and have well-characterized thermodynamic properties which may be input to computational cycle analyses. The reaction kinetics may not be known under all thermodynamic conditions, redox material forms, and reactor configurations, but they can be investigated using traditional thermogravimetric analysis (TGA) methods.

Many perovskite oxides, however, are not commercially available or thermodynamically well-understood, particularly in specific doped compositions. Therefore, perovskites must often be synthesized and characterized via equilibrium TGA experiments and reaction models to extract thermodynamic properties. For kinetic analyses, the expected rapid reaction rates mean that novel infrastructure and experimental methods compatible with high heating rates must first be developed.

The thesis objectives are:

1. Characterize a high flux solar simulator (HFSS) for rapidly heating redox material samples to temperatures near or above 1273 K at heating rates greater than 50 K/s. Predict incident solar fluxes using experimental and/or computational methods.

2. Design, characterize, and validate a directly-irradiated reactor for heating redox samples with the HFSS, in order to temporally study reaction behavior. Develop computational models to predict spatial, temporal sample temperatures and reaction extents in the reactor.

3. Synthesize samples of perovskite-type oxides of various chemical compositions and dopant concentrations. Then, via equilibrium experiments, develop models to predict redox reactions and thermodynamic properties as functions of composition, temperature, and gas environment.

4. Using newly and previously determined thermodynamic properties, evaluate metal oxide materials for use in solar thermochemical applications, defining the thermodynamically ideal performance through relevant metrics such as solar input, work output, product yield, and cycle efficiency.

5. Using, where applicable, TGA and/or the HFSS-paired reactor, study the reaction rates of metal oxide materials and, if necessary, develop kinetic models to predict reaction rates as a function of composition, temperature, and gas environment.

1.3   Thesis Overview

The thesis is organized into three major parts. Chapter 2 is a literature review of previous studies on binary metal and perovskite redox-active oxides and the measurement of their properties. As these materials are relevant to the work detailed in later chapters, they are presented in the context of the solar thermochemical applications for which they are selected in those sections. The next three chapters detail the characterization and validation of the experimental infrastructure and methods used to analyze high-temperature redox reactions. The next two chapters detail the use of the novel and established analysis methods to characterize redox-active materials, and the use of thermodynamic and kinetic modeling to identify the materials for solar applications and bound their ideal theoretical performance. The final chapter summarizes the accomplishments of the thesis research and suggests future areas of investigation.

In Chapter 3, a characterization methodology is presented and applied to a high-flux solar simulator. Spatial radiative heat flux distributions are determined using calorimetric measurements coupled with digital images of reflections from a Lambertian target mounted in the focal plane. Imaging error corrections are applied, and pixel scale flux maps are produced in order to calibrate an existing Monte Carlo ray tracing radiative model of the HFSS.

In Chapter 4, a novel method is presented for mapping the HFSS Monte Carlo ray tracing model to computational heat transfer and fluid dynamics reactor models. The method is well suited to models with highly directionally and spatially-detailed concentrated radiative inputs, as observed in solar receivers and reactors. The algorithm is

compatible with unstructured, two and three-dimensional meshes with varying face and cell element shapes, respectively. Four case studies are performed on a directly irradiated, windowed solar thermochemical reactor. The method is shown to be energy conservative and to preserve spatial variation.

In Chapter 5, the design and characterization of an upward flow reactor (UFR) is presented. The UFR is designed to allow rapid heating of solid samples with concentrated irradiation from the HFSS to temperatures near and greater than 1273 K at heating rates above 50 K/s. As reactions are measured downstream of the samples via O_2 molar flow rates, gas phase lag and dispersion are characterized through a suite of O_2 tracer experiments. A transient computational fluid dynamics and heat transfer model of the UFR is combined with the Monte Carlo ray tracing model to predict spatial and temporal sample temperatures. The model is compared to a Co_3O_4/CoO thermal reduction experiment and the experimental bed temperatures are shown to be bounded by the average top and bottom modeled bed temperatures for the duration of the experiment.

In Chapter 6, solar electricity production via an Air Brayton cycle is considered with integrated thermochemical energy storage via Fe_2O_3/Fe_3O_4 redox reactions. A thermodynamic analysis of the system is performed to predict maximum cycle efficiencies and optimal operating conditions. Fe_2O_3 thermal reduction kinetics are captured by an Avrami-Erofe'ev nucleation model, an Arrhenius-type temperature dependency, and a power-law dependence on O_2 partial pressure. Fe_3O_4 oxidation is shown to exhibit rapid reaction rates but also to cross multiple kinetic regimes. Solid characterization is carried out using scanning electron microscopy and room/high temperature x-ray powder diffractometry to verify sample compositions and structures.

In Chapter 7, thermochemical N_2 production via air separation is considered using aluminum-doped $SrFeO_{3-\delta}$. Perovskite samples are synthesized using a sol-gel method and crystalline structures are confirmed via x-ray powder diffractometry. The compound energy formalism is applied to thermogravimetric measurements to predict nonstoichiometry and to determine the partial enthalpies and entropies of reaction. Aluminum doping is shown to modestly increase oxygen affinity and reduce the overall range of nonstoichiometries attained. Ten cycling experiments on an $SrFeO_{3-\delta}$ sample are performed using the UFR and HFSS to test cyclability. A thermodynamic analysis of the system is performed to predict N_2 purities and cycle efficiencies.

In Chapter 8, the technical contributions of this work are summarized. In addition, future improvements to the experimental and modeling methods described in the preceding chapters are suggested, and future research opportunities that have been enabled by this work are identified.

CHAPTER 2. LITERATURE REVIEW

2.1   Introduction

The transition from fossil fuels to renewable energies has motivated research aimed at harnessing the power of the sun. Many solar-driven technologies are available with the potential to meet growing energy demands while mitigating anthropogenic CO_2 emissions [11-13]. Of special interest is a subset of solar technologies that employ concentrated solar irradiation as a heat source to drive endothermic chemical reactions to produce solar fuels and/or solar electricity. These technologies provide a renewable route for storing intermittent sunlight in a chemical form for use when needed in two major applications: (1) Solar fuels (*e.g.* H_2 and CO) function as energy carriers [14-17] that can be stored and used on demand, or further processed to liquid hydrocarbons by known catalytic processes [18] to power the transportation sector; and (2) thermochemical energy storage (TCES) allows the production of electricity, as sunlight is stored in the bonds/potential of a chemical species via reversible, endothermic reactions which may then be accessed and coupled to a power cycle. TCES methods are particularly appealing choices for the high energy density needed to produce electricity in power cycles [19-21].

2.2   Solar Thermochemical Energy Storage

A variety of thermodynamically favorable reduction-oxidation (redox)-active binary metal oxides have been investigated using thermogravimetric analysis (TGA) [9, 22, 23] and lab-scale test reactors [24] to identify reaction behavior. Many metal oxide candidates have been proposed for TCES applications, including the Co_3O_4/CoO [21, 25-

11

27], Mn_2O_3/Mn_3O_4 [20, 28], CuO/Cu_2O [29-31], and BaO_2/BaO [32, 33] binary pairs, as well as a number of mixed ionic-electronic conducting metal oxides, which have the advantages of continuous redox equilibria, tunable thermodynamic properties, high reaction rates, and large redox capacities without departure from the perovskite phase [34-37].

Co_3O_4/CoO is one of the most thermodynamically and kinetically promising binary metal oxide pairs for TCES. In previous works, thermodynamic and kinetic analyses were used to examine electricity production in an Air Brayton cycle with integrated solar thermochemical energy storage (TCES) based on Co_3O_4/CoO redox reactions at a solar concentration ratio of 1000 suns (where 1 sun = 1 $kW \cdot m^{-2}$) [19, 23, 38]. The proposed cycle operates via the endothermic thermal reduction of Co_3O_4 to CoO in a windowed solar reactor to promote reduction favorability at lower temperatures. The CoO is then exothermically reoxidized to Co_3O_4 with compressed air to produce an O_2-deficient, high temperature, high pressure airflow. The airflow is expanded through a turbine to produce electricity.

TCES based on the Co_3O_4/CoO redox pair is especially promising due to rapid achievable reaction rates, a high reaction enthalpy, and cyclability of the redox reactions. However, cobalt oxides are relatively sparse and expensive [9] and pose potential human and environmental health concerns [39]. Co_3O_4 also thermally reduces at lower temperatures compared to some other redox pairs, reducing the maximum achievable cycle efficiency and producing a mismatch in pairing to solar concentrating infrastructure capable of high solar concentration ratios [40].

Fe_2O_3/Fe_3O_4 redox reactions are also particularly attractive for TCES, because Fe_2O_3 has a higher thermal reduction temperature than most other binary candidates, permitting higher theoretical Air Brayton cycle efficiencies. The Fe_2O_3/Fe_3O_4 redox pair materials are relatively inexpensive and widely available compared to Co_3O_4/CoO materials, and they carry fewer environmental/human health concerns [41], making the redox pair a more practical and economically appealing candidate for large-scale deployment.

Iron oxides have been the focus of numerous solar thermochemical studies, including carbothermal iron production [42], fuels co-production via carbothermal reduction and/or methane cracking [6, 43-45], and H_2O and/or CO_2 splitting via two-step cycles based on Fe_3O_4/FeO redox reactions [22, 46-49]. For the Fe_2O_3/Fe_3O_4 pair, the high Fe_2O_3 thermal reduction temperatures (>1700K) have presented both materials compatibility and engineering design challenges. Such concerns have prompted the study of combined oxides of iron and other multivalent metals, with the goal of lowering the thermal reduction temperature [21, 50-52]. However, past efforts have shown significant decreases in reaction enthalpy.

2.3   Solar Air Separation

Air separation is integral to many industrial processes, including the processing and combustion of fuels, the manufacturing of electronics, and the production of fertilizers. Cryogenic distillation [53] and pressure-swing absorption [54] are typical processes for air separation. However, a renewed focus on less energy-intensive, *in-situ* methods has prompted research in membrane technologies, where cost, scale, and purity vary widely

with the membrane material and design [55, 56]. Alternatively, two-step thermochemical cycles may be used for air separation by harnessing the oxygen-affinity of redox-active metal oxides. When the cycles are driven by concentrated solar irradiation, they reduce the CO_2 emissions associated with air separation.

Nitrogen fixation, or the separation of N_2 from air to form NH_3, may be accomplished artificially by the Haber-Bosch process [57]. There, a catalyst aids in the dissociation of N_2 and H_2, obtained from air separation and steam reforming of CH_4, respectively. The adsorbed gases react exothermically to produce NH_3 gas, which is separated from the reactants via condensation. The reaction is performed at elevated temperatures above 673 K to overcome kinetic limitations and pressures above 200 bar to maintain thermodynamic favorability. Production is energy intensive, with an associated global warming potential of 2.6 kg CO_2-equivalent per kg NH_3 [58]. Novel solar-driven N_2 separation and NH_3 fixation methods therefore have the potential to significantly mitigate greenhouse gas emissions.

High-purity inert gases are also important for moving solar thermochemical cycles closer to commercial realization. Inert sweep gases (*e.g.*, N_2 and Ar) are employed in two-step solar thermochemical redox cycles [59] for producing solar electricity and splitting H_2O/CO_2, as they allow favorable thermal reduction at lower temperatures via Le Chatelier's principle [1, 19, 60]. Separation of the sweep gas from the O_2 evolved during the thermal reduction is essential to make the cycle viable. Thermochemical separation by applying a second two-step cycle to the flow mixture was proposed in previous work [61].

14

Ideal thermochemical air separation candidates typically have low enthalpies of reduction, allowing lower temperature processes than other solar thermochemical cycles. Binary metal oxides have been studied for such a purpose [7, 62], with CuO/Cu_2O and AgO/Ag_2O emerging as particularly promising candidates. More recently, mixed ionic-electronic conducting (MIEC) perovskite oxides (ABO_3) have been investigated due to their continuous reduction with temperature and potential for rapid oxygen exchange [63-65]. Rapid kinetics result from the high conductivity of electrons and oxygen ions through the sublattice [66]. By substituting or doping the oxides on their A and/or B sites, the A/B solution space is widened considerably, and the potential for thermodynamic properties finely-tuned for an air separation process is unlocked.

The perovskite $SrFeO_{3-\delta}$ was the subject of previous studies for chemical looping [67, 68] and solid oxide fuel cell [69] applications. A screening study for air separation [64] identified $SrFeO_{3-\delta}$ for its considerable reducibility via high deviations from stoichiometry at relatively low temperatures. Mn- [70] and Cu- [71] doped $SrFeO_{3-\delta}$ were examined further for the dopant influence on oxygen affinity and reduction temperature. Both Fe and the dopant cations underwent reduction and oxidation, with increased Mn and Cu compositions favoring higher-temperature reduction. Al and Ti have been used as dopants for $CaMnO_{3-\delta}$ due to high average bond strengths and were found to increase the thermal reduction temperatures and enthalpies in solar thermochemical energy storage applications [36].

To predict the thermodynamic performance of a perovskite-oxide thermochemical cycle, there must first exist reliable predictions for redox behavior with varying temperatures and pressures. Doped and undoped $SrFeO_{3-\delta}$ thermodynamic studies have

15

done so by employing different lattice defect models [72] due to the ranges of temperature and O_2 pressure studied. These models used combinations of random oxygen vacancies, disproportionation [73], and/or non-interacting and interacting clusters based on statistical thermodynamics [74-77], with mixed results. Difficulties developing comprehensive thermodynamic models for $SrFeO_{3-\delta}$ are due to the ease of reducibility, as the wide deviations from stoichiometry result in complex defect behavior and lattice interactions across the full range of temperatures and pressures.

The compound energy formalism (CEF) [78] is a thermodynamic modeling method that has been employed for complicated MIEC materials. It can capture the influences of individual lattice constituents without relying on the assumption of specific lattice reactions. The CEF was previously used to model the thermodynamics of $LaMnO_{3-\delta}$ [79] and $(La,Sr)MnO_{3-\delta}$ [80] using data compiled from literature and was compared to fits with the more restrictive lattice defect models. The CEF was also used in the comprehensive thermodynamic description of cerium-oxygen systems [81], including the nonstoichiometric $CeO_{2-\delta}$ fluorite phase, which was later extended to compositions containing yttrium [82]. Due to its versatility and implicit accounting for non-ideal solution behavior, the CEF is well-suited to modeling $SrFeO_{3-\delta}$ and other oxygen-deficient perovskite oxides.

For many perovskite oxide materials, slow heating rates and gas changeovers in traditional TGA make it impossible to extract meaningful kinetics. This drives the need to design and fabricate infrastructure that combines rapid heating rates and high frequency measurements to examine temporal reaction behaviors and rates.

2.4   Reactors for Reduction-Oxidation Characterization

Previous research into pairing rapid heating with temporal redox measurements includes solar-driven TGA, used to determine reaction kinetics for the isothermal dissociation of ZnO [83] and the reduction of non-volatiles Mn_2O_3 and Mn_3O_4 [28], and to study CO_2 splitting cycle reaction rates of doped and undoped porous CeO_2 structures [84]. Non-TGA, downstream-measurement methods have also been used, including a stagnation-flow reactor (SFR) with a SiC furnace and product gas measurement via mass spectrometry. The SFR was used to extract oxidation kinetics for a cobalt ferrite-zirconia composite for H_2 production [85], and it was determined that characterization of reactor transport, namely product gas lag and dispersion, was critical for accurate kinetic modeling. Another, directly-irradiated cavity-type solar reactor also employed a downstream-measurement method, but the horizontal packed bed sample and flow configuration resulted in minimal dispersion for a range of flow rates [86].

Temperature and reaction measurement within on-sun reactors is often difficult. Temperature measurement devices such as IR sensors may be confounded by reflections from the radiative source, and thermocouples measure only a local region around the location of a metal probe. Computational models therefore may need to be developed to predict spatial and temporal temperatures [5] and reaction extents. This is a process which encompasses four non-trivial steps, described in the following sections:

measure radiation source → model radiation source →
input radiation source to reactor model → model reactor

2.4.1   High Flux Solar Simulator for Rapid Sample Heating

High-flux solar simulators (HFSS) are important tools for driving solar thermochemistry research, as they provide controlled laboratory environments for the experimentation needed to develop prototype solar thermochemical reactor/solar receiver technologies. With a HFSS, the technologies can be developed, optimized at small scales, then scaled up after optimal operating parameters are identified. A HFSS is an ideal device for providing the rapid heating rates to study MIECs, as it not only provides a highly concentrated input of thousands of suns within a matter of seconds, but a HFSS built with Xe arc lamps closely approximates the spectral distribution of sunlight.

A HFSS inherently produces highly directional, spatially-varying input radiation. Monte Carlo ray tracing (MCRT) [87] is a stochastic method that is ideal for capturing solar inputs, but MCRT models require calibration via estimation of the total energy production of the light source. Precise determination of spatial heat distributions, generally referred to as flux mapping, may be used to calibrate MCRT models. Flux mapping allows for the pixel-precise measurement of radiative heat fluxes to solar thermochemical reactor/receivers. Flux maps are generated by aligning a Lambertian reflector in the focal plane, then obtaining images of reflected radiation from the concentrator system. The pixel intensities are calibrated to a measurement standard (e.g., heat flux gauges or calorimeters) based on a linear response [88], resulting in global calibrations.

Simple flux mapping alone is not sufficient for predicting radiation from a HFSS, as it only provides information about the irradiation in a specified plane and not generalized directional and spatial radiative intensities. While work has shown that multiple flux maps

at various locations can yield experimental directional irradiation intensities [89], such a method is experimentally cumbersome. MCRT is therefore appealing to extend the characterization beyond one plane, to the multiple surfaces of solar receivers/reactors.

The use of charge-coupled device (CCD) cameras to produce high-resolution flux maps is well established: A variety of methods are reported for calibrating CCD pixel intensities to radiative heat flux measurements in the focal plane. One or more radiometers [90] are often placed at the focal plane and flux measurements are globally or locally correlated to the pixel intensities at radiometer position(s) from CCD images. Calibrations are performed to account for instrument errors [91-93] and, when necessary, spectral dependencies [94]. To prevent saturation of the camera sensor, short exposure times and neutral-density (ND) filters are employed. To obtain pixel intensities for the radiometer locations in the CCD images, several techniques have been used, including mechanical methods (e.g., closing-shutter [95] and rotating wand [96] gauges) and image processing techniques such as nearest-neighbor pixel estimation [97].

In lieu of radiometers, calorimetry is employed for calibration, including flat plate calorimeters that mitigate convective and re-radiative losses to the surroundings by keeping the receiving plate at near ambient temperature [98, 99]. Cavity-type calorimeters are ideal for maximizing radiative absorptivity by creating a near blackbody environment and minimizing spectral dependencies [100-103]. Other non-radiometer techniques include correlating a globally averaged target flux to theoretical calculations of the power provided by the concentrator system [104] and a novel calibration method [105] whereby a correlation of CCD images of the sun and on-site direct-normal irradiation measured with a pyrheliometer is applied to receiver flux maps.

19

While flux mapping is used extensively for concentrating solar technology characterization, existing literature either does not explicitly outline methodologies for the mapping and calibration or omits mention of one or more sources of map error. Camera-specific errors (e.g., lens distortion) are generally neglected in the calibration process, and images are often produced from cameras mounted normal or near-normal to Lambertian targets, negating the need for correction of perspective errors. However, in many systems (e.g., HFSSs) such a camera position is either impractical or impossible, and the perspective correction procedure is noted but not rigorously defined. To accurately construct computational models of HFSS radiation using experimental flux maps, such errors must be corrected.

2.4.2   Coupling the Solar Input to Computational Models

To use a HFSS-paired reactor to study redox behavior, computational heat and fluid dynamics (CFD) models typically must be developed to understand sample temperature changes and reaction rates, which may exhibit significant spatial and temporal variations. Just as the highly directional nature of concentrated light from a HFSS must be captured through careful experimental measurements, error corrections, and modeling, robust methods must be used for coupling the modeled radiative input to the CFD models for studying redox behavior. Various methods exist for coupling or mapping external radiation models to computational heat and mass transfer models of solar receivers/reactors, but they typically involve tradeoffs in computational accuracy.

Other than MCRT, finite volume approximations to the radiative transport equation (FV–RTE) are the primary method for modeling radiative heat transfer to or within

20

receiver/reactor models. Challenges in implementing MCRT for solar receivers/reactors occur when modeling optically thick media, wavelength/temperature-dependent radiative properties, and complex geometries. These conditions may prove more tractable using FV–RTE methods such as the discrete ordinates method, which is supported in computational software [106]. FV-RTE methods are computationally expensive for domains requiring high mesh resolutions, like combined models of solar receivers/reactors and collecting/generating infrastructure. Fortunately, MCRT and FV-RTE methods have complementary strengths. MCRT may be used to model the directional concentrated solar input to the receiver/reactor, such as from a HFSS, and FV-RTE may be used to capture internal radiative exchange within the reactor. If paired appropriately, the models are a powerful tool for modeling radiative heat transfer to and within solar receivers/reactors.

Prior methods for pairing MCRT and FV-RTE have been implemented by employing 1) non-overlapping or 2) overlapping domains. In non-overlapping schemes [107-109], models of the solar input are mapped to the CFD model at a common boundary through an often-intensive process of translating directional solar inputs to intensity boundary conditions. Non-overlapping schemes may be functionally energy-conservative. However, to mitigate discretization error, they require fine meshes that are directionally aligned with the solar input, which may extend computational time and inhibit CFD convergence. Restricting non-overlapping schemes to two-dimensional domains has been recommended [108].

In overlapping schemes [38, 110-113] some portions of the MCRT and CFD modeling domains are spatially coincident. In this scheme, the external radiative input is modeled from the collector/generator until it is 1) absorbed by internal receiver/reactor

21

surfaces or media, modeled as boundary or volumetric sources, respectively; or 2) rejected from the receiver/reactor by reflection, transmission, or scattering. Re-emission within the receiver/reactor is captured separately in the CFD model. For diffuse surfaces, overlapping schemes permit coarser CFD meshes that are not necessarily directionally aligned with the solar input. Systematic errors may result from the representation of curved geometries in the MCRT domain as planar approximations in the CFD domain [113] but can be mitigated by careful meshing and mapping.

Absorbed rays in overlapping schemes may be implemented as surface [114] or sub-surface [86, 115] averaged fluxes. This approximation maintains energy conservation but not preservation of spatial variation between the MCRT and CFD models. Alternatively, absorbed rays may be binned into a grid within the MCRT modeling domain to produce a spatial irradiation profile, which may then be interpolated to the CFD mesh [110]. For sufficiently fine grids and meshes, this method preserves spatial variation but does not guarantee energy conservation.

CHAPTER 3. HFSS CHARACTERIZATION

3.1   Introduction

A detailed methodology is presented for calibrating a high flux solar simulator used to drive solar thermochemical reactions of redox-active materials. The HFSS consists of seven 6 kW$_e$ xenon short-arc lamps (Osram XBO 6000 W/HSLA) mounted in truncated ellipsoidal reflectors as shown in Figure 3.1. The HFSS is based on a previous design [116], and the reflectors share a common focal point at which various solar technologies (e.g., solar thermochemical reactors) are mounted. Calorimetry was used to accurately calibrate reflected intensities from the HFSS attenuated by a ND filter (CVI Melles Griot NDQ-400-2.00) and measured by a CCD camera (Basler Scout scA 1400-17gm). Corrections were developed for three error types: (1) lens distortion, (2) off-centering brightness loss, and (3) perspective shape distortion [117]. Since previous works do not discuss a comprehensive correction method for these error sources, an explicit methodology for pixel-scale error corrections was developed. The routines used for shape distortion correction were verified using projective geometry techniques [118, 119]. For off-centering brightness loss, correction equations were derived. The results were also used to calibrate a Monte Carlo (MC) ray tracing program, which was built based on the VeGaS software [120], to determine directional intensities for use as inputs for heat and mass transfer models of solar thermochemical reactors.
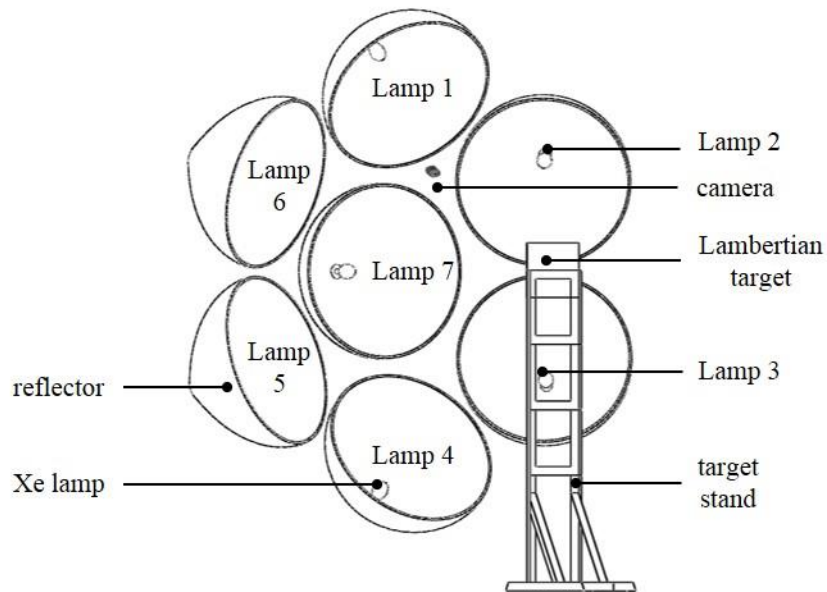
Figure 3.1 A detailed schematic of the high-flux solar simulator consisting of seven 6 kW$_e$ xenon short-arc lamps mounted in truncated ellipsoidal reflectors. The reflectors are arranged to ensure a common focal point for all seven lamps, enabling reproducible radiative heat fluxes similar to solar power towers and dishes.

3.2   Experimental

Experimentation was performed using a cavity-type calorimeter depicted schematically in Figure 3.2[1]. The calorimeter was mounted in the focal plane of the HFSS, and radiative heat fluxes were measured over a range of conditions. The calorimeter consisted of a water-cooled stainless-steel diaphragm through which concentrated irradiation was introduced to the cavity via a 40 mm diameter aperture (*i.e.* the hole cut in the diaphragm). Any spillage of irradiation (*i.e.* irradiation on the front of the diaphragm)

---

[1] The design and Monte Carlo ray tracing of the calorimeter were developed by Robert Gill, with whom calorimetry experiments and calculations were performed in collaboration. Full details are given in:

121. Gill, R., et al., *Characterization of a 6 kW high-flux solar simulator with an array of xenon arc lamps capable of concentrations of nearly 5000 suns.* Review of Scientific Instruments, 2015. **86**(12): p. 8.

was assumed to be removed by cooling coils in the diaphragm. The inside of the diaphragm was polished to produce a highly reflective, specular surface to minimize absorption of reflected radiation from the cavity. The irradiation directly impinged upon the body of the calorimeter, constructed of 9.525 mm diameter soft copper tubing and coated with a black paint (VHT Flameproof Coating SP102) to maximize the absorptivity, measured as 0.984 ± 0.00065 after annealing. The soft copper tubing was encased in a 101.6 mm diameter copper tube that reduced to 50.8 mm and was capped. The encasement was supported inside a 152.4 mm diameter steel pipe by a Duraboard frame, and the void was filled with mineral wool insulation. The water flow rate inside the cavity reached ~3.2 L_N/min (where L_N is the nominal flow at 20 °C and 1 atm) as measured by a liquid flowmeter (Omega FPR301 Low Flow Liquid Flowmeter). The inlet and outlet water temperatures were measured by t-type thermocouples, and an additional t-type thermocouple was fixed to the outer side of the steel encasement to measure surface temperature during experimentation.
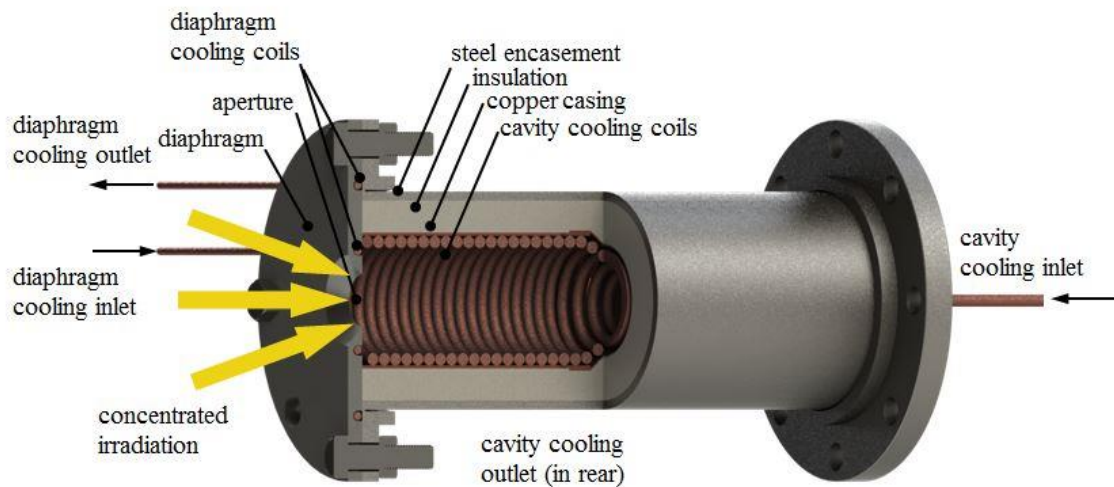
Figure 3.2 A schematic of the calorimeter used in the experiment with concentrated irradiation entering through the aperture. Water enters the cavity coils through the rear and exits behind the water-cooled diaphragm (not pictured). The coils are encased in a copper shell which is packed into a steel frame with insulation.

The incident radiative heat fluxes from the HFSS were determined by considering all relevant heat flows in and out of the calorimeter using measured properties, literature values, and modeling. The heat leaving the calorimeter from the water flow assuming steady state, incompressible flow with constant properties, and negligible kinetic and potential energies was calculated as:

$$\dot{Q}_{H_2O} = \rho_{H_2O} \dot{V} c \Delta T_{coil} \tag{3.1}$$

where ρ_{H_2O} is the density of H_2O determined at 1 atm and the inlet temperature; $\dot{V}$ is the volumetric flowrate; c is the heat capacity of water at 20 °C; and ΔT_{coil} is the temperature rise of water across the cavity cooling coils. Water properties are assumed to be at the inlet temperature of ~20°C and constant due to the low ΔT_{coil} ~4 K, as measured during experimentation. Re-radiative losses through the aperture were estimated assuming blackbody behavior in the environment (*i.e.* the area of the surrounding was much greater than aperture area), represented as:

$$\dot{Q}_{rerad} = \varepsilon_{cavity} \sigma A_{aperture} \left(\bar{T}_{cavity}^4 - T_{surr}^4 \right) \tag{3.2}$$

where ε_{cavity} is the apparent cavity emissivity assuming an effective gray, diffuse surface; σ is the Stefan-Boltzmann constant; $A_{aperture}$ is the area of the aperture; $\bar{T}_{cavity}$ is the average surface temperature of the cavity; and T_{surr} is the measured temperature of the surroundings. The heat losses to the environment conducted from the cavity and through the insulation and convected to the surroundings were determined as:

$$\dot{Q}_{conv} = A_{surface} \bar{h} \left(T_{surface} - T_{surr} \right) \tag{3.3}$$

where $A_{surface}$ is the surface area of the steel encasement and back; $\bar{h}$ is the average convective heat transfer coefficient for natural convection between a non-infinite cylinder and ambient surroundings [122]; and $T_{surface}$ is the measured surface temperature of the steel encasement at steady state. $T_{surface}$ was assumed to be constant over the outer surface since convective losses accounted for less than 1% of the total heat absorbed by the calorimeter from the HFSS. The radiative exchange between the surroundings and steel encasement was neglected due to a small temperature difference between the T_{surr} and $T_{surface}$. The radiative input from the HFSS at the aperture was calculated once steady-state conditions were reached as:

$$\dot{Q}_{HFSS} = \int G_{HFSS} dA_{aperture} = \frac{\dot{Q}_{H_2O} + \dot{Q}_{rerad} + \dot{Q}_{conv}}{\alpha_{cavity} - F_{diaphram}} \tag{3.4}$$

where G_{HFSS} is the irradiation on the target from the HFSS; $\alpha_{cavity} = \varepsilon_{cavity}$ is the apparent absorptivity of the cavity assuming a gray, diffuse surface; and $F_{diaphram}$ is the fraction of total incoming energy passing through the aperture but absorbed by the inner side of the diaphragm, as calculated from MC ray tracing. $F_{diaphragm}$ was included to show cooling for the diaphragm via a separate water-cooling stream in the analysis.

Flux maps were produced from digital CCD camera images calibrated by calorimetric measurements. A Lambertian target was placed in the focal plane of the HFSS at the same location as the calorimeter in the previous test and subjected to identical conditions. The camera was mounted behind the HFSS off-normal relative to the Lambertian target due to the position of Lamp 7 (Figure 3.1), and two ND filters were

27

placed in front of the camera aperture to prevent overexposure. The camera focal length was manually adjusted and remained unchanged throughout experimentation.

Lens distortion errors were corrected by acquiring a series of images of a planar checkerboard surface with known dimensions at varying angles and positions relative to the camera. Checkerboard corners were located within each image and used to resolve the camera position relative to the board in each image. A distortion model for the lens was then created, and this model was applied to all images both during calibration and flux map production prior to perspective corrections.

Digital images were then acquired, and flux maps were determined based on camera position. The relative positions of the lamps, target, and camera referenced in the correction derivations, as well as the incident powers and fluxes on the target and camera, are schematically depicted in Figure 3.3. Irradiation from the HFSS onto the Lambertian target was diffusely reflected, and a portion of the reflection was contained in the solid angle of the CCD sensor. The resulting image was used to generate radiative heat flux maps by correlating calorimetric measurements to the pixel intensities over the area that corresponded to the location of the calorimeter aperture.
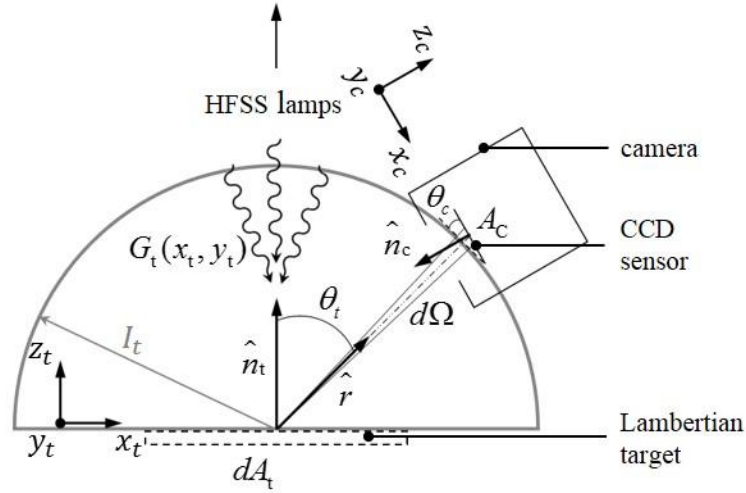
Figure 3.3 A schematic of the Lambertian target and CCD camera/sensor positions. Incoming irradiation from the high-flux solar simulator onto a differential surface area and reflected through the solid angle onto the CCD sensor is depicted. Relative Cartesian coordinates and solid angles for the Lambertian target and CCD camera are also depicted.

The camera sensitivity limited acquisition to the visible spectrum; therefore, all detected irradiation was assumed to originate from the HFSS. For a differential sensor area, the electric potential was proportional to the reflected intensity from the Lambertian target, given as:

$$\xi_{CCD} = \zeta F_{visible} V_{ND} t_{exp} I_t(x_t, y_t) d\Omega \tag{3.5}$$

where ζ is a proportionality constant; $F_{visible}$ is the fractional function in the visible spectrum; V_{ND} is the slab transmittance of the filter; t_{exp} is the CCD camera exposure time; I_t is the intensity of radiation from a point (x_t, y_t) on the target; and $d\Omega$ is the differential solid angle. Assuming diffuse reflections, the irradiation and differential solid angle were related to the local radiative heat flux from the HFSS, respectively, as:

$$I_t = \frac{J_t(x_t, y_t)}{\pi} = \frac{\rho_t G_{HFSS}(x_t, y_t)}{\pi} \tag{3.6}$$

29

$$d\Omega = \frac{dA_s}{r^2} \cong \frac{A_C \cos \theta_C}{r^2}$$

(3.7)

where J_t is the target radiosity assuming negligible target emissions and ambient reflections; ρ_t is the target reflectivity; dA_s is the differential surface area characteristic to the solid angle; A_c is the area of the CCD sensor; θ_c is the angle of incidence of light on the sensor area; and r is the straight-line distance from (x_t,y_t) to (x_c,y_c). Angles and straight-line distances varied with position on the target and the CCD sensor was small (*i.e.* a point-receiver). A model was implemented to transform pixel locations to world coordinates in order to relate the projected area to the actual target area, represented as:

$$dA_t = \frac{dA_p}{\cos \theta_t} = \frac{dA_p}{\hat{n}_t \cdot \hat{r}(x_t, y_t)}$$

(3.8)

where dA_p is the projected differential target area normal to the camera; θ_t is the angle between $\hat{n}_t$ the target surface unit normal and $\hat{n}(x_t,y_t)$. The spatially changing r and θ_c from each target location to the CCD chip and all pixel coordinates (x_p,y_p) were mapped to real world points (x_t,y_t) with a projective transformation, represented as:

$$\begin{bmatrix} x_{t,1} & x_{t,2} & & x_{t,n} \\ y_{t,1} & y_{t,2} & \cdots & y_{t,n} \\ 1 & 1 & & 1 \end{bmatrix} = \overline{\overline{\mathbf{M}}}_{p\to t} \begin{bmatrix} x_{p,1} & x_{p,2} & & x_{p,n} \\ y_{p,1} & y_{p,2} & \cdots & y_{p,n} \\ 1 & 1 & & 1 \end{bmatrix}$$

(3.9)

where n is the pixel index and $\overline{\overline{\mathbf{M}}}_{p\to t}$ is the projective transformation matrix created by relating the four known locations of the target corners to corresponding pixel positions in CCD images, knowing each set of corners was coplanar within its respective coordinate system. This transformation and lens distortion correction are shown in Figure 3.4 with the

30

Lambertian target. Figure 3.4a depicts the edges of the Lambertian target as they appear from the camera position, and Figure 3.4b depicts the edges after correction, adjusted to produce a normal view of the target. An initially-square boundary was added in post-processing to Figure 3.4a prior to correction to capture the image skewing. A dotted circle indicating the calorimeter aperture location was overlaid and similarly corrected to indicate the area of the target used for calibration with calorimetric measurements.
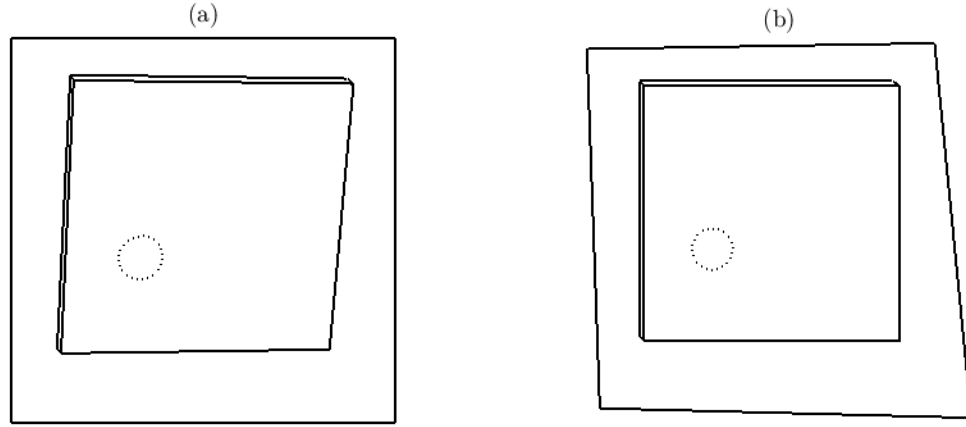
Figure 3.4 Results of perspective shape distortion correction to overlaid images of the Lambertian target edges (solid lines) and calorimeter aperture (dotted lines): (a) the images as viewed by the camera during image acquisition, (b) the corrected images.

The spatial irradiance measurements were coupled to calorimetric measurements by integrating over the boundaries of the aperture of the calorimeter, represented as:

$$
\dot{Q}_{\mathrm{HFSS}} = \int_{A_{\mathrm{aperture}}} G_{\mathrm{HFSS}}(x_{\mathrm{t}}, y_{\mathrm{t}}) dA_{\mathrm{aperture}}
$$

$$
\cong \sum_{A_{\mathrm{aperture}}} \frac{\pi r^2}{A_{\mathrm{C}} \cos\theta_{\mathrm{C}}} \frac{\xi_{\mathrm{CCD}}}{\zeta F_{\mathrm{visible}} V_{\mathrm{ND}} t_{\mathrm{exp}} \rho_{\mathrm{t}}} \Delta A_{\mathrm{aperture}}
$$

(3.10)

where the left-hand side is the result from calorimetry, and the right hand side are the results taken from digital image processing, using only the pixels that were found to fall within the aperture by overlaying it on flux images. The two sets of experimental data are related by the constant ζ. ρ_t, V_{ND}, t_{exp} $F_{visible}$, and A_C remained constant and were lumped together with ζ to define an experimentally determined calibration constant, given as:

$$\zeta^* = \frac{1}{A_C \zeta F_{visible} V_{ND} t_{exp} \rho_t}$$

(3.11)

Combining the above equations, the spatial HFSS irradiance was determined as:

$$G_{HFSS}(x_t, y_t) = \zeta^* \frac{\pi r^2}{\cos \theta_C} \xi_{CCD}$$

(3.12)

3.3   Modeling

The pixel-scale flux maps were employed in the calibration of a Monte Carlo ray tracing model of the high flux solar simulator developed by a colleague, Robert Gill. The results of this work are discussed in the next section. The full details of the calibration procedure and results from ray tracing are provided elsewhere [121].

3.4   Results and Discussion

A series of calorimetric experiments was performed with different lamp combinations. Temporal results using calorimetry with Lamp 7 are shown in Figure 3.5. The xenon arc lamp was ignited and the lamp input electric power P rapidly increased to 4.65 kW as the arc was established. ΔT_{coil} of the calorimeter cavity increased to ~3.75 K in ~300 seconds, directly corresponding to the time required for the calorimeter to reach steady-state due to a relatively large thermal mass. The shaded area in Figure 3.5 denotes near steady conditions for the calorimeter. As the experiment progressed, P began to degrade slightly due to the non-ohmic nature of the resistor shunts used to measure current to the lamps.
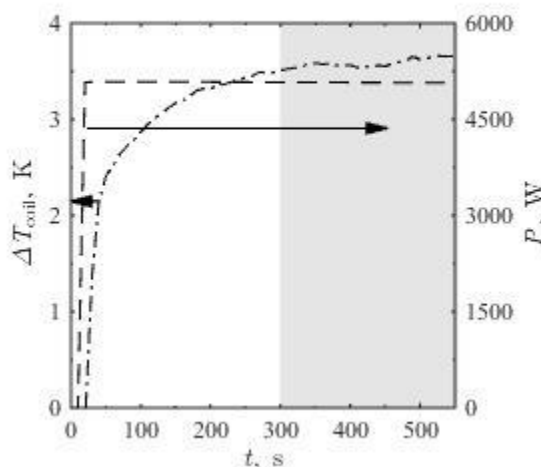
Figure 3.5 Temporal xenon arc lamp electric power (dashed) and change in water temperature across the calorimeter cavity cooling coils (dashed-dotted) for Lamp 7. The shaded box highlights of the time interval where steady state conditions were assumed for the calorimeter. Steady conditions for the HFSS, reflectors, and Lambertian target were at a much faster timescale (*i.e.* 30 s).

The results from calorimetry are shown in Table 3.1 for summing of two single lamp measurements together and comparing these results with measurements after reaching steady state, taken with two lamps running simultaneously. A maximum percent difference of 3.36% was found for Lamps 1 and 4. The experimental error was determined via an error propagation analysis. The summed single lamp and multi-lamp flux differences were within the 95% error bounds for all runs, providing confidence in the calorimetric measurements.

Table 3.1 Single and multi-lamp average flux comparison with 95% error bounds, where the single lamp flux measurement is the sum of two lamps running individually, and the multi-lamp flux is the measurement with both lamps simultaneously running.

Lamps	Single Lamp Sum q, kW·m^{-2}	Multi Lamp q, kW·m^{-2}	Difference, %
1 & 4	1451 ± 122	1403 ± 162	3.36
2 & 5	1739 ± 146	1760 ± 217	1.16
3 & 6	1020 ± 85	1047 ± 120	2.61

The overall flux map is shown in Figure 3.6 for the Lambertian target placed in the focal plane. The flux map was produced with superposition of individual lamp measurements and was highly symmetric. A $\bar{q}_{HFSS}= 4880 \pm 223$ kW·m^{-2} with 95% error was measured via calorimetry, and a total $\dot{Q}_{HFSS} = 6.13 \pm 0.27$ kW was determined for a 40 mm diameter aperture. An experimental peak $q = 6834$ kW·m^{-2} was calculated using the calibrated flux map, which corrected for an off-centering loss of 20 kW·m^{-2} at peak radiative heat fluxes.
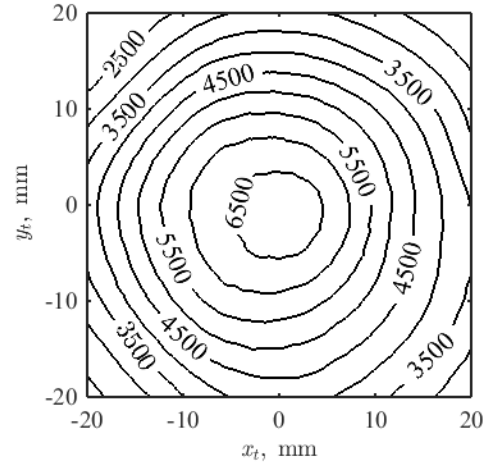
Figure 3.6 Measured spatial radiative heat fluxes in kW·m^{-2} in the focal plane of the high flux solar simulator by summing all seven xenon arc lamps.

The experimentally determined spatial q for Lamp 5 were used to calibrate parameters in the MC ray tracing using least-squares analysis and regressing modeled $q = f(\sigma_s, \varepsilon_w)$ with measured q with the Nelder-Mead algorithm [123]. The reflectivity of the truncated ellipsoidal reflector was assumed as 0.95 (polished aluminum) [101]. The experimental q for Lamp 5 calibrated with calorimetric measurements is shown in Figure 3.7a. The results are slightly skewed to the right, as the off-normal irradiation is projected onto the focal plane. The MC ray tracing results are shown in Figure 3.7b. The q contours are more equally spaced around the focal point than experimentally measured q (Figure 3.7a) primarily due to modeling assumptions (*e.g.*, uniformly emitting plasma cylinder), alignment errors, and shape distortions in the reflectors. Additionally, the q contours are further spaced in MC ray tracing results, indicating a more uniform flux field. The MC ray tracing resulted in $\bar{q} = 893.3 \pm 262.8$ kW·m^{-2} over the calorimeter aperture for Lamp 5, while the calorimeter measured $\bar{q} = 892.5 \pm 105.3$ kW·m^{-2}. A reflector specular error $\sigma_s = 5.92 \pm 0.05$ mrad and a power to radiation conversion efficiency $\kappa = 0.537 \pm 0.004$ were determined from least squares analysis for Lamp 5.

35
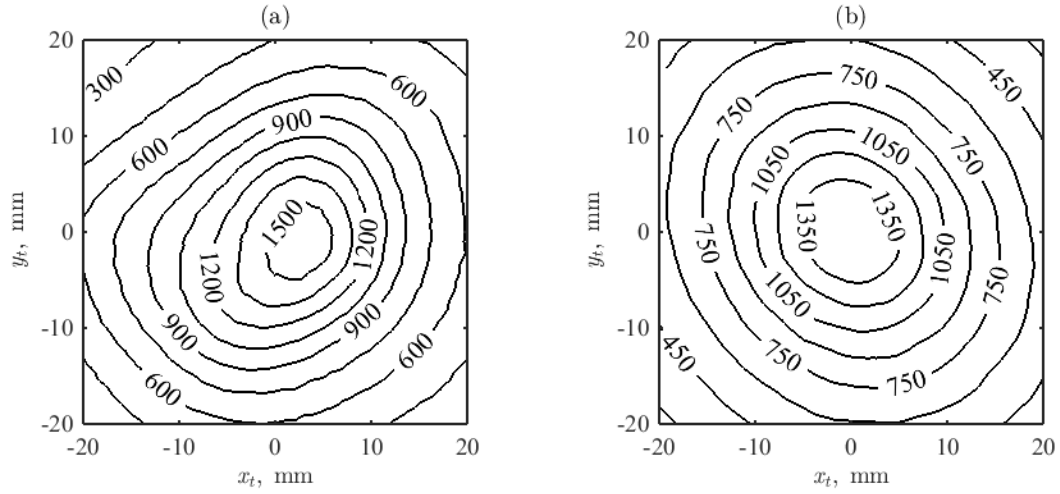
Figure 3.7 Measured spatial heat fluxes for Lamp 5 in kW·m^{-2} from the (a) high-flux solar simulator and the (b) Monte Carlo ray tracing model.

3.5   Conclusions

A robust methodology is outlined for characterizing the radiative heat inputs of a high-flux solar simulator with seven xenon short-arc lamps mounted in truncated ellipsoidal reflectors. A cavity-type calorimeter was used to accurately measure radiative heat fluxes in the focal plane of the simulator. The results were used to calibrate the pixel intensities of images acquired from a Lambertian target with a CCD camera. Lens distortion, off-centering brightness loss, and perspective shape distortion were also considered. The peak and average radiative heat fluxes over a 40 mm diameter were 6834 kW·m^{-2} and 4880 ± 223 kW·m^{-2}, respectively, when all lamps were running. The measured radiative heat fluxes were used to calibrate the radiative heat transfer in the high-flux solar simulator modeled using the Monte Carlo ray tracing developed by a colleague. Least squares analysis was used to regress modeled versus measured heat fluxes as a function of specular error and electric power to radiation conversion efficiency, producing a reflector

specular error of 5.92 ± 0.05 mrad and an electric power to radiation conversion efficiency of 0.537 ± 0.004.

The step-by-step methodology summarized in this paper provides a means for accurately quantifying irradiances from high flux solar thermochemical reactors/solar receivers in experimentation over a range of operating conditions. These experimental results were coupled with the radiative heat transfer model developed by a colleague to calibrate the results, allowing for precise determination of directional intensities, essential for constructing accurate heat and mass transfer models for solar thermochemical reactor/solar receiver technologies. These results provide the foundation for developing and optimizing the solar technologies needed to expedite the transition to renewable energy driven by concentrated sunlight.

CHAPTER 4. MONTE CARLO-CFD MAPPING

4.1   Introduction

An algorithmically simple method of Monte Carlo ray tracing (MCRT) to computational fluid dynamics (CFD) mapping is presented to accurately pair radiative solar inputs from the high flux solar simulator (HFSS) to the computational models of the upward flow reactor (UFR). The method was developed to capture the highly directional, spatial nature of the radiative input from the HFSS, as predicted by the MCRT model, while also maintaining energy conservation.

MCRT allows for the directional modeling of radiative heat transfer by partitioning reflections or emissions from a radiation source, in this case concentrating solar collectors (*e.g.* heliostats, parabolic troughs/dishes) or generating devices (*e.g.* high flux solar simulators; HFSS), into rays or individual packets of energy, represented as:

$$\dot{E}_k = \frac{\dot{Q}_{sun}}{N_{rays}} \tag{4.1}$$

where $\dot{Q}_{sun}$ is the total radiative power, here assumed to be evenly partitioned among N rays. N_{rays} is typically between 10^5 and 10^7, and MCRT convergence is expected for $N_{rays} \rightarrow \infty$. The path of a given ray $k = 1, 2, \ldots, N_{rays}$ is defined via [87]:

$$\vec{r}_k = \vec{r}_{0,k} + D\hat{s}_k \tag{4.2}$$

where $\vec{r}_k$ is the ray intersection located a distance D and direction $\hat{s}_k$ from the ray origin $\vec{r}_{0,k}$. The origin may be the point of ray generation (*i.e.* introduction to the model) or the point of the previous ray interaction (*e.g.* reflection, scattering) in the system.

The MCRT–CFD mapping method introduces no spatial or energy conservation errors beyond the MCRT precision and CFD mesh resolution. The method may be implemented for 2D or 3D, for structured or unstructured meshes, for commercial or in-house CFD models, and for surfaces of any shape and orientation. The method is demonstrated in ANSYS Fluent via user-defined functions (UDFs) written in the C programming language (see Appendix A and Appendix B). Validation is performed for a solar thermochemical reactor [38] receiving concentrated radiation from a high flux solar simulator (HFSS) [121].

4.2   Irradiated Surface Mapping

A point mapping algorithm is applied to ray intersections to translate absorbed irradiation from a MCRT model to boundary sources in a CFD model. The mapping for a group of $\vec{r}_k$ depicted as red points is given in Figure 4.1 for a solar reactor aperture and cavity. A detail view shows the mapping for two $\vec{r}_k$ on a single mesh face F_i of the CFD model. The $\vec{r}_k$ are transformed to a local, barycentric coordinate system $(\hat{t}_1, \hat{t}_2)$ on F_i to determine whether they fall within the boundaries of, and should be mapped to, F_i. The process is repeated until all $\vec{r}_k$ are sorted into a given F_i.
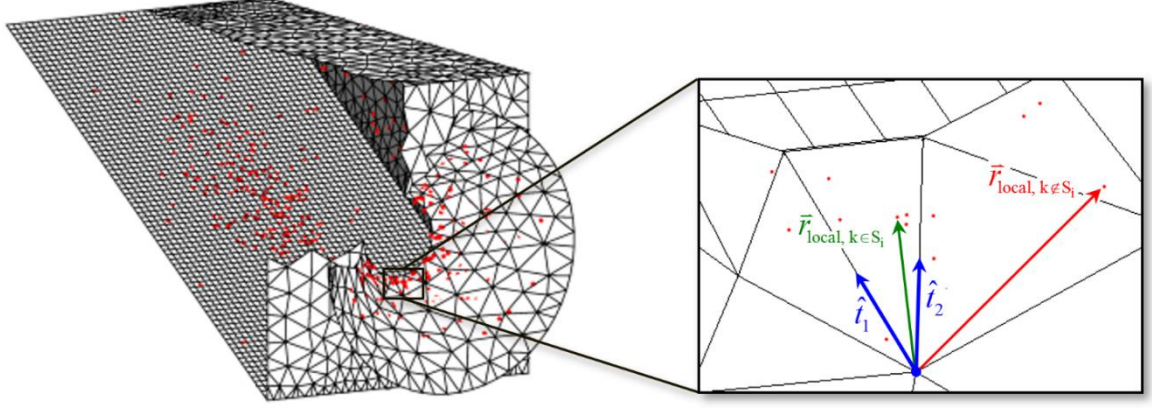
Figure 4.1 Monte Carlo ray tracing intersections (red points) on the surfaces of a solar reactor (left) overlaid on the computational mesh (black lines) to which the rays are coupled; and (right) a detail view of a mesh face on the reactor aperture with basis vectors of the local coordinate system (blue, not to scale) for ray mapping, as well as the position vectors of two ray intersections: one within the mesh face (green) and one not (red).

For triangular F_i, the local coordinate system origin is defined at any of the three F_i vertices, where the basis vectors $\hat{t}_1$ and $\hat{t}_2$ are unit vectors in the directions from the origin to each of the two remaining F_i vertices, respectively. For quadrilateral or greater F_i, the face is first subdivided into multiple triangular subcomponents which are each tested. The two-dimensional, local intersection position vectors are defined as:

$$\vec{r}_{\text{local}} = a\hat{t}_1 + b\hat{t}_2 \tag{4.3}$$

where (a,b) are the local coordinate dimensions. The subset of rays falling within F_i is defined by:

$$S_i = \left\{ k = 1, 2, \ldots, N_{\text{rays}} : a_{i,k}, \, b_{i,k} > 0, \, a_{i,k} + b_{i,k} \leq 1 \right\} \tag{4.4}$$

The direct mapping method is depicted in Figure 4.1 for two example intersections at the given F_i, where one intersection (green vector) falls within F_i and one (red vector) falls outside F_i.

CFD model boundary sources for each F_i are computed from mapped, summed ray energies as:

$$q''_{sun,i} = \left(\alpha G_0\right)_{sun,i} = \frac{1}{A_{s,i}} \sum_{k \in S_i} \dot{E}_k \qquad (4.5)$$

where $(\alpha G_0)_{sun}$ is the absorbed component of the surface irradiation profile $G_{0,sun}$; and A_s is the face surface area. The summation is limited only to the rays within the subset S. The boundary sources are incorporated into a general surface-fluid mixed boundary condition to the heat diffusion equation as:

$$-k_{n,i} \left.\frac{\partial T}{\partial n}\right|_{s,i} + q''_{sun,i} = U_i \left(T_{s,i} - T_{\infty,i}\right) + q''_{R,i} \qquad (4.6)$$

where the first term on the left-hand side is the conductive heat flux in the direction normal to the surface n and the first and second terms on the right-hand side are the convective and radiative heat fluxes, respectively. The convective heat flux has an overall heat transfer coefficient U to account for contact resistance and/or thin-wall conduction. The net radiative heat flux q''_R from internal reemission and reflection is computed via FV-RTE.

4.3   Participating Volumetric Cell Mapping

The method may also be applied to volumetric radiative absorption in a mesh, as the generalized mapping equation is readily extended to three dimensions. Globally-defined points of absorption $\vec{r}_k$ are transformed into a local, barycentric coordinate system $(\hat{t}_1, \hat{t}_2, \hat{t}_3)$ based on the tetrahedral mesh element C_i. For more complex element shapes, the C_i is first subdivided into M tetrahedral sub-elements which are each tested. Subdivision of a given element C_i and volumetric mapping of two $\vec{r}_k$, depicted as red points, are depicted in Figure 2, where the transparent surface bounds a sub-element.
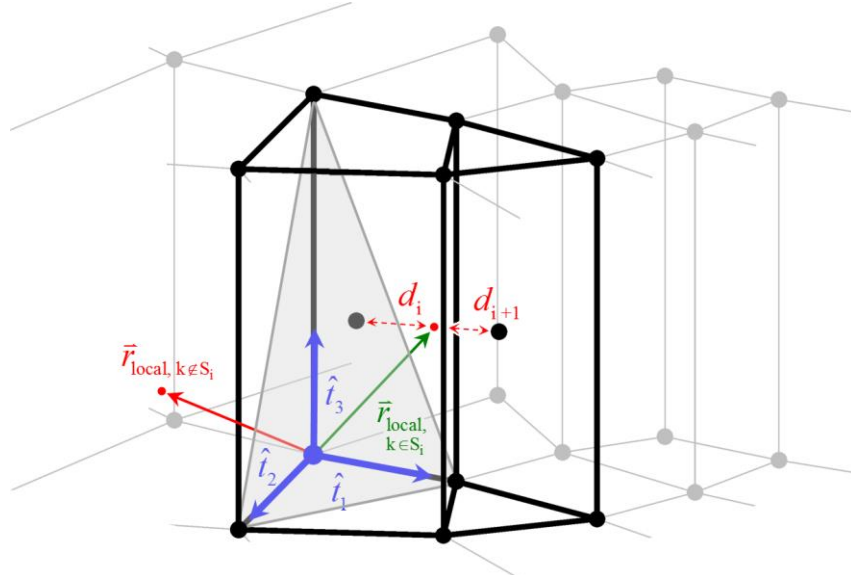
Figure 4.2 Monte Carlo ray tracing intersections (red points) within a discretized computational mesh (gray wireframe) to which the rays are coupled, with: 1) bases vectors of the local coordinate system (blue, not to scale) for a tetrahedral region (transparent gray surface) of a given cell (black lines); 2) position vectors of two ray intersections within the cell (green) and outside the cell (red); and 3) straight-line distances (red dashed) from one absorbed ray to the centroids of the cell and a neighbor (black wireframe).

The three-dimensional, local absorption point position vectors are defined as:

$$\vec{r}_{\text{local}} = a\hat{t}_1 + b\hat{t}_2 + c\hat{t}_3 \tag{4.7}$$

where (a,b,c) are the local coordinates. The subset of rays that fall within C_i is defined by:

$$S_i = \{k = 1, 2, \ldots, N : a_{i,k}, b_{i,k}, c_{i,k} > 0,\ a_{i,k} + b_{i,k} + c_{i,k} \leq 1\} \tag{4.8}$$

The direct mapping method is depicted in Figure 4.2 for two example intersections at the given C_i, where one intersection (green vector) falls within C_i and one (red vector) falls outside C_i.

Volumetric sources for each C_i are computed from mapped, summed ray energies as:

$$\dot{q}'''_{\text{sun},i} = \left(\kappa \int_{4\pi} I(s')\, d\Omega' \right)_{\text{sun},i} = \frac{1}{V_i} \sum_{k \in S_i} \dot{E}_k \tag{4.9}$$

where $\left(\kappa \int_{4\pi} I(\bar{s}')\, d\Omega' \right)$ is the absorbed component of the entering radiation from all directions $\bar{s}'$ and over all solid angles Ω' for a linear absorption coefficient κ; and V is the cell volume. The summation is limited only to the rays within the subset S. The volumetric heat sources are applied at each C_i as a term in the thermal energy transport equation, a common form of which is represented as:

$$\frac{\partial E_i}{\partial t} + \nabla \cdot \left(\rho \vec{V} h \right)_{\text{nb},i} = \nabla \cdot \left(k \nabla T_i \right) + q'''_{\text{sun},i} + q'''_{\text{R},i} \tag{4.10}$$

43

where the left hand side includes the transient and convected energy from neighboring fluid cells *nb*, and the right hand side captures heat diffusion and the two energy source terms: 1) q_{sun}''', and 2) the internal radiative balance computed via the FV-RTE q_R''.

4.4   Hybrid Nearest Neighbor/Barycentric Mapping

In a hybrid nearest-neighbor/barycentric direct mapping method, a neighborhood of the *n* nearest surface/volumetric elements to each $\vec{r}_k$ is identified. The barycentric mapping is applied exclusively to this neighborhood, significantly reducing computational cost. The nearest-neighbor algorithm used to identify the neighborhood, or subset of elements eligible for mapping, is defined as:

$$S_{n,i} = \left\{ k = 1, 2, \ldots, N_{rays} \,\middle|\, d_{i,k} \leq P_{d_i, n/N_{elements} \cdot 100\%} \right\} \tag{4.11}$$

where $P_{d_i, n/N_{elements} \cdot 100\%}$ is the percentile of the *n* nearest elements; and $d_{i,k} = \sqrt{\left\| \vec{r}_k - \vec{r}_{C_i} \right\|_2}$ is the straight-line distance between $\vec{r}_k$ and the cell centroid $\vec{r}_{C_i}$. For a sufficiently large neighborhood, the barycentric and hybrid methods produce identical mapping results.

It should be noted that, while an exclusively nearest-neighbor direct mapping would be computationally simpler than a barycentric or hybrid method, it could amplify discretization error and instability by erroneously mapping some rays to neighboring cells. This scenario is demonstrated in Figure 4.2 for the $\vec{r}_k$ within C_i: since $d_{i+1} < d_i$, nearest-neighbor direct mapping would map the $\vec{r}_k$ to the prism-shaped cell despite the $\vec{r}_k$ falling within C_i. Such errors are more likely to occur for meshes with high skew and large, abrupt

element size changes, biasing $\vec{r}_k$ toward nearby small cells. Therefore, the nearest neighbor/barycentric mapping hybrid method is suggested.

A flow chart detailing the algorithms for direct surface and volumetric mapping from the MCRT to CFD modeling domains is depicted in Figure 4.3a and b, respectively. Directions and example files for implementing the algorithm in ANSYS Fluent v19.0 are included in Appendix A and Appendix B.
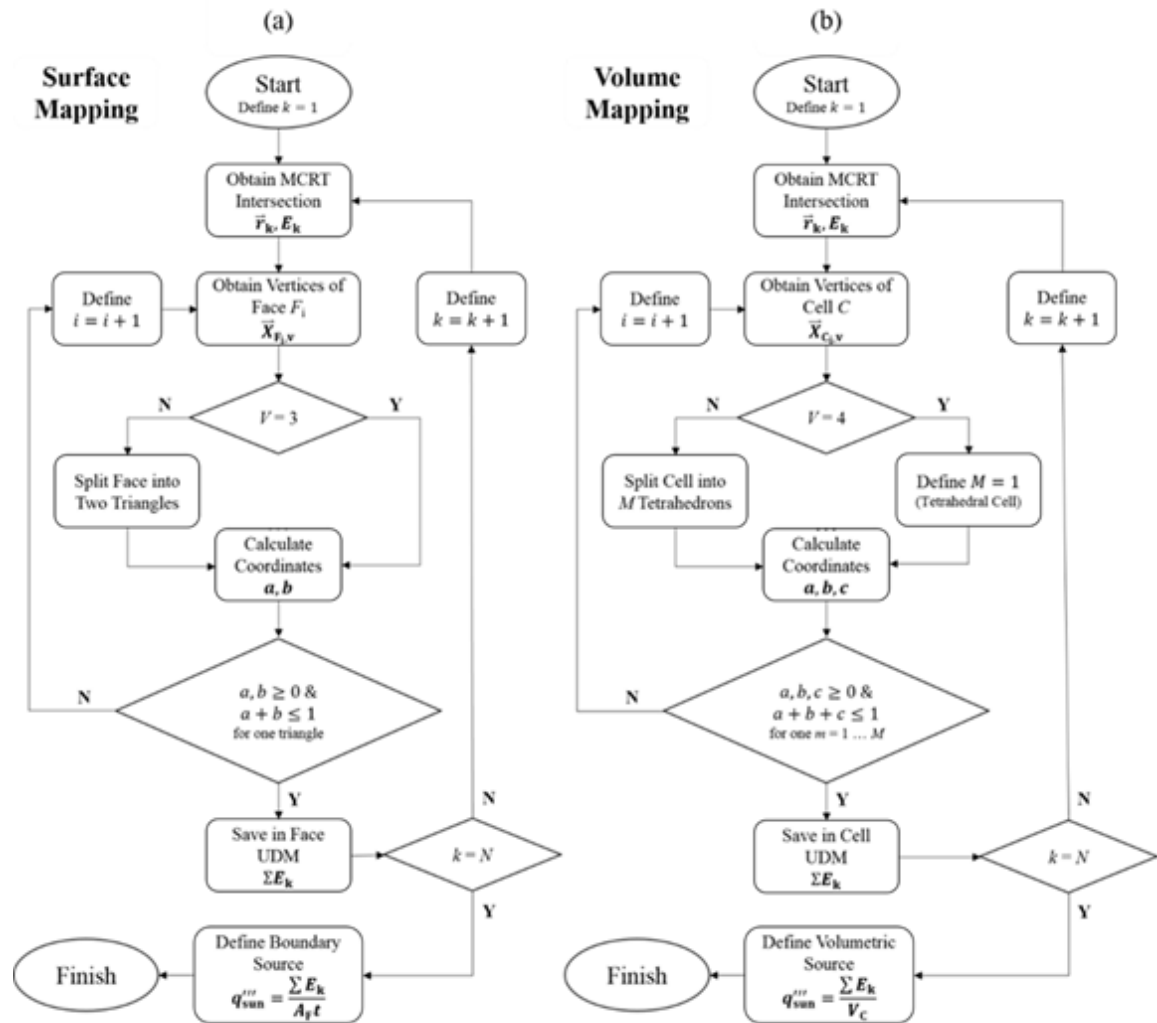
Figure 4.3 Flow charts for mapping of spatially-absorbed, incident irradiation for (a) surface and (b) volume geometries between Monte Carlo ray tracing and computational fluid dynamics modeling domains.

4.5   Modeling

Validation of energy conservation and preservation of spatial variation for the method was performed using the Solar Thermal Inclined Granular-Flow Reactor (STInGR), a 5 kW$_{th}$ windowed solar thermochemical reactor[2]. STInGR was designed for the reduction of redox-active metal oxides heated by input radiation from a HFSS [38], and the combined HFSS-STInGR system was modeled using an overlapping scheme. The 142 mm diameter, 5 mm thick quartz window was modeled as a specularly reflecting, non-scattering, participating medium [124]. The empty cavity and conical frustum were modeled as diffusely reflecting alumina surfaces.

The radiative input was modeled using a MCRT of a 6 kW$_{th}$ HFSS comprised of seven Xe arc lamps [121] with the aperture of STInGR aligned to the HFSS focal point and all emitted rays assumed to be within the visible spectrum. The MCRT predicted that 8.77 kW$_{th}$ of radiation was absorbed by STINGR surfaces or within the quartz window. The ray intersections from the MCRT were mapped to a CFD mesh produced in ANSYS Mesh for CFD models in ANSYS Fluent. The mesh consisted of 59209 unstructured triangular and quadrilateral face elements and 617 unstructured tetrahedral, hexahedral, and prismatic volumetric elements.

---

[2] The Solar Thermal Inclined Granular Flow Reactor and its computational models were developed by Andrew Schrader, with whom the MCRT-CFD mapping validation was performed in collaboration. More information on the reactor is given in:

    38.   Schrader, A.J., et al., *Solar electricity via an Air Brayton cycle with an integrated two-step thermochemical cycle for heat storage based on Co3O4/CoO redox reactions III: Solar thermochemical reactor design and modeling.* Solar Energy, 2017. **150**: p. 584-595.
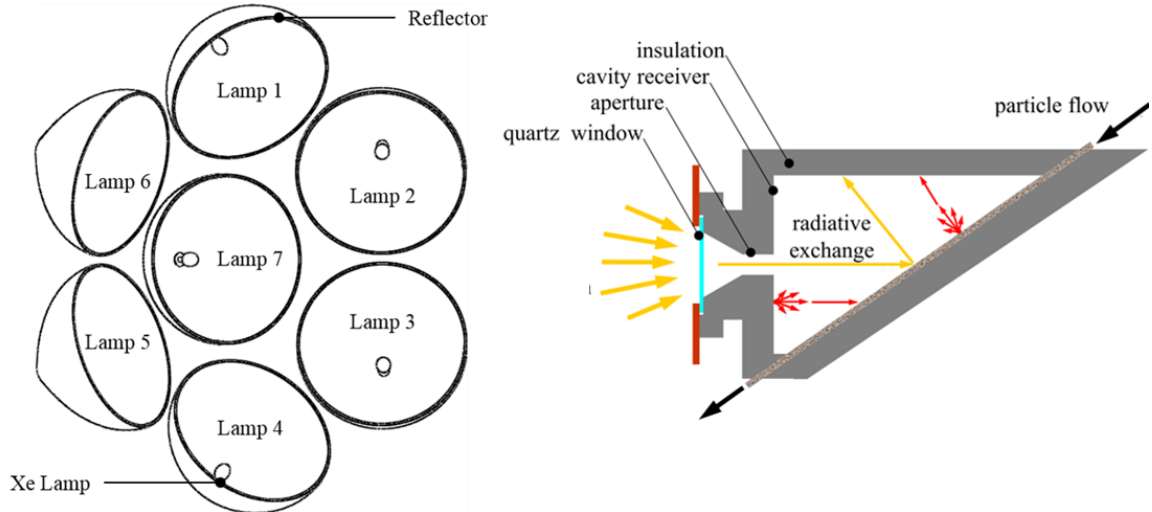
Figure 4.4. Schematic of the 6kW$_t$ high-flux solar simulator with seven Xe arc lamps mounted in truncated ellipsoidal reflectors, with the solar thermochemical inclined granular-flow reactor positioned at the reflector focal point.

Three case studies were performed to investigate preservation of spatial variation and energy conservation for direct mapping for three STInGR surfaces: the inclined slope, ceiling, and conical frustum, labeled as surfaces 1, 2, and 3 in Figure 4.5b, respectively. The direct mapping method was compared to the profile interpolation process in ANSYS Fluent. The $\vec{r}_k$ were binned to a structured grid to produce an irradiation flux profile which was interpolated to the CFD mesh. For surface 1, the CFD mesh was structured, so direct mapping would produce identical results to interpolation from an equally-fine MCRT grid. For surface 2, the CFD mesh was unstructured, so direct mapping would provide equal or better preservation of spatial variation and energy conservation. For surface 3, the CFD mesh was unstructured, the surface geometry was complex (conical), and the irradiation gradients were high due to proximity to the HFSS focal point. For this case, deficiencies in the binning, interpolation, and/or mesh resolution could produce significant energy losses.

To quantify spatial accuracy, MCRT surfaces were discretized as uniform, structured grids with approximately the same number of elements as the corresponding

47

meshed CFD surfaces. For each case study, the $\vec{r}_k$ were binned into the corresponding

MCRT grid using MATLAB to establish a common standard for comparing preservation

of spatial variation. For the profile interpolation method, these gridded data were input to

ANSYS Fluent as a profile which was internally interpolated to the CFD mesh. Separately,

$\vec{r}_k$ were input to the CFD mesh using the direct mapping method.

To quantitatively compare the energy conservation of both methods, the total

energy loss from the MCRT grid to the CFD mesh sources was calculated as:

$$P = \left| \left(\sum_i A_i q''_{sun,i} \right)_{CFD} - \left(\sum_j A_j q''_{sun,j} \right)_{MCRT} \right| \tag{4.12}$$

where i and j are the indices of CFD mesh and MCRT grid elements, respectively. To

quantitatively compare the spatial accuracy of both methods, the resulting CFD mesh

sources were linearly interpolated to the MCRT grid and the sum of square errors was

calculated as:

$$SSE = \sum_j \left(q''_{sun,j} \big|_{CFD} - q''_{sun,j} \big|_{MCRT} \right)^2 \tag{4.13}$$

For complete energy conservation and preservation of spatial variation, $P \rightarrow 0$ and $SSE \rightarrow$

0, respectively.

A final case study was performed on the solar thermochemical reactor quartz

window to demonstrate the application of the direct volumetric mapping algorithm to

participating media. As profile interpolation for volumetric sources was not supported in

48

ANSYS Fluent v19.0, the case study was instead compared to a simple, independent nearest-neighbor sorting algorithm as described in Section 2.2.

Side, isometric, and normal views to the solar reactor inclined slope are given in Figure 4.5a, b, and c, respectively. Each CFD mesh element is colored according to the absorbed irradiation, which was applied in ANSYS Fluent as a boundary source via the direct mapping method.
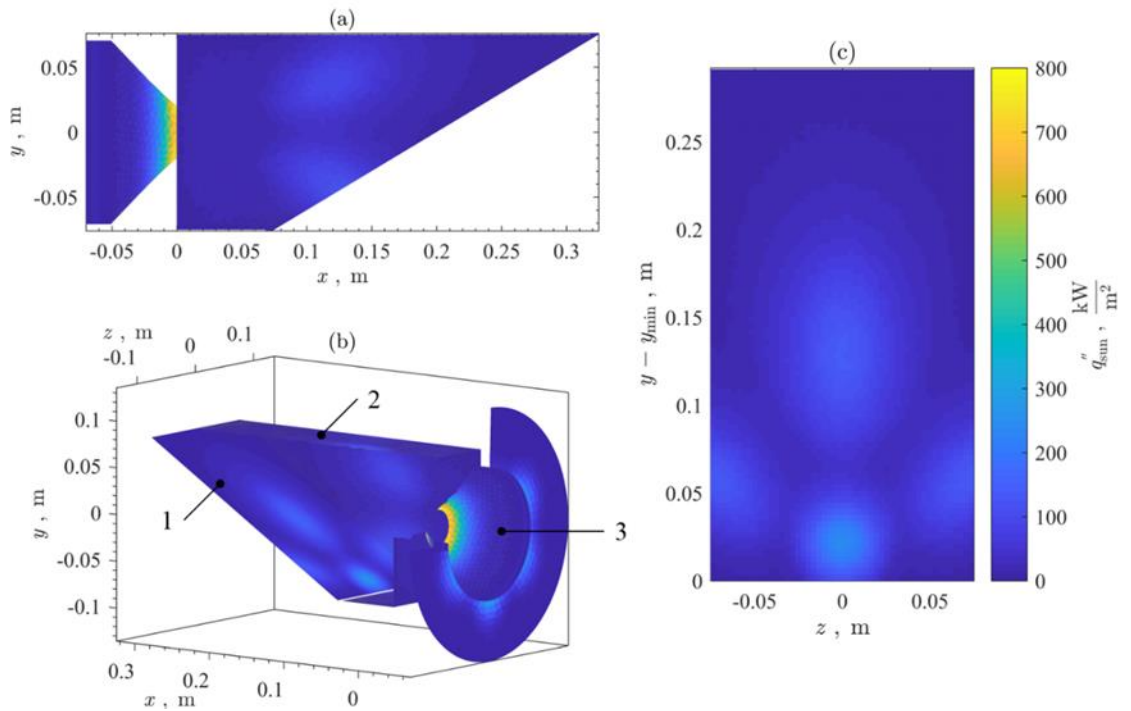
Figure 4.5 Side-view (a), isometric view (b), and normal view to inclined slope (c) of the unstructured computational fluid dynamics mesh for the solar thermochemical inclined granular-flow reactor, with each mesh face colored by the magnitude of mapped absorbed irradiation delivered by a seven-lamp high flux solar simulator using the direct mapping method.

In Figure 4.5 a-c, localized regions of highly concentrated absorbed irradiation from individual lamps are evident along the internal cavity and external front face surfaces. Localized regions of high absorbed irradiation were particularly evident along the inclined slope (1), as shown in Figure 4.5c, and would not have been captured by a uniform or

spatially-averaged heat flux profile. The total energy mapped to the reactor surfaces was $\sum_i \left(q''_{sun,i} A_i \right)$ = 8.29 kW$_{th}$. The total energy mapped to the quartz window was $\sum_i \left(q''_{sun,i} V_i \right)$ = 0.48 kW$_{th}$. A total of 8.77 kW$_{th}$ was mapped to the CFD mesh in ANSYS Fluent, meaning energy was conserved between the MCRT and CFD.

4.6 Case Studies

The first case study demonstrates a scenario in which the direct mapping method performs identically to previous methods. A normal view of the STInGR cavity inclined slope is given in Figure 4.6, where (a) shows the binned MCRT grid and (b-c) show the mesh elements colored by the magnitude of absorbed irradiation. The slope was discretized as a structured, uniform mesh in the CFD modeling domain with 4250 quadrilateral elements aligned with the MCRT grid. Four local regions of absorbed irradiation were captured in Figure 4.6a-c associated with individual HFSS lamps. Peak fluxes up to 300 kW$_{th}$·m^{-2} and a total absorbed power of 1.91 kW$_{th}$ were predicted.

In Figure 4.6b and c, nearly identical distributions of absorbed irradiation for the two methods were observed due to effectively exact alignment between MCRT grid and CFD mesh. Both methods achieved complete energy conservation ($P = 0$ kW$_{th}$) and high spatial preservation, with $SSE_{interp} = 0.003$ and $SSE_{map} = 0.711$, respectively. The spatial errors resulted solely due to differences in numerical precision between C and MATLAB, as no interpolation between modeling domains was required. Therefore, for structured meshes that align exactly to the binned MCRT grid, the direct mapping method is identical to the interpolated profile method.
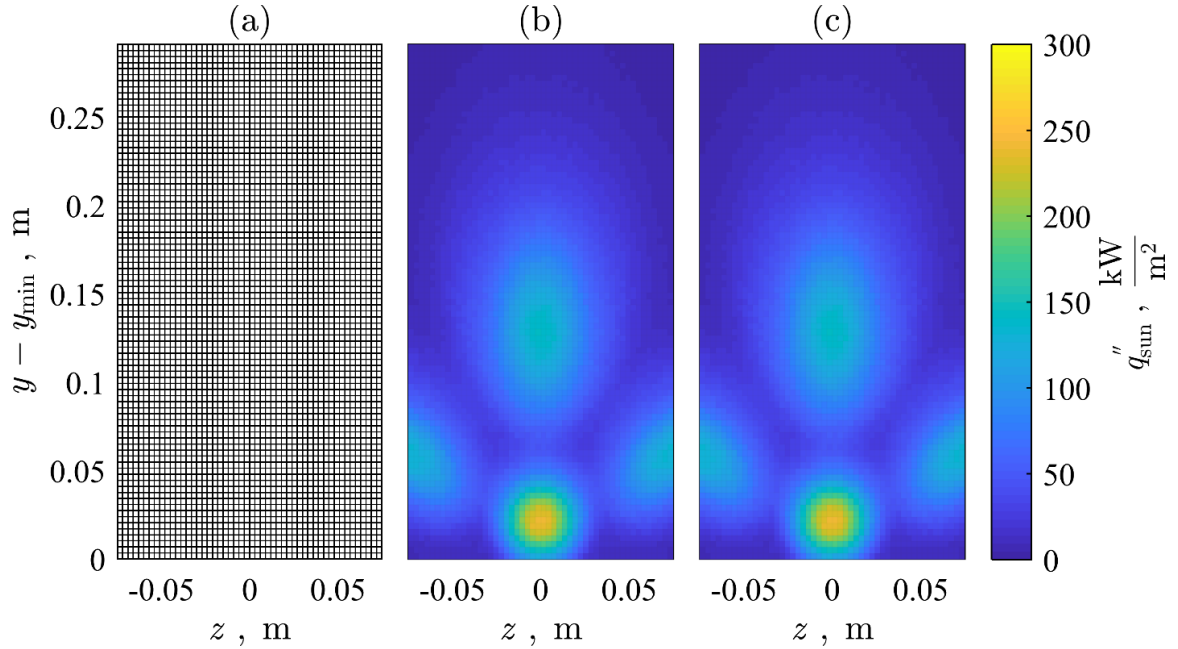
Figure 4.6 Normal view of reactor cavity inclined slope, with (a) the grid used to bin results from a Monte Carlo ray tracing of a seven-lamp high flux solar simulator to an absorbed irradiation profile applied as a boundary source in ANSYS Fluent using (b) the interpolated profile method, compared to (c) the direct mapping method; where each grid/mesh element is colored by the magnitude of absorbed irradiation.

The second case study demonstrates a scenario in which the direct mapping method is equal to or better than previous methods. A normal view of the meshed STInGR ceiling is given in Figure 4.7, where (a) shows the binned MCRT grid and (b-c) show the mesh elements colored by the magnitude of absorbed irradiation. The ceiling was discretized as an unstructured, non-uniform mesh in the CFD modeling domain with 2864 elements. Three local regions of absorbed irradiation were captured in Figure 4.7a-c, each associated with individual HFSS lamps. Peak fluxes up to 150 $kW_{th} \cdot m^{-2}$ and a total absorbed power of 0.97 kW_{th} were predicted.

In Figure 4.7b, some degradation in spatial accuracy using the profile interpolation method is evident, particularly for F_i with absorbed irradiation of 50–100 $kW_{th} \cdot m^{-2}$. The elliptical profile was slightly better preserved by direct mapping, as observed in Figure

4.7c. Spatial accuracy and energy conservation were achieved, respectively, to $SSE_{map} =$ 5.8 x10^3 < SSE_{interp} = 7.5x10^3 and P_{map} = 0 < P_{interp} = 0.004 kW$_{th}$. While both methods approximately preserved the spatial profile shape without significant energy losses, the new method achieved improved spatial accuracy and complete energy conservation.
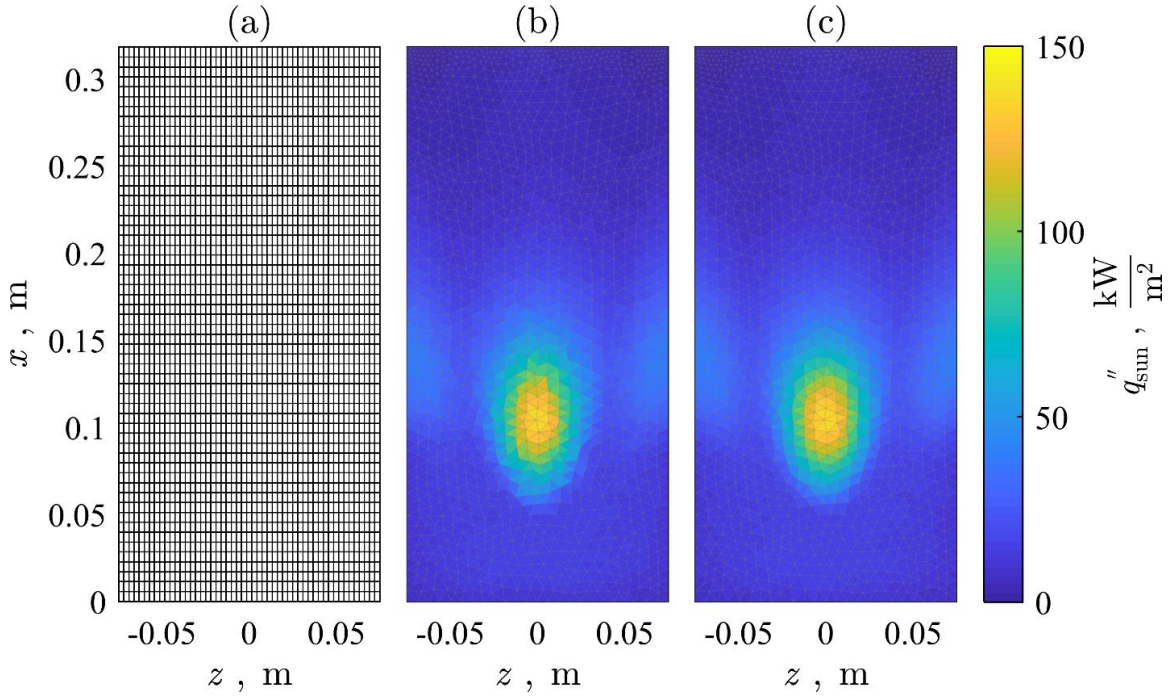
Figure 4.7 Normal view of reactor cavity ceiling, with (a) the grid used to bin results from a Monte Carlo ray tracing of a seven-lamp high flux solar simulator to an absorbed irradiation profile applied as a boundary source in ANSYS Fluent using (b) the interpolated profile method, compared to (c) the direct mapping method; where each grid/mesh element is colored by the magnitude of absorbed irradiation.

The third case study demonstrates a scenario in which the direct mapping method not only preserves spatial accuracy better than previous methods but is critical to prevent significant energy losses. A normal view of the STInGR aperture, a conical frustum shape, is given in Figure 4.8, where (a) shows the binned MCRT grid and (b-c) show the mesh elements colored by the magnitude of absorbed irradiation, with an inset in the bottom right of (b) presented to show the spatial variation. The frustum was discretized as an unstructured, non-uniform mesh in the CFD modeling domain with 1182 elements. An

approximately radially-uniform absorbed irradiation profile is shown in Figure 4.8a-c due a 2.3 kW$_{th}$ spillage of concentrated radiation from the HFSS around the aperture.

While the direct mapping method qualitatively preserved the spatial profile shape slightly better than profile interpolation, there was a mismatch between the locations of the MCRT grid and CFD mesh elements, and between the total surface areas in the MCRT grid (0.022 m^2) and CFD mesh (0.020 m^2), due to approximation of conical surface as planar faces in the mesh. This mismatch prevented a meaningful quantitative *SSE* comparison before and after mapping.

A significantly smaller magnitude of absorbed irradiation was observed in Figure 4.8b compared to Figure 4.8c due to the highly concentrated irradiation in the focal plane. High flux gradients near the aperture led to underestimation during interpolation, which produced a maximum $q''_{sun} = 15 \ll 800$ kW·m^{-2}, as shown in the inset. Energy conservation analysis resulted in $P_{map} = 0 < P_{interp} = 2.25$ kW$_{th}$. This result demonstrated that methods such as profile interpolation may introduce large errors in energy conservation depending on: 1) the irradiation gradient and 2) MCRT grid/CFD mesh resolutions. Direct mapping, however, is robust even for sharp irradiation profiles and/or coarse meshes.
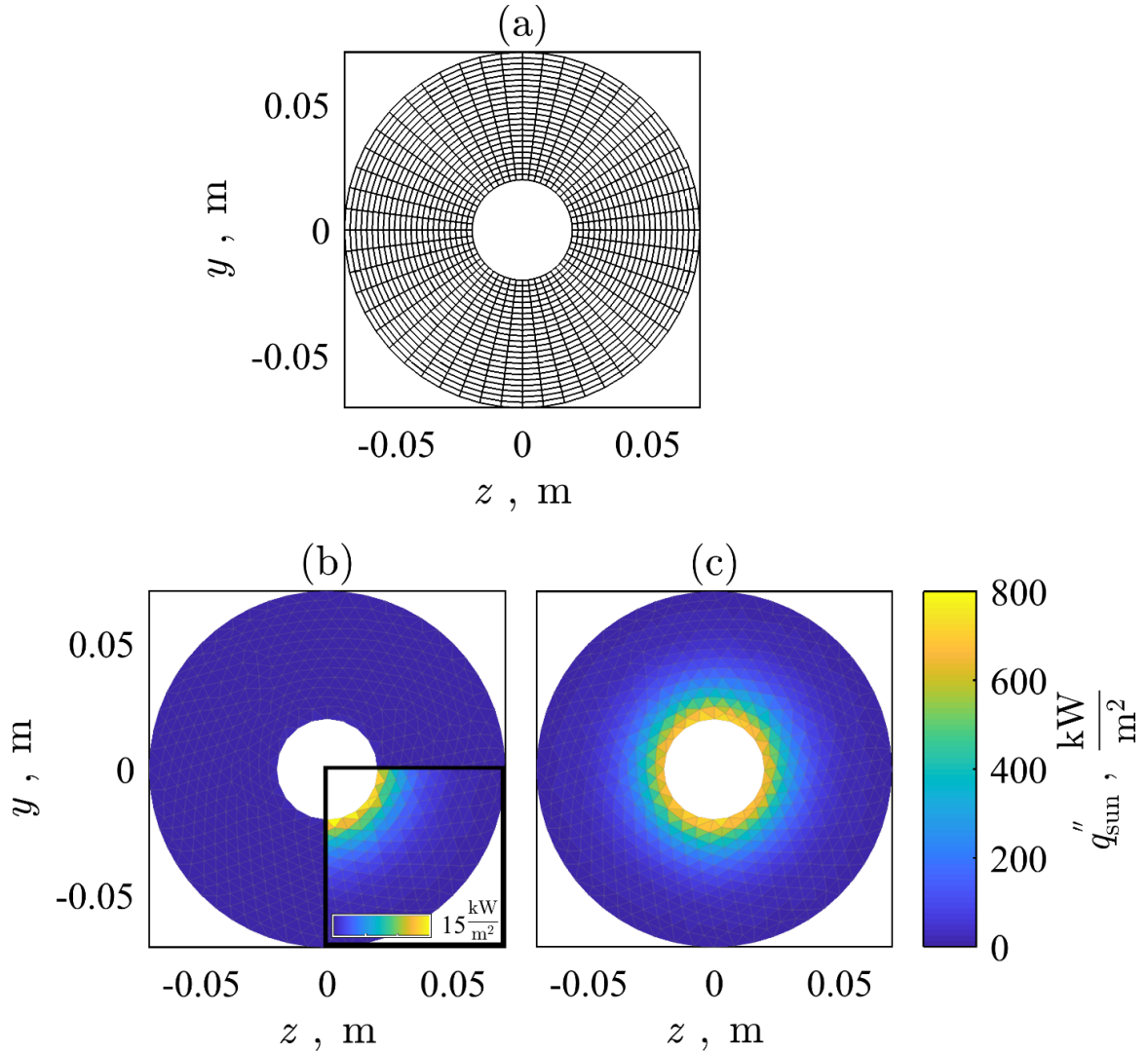
Figure 4.8 Normal view of reactor conical frustum, with (a) the grid used to bin results from a Monte Carlo ray tracing of a seven-lamp high flux solar simulator to an absorbed irradiation profile applied as a boundary source in ANSYS Fluent using (b) the interpolated profile method, compared to (c) the direct mapping method; where each grid/mesh element is colored by the magnitude of absorbed irradiation, and a quarter inset on (b) shows the maximum flux of 15 kW·m^{-2} from the interpolated profile method.

Comparison of mapping methods for the three studies pictured in Figure 4.6-8 demonstrated the inherent energy conservative nature of the direct mapping method, with spatial accuracy dependent upon discretization accuracy of the modeled geometry. The method was also demonstrated to be independent of the non-trivial process of matching gridded MCRT and meshed CFD modeling domains. Direct mapping achieved equivalent

accuracy to the interpolated profile method for aligned MCRT grids/CFD meshes and improved accuracy for misaligned MCRT grids/CFD meshes.

An additional case study was performed to demonstrate the direct mapping method for participating media and to show the method's improved performance over the independent nearest-neighbor algorithm. A view of the STInGR window depicting the unstructured CFD mesh cell centroids is given in Figure 4.9a and b. Each cell is colored according to the volumetrically absorbed radiation, which was applied in as a volumetric heat source in ANSYS Fluent using the (a) nearest neighbor and (b) barycentric direct mapping algorithms, respectively.
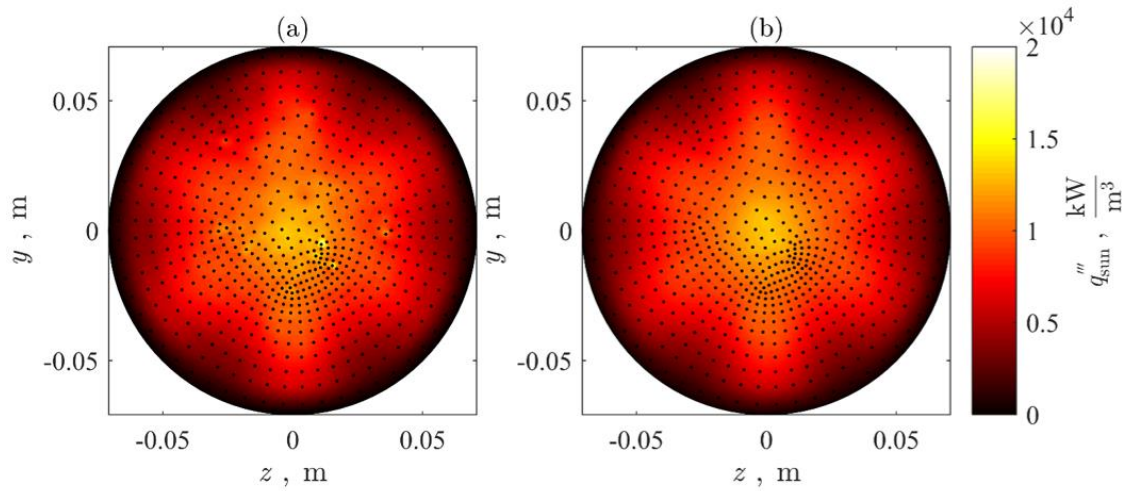
Figure 4.9 Normal view to 5 mm thick quartz window of computational fluid dynamics volumetric cell centroids, with each cell centroid colored by magnitude of mapped volumetric, absorbed irradiation delivered by a seven-lamp high flux solar simulator using (a) nearest-neighbor and (b) barycentric direct mapping methods.

Using both algorithms, the profile of the seven-lamp HFSS, roughly symmetric about (0,0), was visible. In Figure 4.9a, however, localized C_i of high or low q_{sun}'' not present in (b) are evident. The differences were the result of ray misappropriation by the

nearest neighbor algorithm for neighboring cells with significant volume differences. The most prominent example of ray misappropriation in Figure 4.9a occurred at the cell centroid near (0.01,0), producing to a localized hotspot of $q_{sun}'' \approx 1.9 \times 10^4 \, kW/m^3$. The centroid and corresponding meshed element is pictured in greater detail in Figure 4.2 as element C_{i+1}. In Figure 4.9b, the q_{sun}'' profile was smoother as a result of the barycentric mapping algorithm, indicating improved mapping between the MCRT and CFD modeling domains.

Based upon the methodology and various case study observations, the advantages and disadvantages of the method are summarized in the following subsections. Note that all disadvantages are also true for other overlapping modeling domain schemes.

4.7   Advantages

1) The method is energy conservative between the MCRT and CFD modeling domains.

2) The method is spatially accurate to within the MCRT and CFD discretization accuracies.

3) The method is compatible with structured and unstructured meshes of arbitrary polygonal or polyhedral construction, for two and three dimensions.

4) The method uses an algorithm that is programmatically simple and may be applied using an external code or directly within ANSYS Fluent via UDFs (see Appendix A and Appendix B).

5) The method requires that the MCRT run only once for a given geometry and radiative conditions, even when performing CFD mesh refinement.

4.8   Disadvantages

1) Transient mapping is cumbersome using the method. Such cases occur for overlapping schemes with participating media in the band(s) of the radiative solar input. Non-overlapping domains or MCRT/FV-RTE models with a single computational domain may therefore be more appropriate for media with highly temperature-dependent absorption, transmission, reflection, or scattering.

2) Systematic errors in the absorbed heat flux distribution are introduced by approximating curved geometries from the MCRT model with polygonal elements in the CFD model.

3) The method utilizes boundary sources for surface elements, which introduces additional conductive resistance at the interface between two modeled regions in ANSYS Fluent models. However, the additional resistance becomes negligible for a sufficiently thin boundary.

4.9   Conclusions

A method for mapping the results from radiative transport models using Monte Carlo ray tracing to computational heat transfer models was presented. The direct mapping method allows for the input of two- and three-dimensional radiative absorption on structured or unstructured meshes. The method differs from previous documented attempts in that it may be rapidly implemented and not only maintains energy conservation between the two modeling domains, but also preserves spatial irradiation profiles to within mesh precision.

Energy conservation and preservation of spatial variation by the direct mapping method was demonstrated for a windowed solar thermochemical reactor with input radiation from a high flux solar simulator. The method captured local hotspots from individual lamps and demonstrated that the net energy absorption was equal before and after direct mapping from the Monte Carlo to the CFD mesh. The method was demonstrated to preserve spatial variation and maintain energy conservation as well or better than previous methods for various complex geometries and mesh types. Most important, the method successfully mapped absorbed irradiation around the reactor aperture while a previous method resulted in energy losses of multiple kW$_{th}$. Therefore, the direct mapping method is a valuable and, in some scenarios, critical tool for accurately capturing the highly directional and spatial nature of concentrating solar inputs.

CHAPTER 5. UFR DESIGN & CHARACTERIZATION

5.1   Introduction

An upward flow reactor (UFR) coupled to a high-flux solar simulator (HFSS) is presented to overcome the limitations of TGA for capturing the transient reaction behavior of rapidly-thermally reducing materials. The UFR provides rapid heating to study thermal reduction under conditions similar to those in a directly-irradiated solar thermochemical reactor under vacuum. Robust modeling was employed using Monte Carlo ray tracing (MCRT)[3] to model the radiative heat transfer from the HFSS to the UFR. These results were mapped in a decoupled manner to a computational fluid dynamics model that simultaneously solved the continuity, momentum, and energy equations coupled to finite volume radiative transfer within the reactor in ANSYS Fluent v15.0.7 [125].

Thermal reduction of a binary metal oxide, Co_3O_4, was performed to experimentally validate the UFR models. As the thermal transport and radiative properties of Co_3O_4 are well-characterized, and as Co_3O_4 kinetics have been studied via TGA, the material was a convenient choice for initial validation of the UFR, prior to future investigations of thermal reduction behavior for novel materials. The temporal and spatial temperature changes in the packed Co_3O_4 bed were determined, and the reaction rates were measured by temporally monitoring the O_2 evolution from the sample via mass spectrometry. A correction procedure that accounted for dispersion was implemented by

---

[3] Monte Carlo ray tracing of the high-flux solar simulator, as well as extension of the method to include the beamdown mirror and quartz dome of the upward flow reactor, was performed by Robert Gill.

using tracer studies to determine a reactor system residence time distribution (RTD) function and then deconvolving the RTD with measured O_2 flow rates.

The combined computational-experimental UFR characterization provides high-resolution temporal, spatial determination of sample temperatures and reduction and is a first step toward the use of the UFR for the evaluation of materials with reaction rates unsuitable for TGA.

5.2   Design

An UFR capable of vacuum operation was designed and fabricated for operation in conjunction with a HFSS. The UFR was constructed to operate in an upflow configuration for thermal reduction experiments, similar to traditional TGA [126], to minimize recirculation zones and avoid buoyancy effects. The vacuum operation of the reactor further mitigated these phenomena and, therefore, mitigated the impacts of lag and dispersion on experimental measurements.

An exploded view of the UFR is schematically depicted in Figure 5.1. The transparent domed-tube (component 1) was fabricated from a fused quartz cylinder (Technical Glass Products 57 mm ID x 61 mm OD) with a hemispherical top and 6 mm OD, 229 mm long outlet stem. The domed-tube was sealed to a stainless steel adapter (Kurt J Lesker 304L SS Half Nipple QF50-200-LF) (component 4) with fit-over compression by a series of FKM o-rings (Chemical-Resistant Viton® Fluoroelastomer 51 mm ID x 57 mm OD) (component 3). The FKM was temperature-rated for a maximum of 204°C [127], so an equal-sized aluminum foil ring was placed above the o-rings as a shield from incoming thermal radiation. The adapter was joined to a stainless steel reactor body (Kurt J Lesker

304L SS Full Nipple QF50-200-N) (component 5) via a cast clamp (Kurt J Lesker 304L SS QF50-200-CS), FKM o-ring, and centering ring assembly (Kurt J Lesker Centering Ring with Fluorocarbon O-ring QF50-200-SRV) (component 6a). The same assembly (component 6b) was used to connect a custom gas and thermocouple feedthrough (Kurt J Lesker CF-150220A) (component 7) to the bottom of the reactor body. The feedthrough contained three 6 mm OD equiangular Ar inlet pipes placed close to the outer edge of the reactor cavity in order to minimize the stagnation zone below the crucible. At the feedthrough center, a fourth 6 mm OD pipe was used to penetrate the UFR bottom and extend into the reactor to act as a mounting stem for a custom-molded 37 mL bored-through alumina crucible (component 2) (AdValue Technology AL-C-C-GIT).
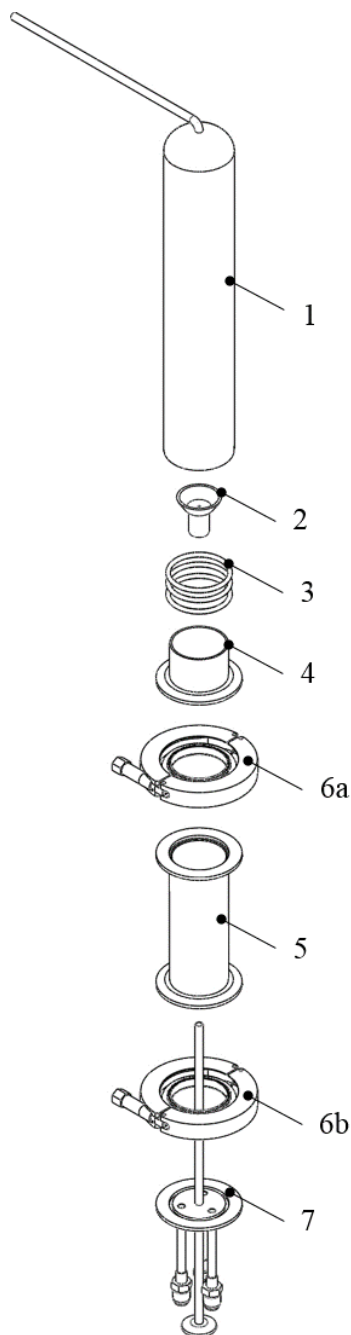
Figure 5.1 Exploded wireframe view of the upward flow reactor with (1) domed quartz tube, (2) alumina crucible, (3) o-rings, (4) stainless steel adapter, (5) stainless steel body, (6) cast clamps, and (7) gas/thermocouple feedthrough.

During experimentation, the UFR was mounted in front of a high-flux solar simulator (HFSS) as shown in Figure 5.2. A small mass of sample, comparable to TGA experiments, was loaded onto a thin platinum foil (Sigma-Aldrich 0.025MM Thick 99%

Pt Foil 267244-1.4G) that was placed in an alumina crucible mounted in the focus of the HFSS. Ar and sometimes O_2 (to adjust the overall O_2 partial pressure) were introduced via flow controllers (FC: Bronkhorst F-201CV-20K-MAD-33-V) to the UFR, and an oil-free vacuum pump (Edwards Oil-Free Scroll Pump 7.5 CFM 0.007 mbar NXDS10I-1PH) was employed to reduce the total pressure in the system as measured by a pressure transducer (Omega Solid State Pressure Transducer Vacuum to 300psi PX209-30Vac10V).

After the air was purged from the system, concentrated irradiation from the HFSS was redirected downward through the quartz tube to the sample by a 45°, water-cooled, polished aluminum mirror. The flow entering from the bottom of the UFR transported the evolved O_2 away from the sample through the top of the quartz tube via advection and buoyancy. O_2 concentrations in the exit flow were temporally measured using a combination of mass spectrometry (MS, OmniStar ThermoStar GSD320 Gas Analysis System) and gas chromatography (GC, Agilent 490 Micro GC equipped with Molsieve and PoraPLOT Q columns). The temperature in the sample was temporally monitored using a Type K thermocouple (Omega OMEGACLAD XL Type K KQXL-116) The reduction temperature was controlled by varying the electrical input to the xenon arc lamp via a potentiometer prior to ignition to increase/decrease the concentrated irradiation to the sample.
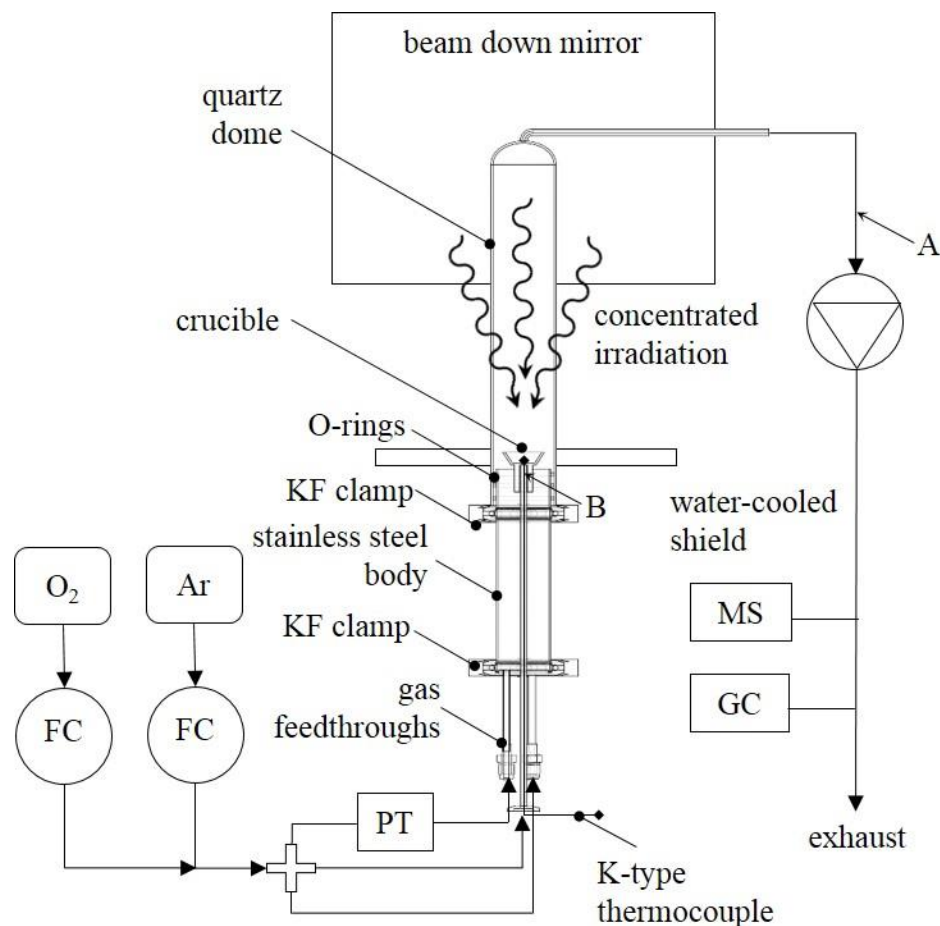
Figure 5.2 Schematic of experimental setup: O_2 and Ar tanks supplied gas to the reactor via flow controllers (FC), driven by a pump downstream of the reactor outlet. A pressure transducer (PT) was used to monitor reactor operating pressure and products of reduction were measured via a mass spectrometer (MS) and gas chromatograph (GC). Labels A and B indicate locations at which the O_2 flow controller and supply were connected for dispersion testing.

5.3   Modeling

Steady, incompressible, laminar CFD modeling was performed with an unstructured mesh to characterize heat transfer and flow through the UFR, including the cavity, crucible, and sample bed. Second-order upwind discretization methods were used to capture advective transport in the momentum and energy equations, and a second-order method was used for pressure. A Green-Gauss, node-based gradient method was employed for calculating cell face values, and the SIMPLE scheme was used for pressure-velocity

coupling. Thermophysical properties for a reacting Co_3O_4 bed at high temperatures were calculated using porous media models[4]. Transient modeling under the same conditions and methodology was also performed, using a first-order implicit method with initial conditions determined via a separate steady-state model with no heat input.

Reflection and refraction by the quartz tube during HFSS operation prevented an experimental determination of spatial irradiation on the sample. Therefore, to model radiative input from the HFSS, the HFSS lamps MCRT from [129] was modified to include reflection by the beam down mirror and transmission through the quartz tube. A random, unbiased slope error with standard deviation of 5.0 mrad [130] was introduced for the mirror to account for visible imperfections (bubbles or ripples) in the polished surface. A total reflectivity for the mirror of 0.93 was calculated from spectral aluminum surface properties [131], approximating HFSS irradiation as originating from a blackbody at 5777 K. The quartz tube was idealized as a constant-thickness slab with total, hemispherical surface properties defined by the shorter-wavelength band in Table 5.1 and a refractive index of 1.3.

Table 5.1 Two-band model for the quartz tube transmissivity and absorptivity [132].

λ, μm	τ, -	α, -
0-4	0.93	0
4-∞	0	0.9

---

[4] Porous media model selection was informed by the Master's thesis of Karl-Philipp Schlichting, a collaborator on the project. More information may be found in:

    128. Schlichting, K.-P., *Parametric Study of the Temperature Distribution of a Packed-Bed Subjected to Concentrated Irradiation*, in *Department of Mechanical Engineering*. 2015, Eidgenössische Technische Hochschule Zürich (Swiss Federal Institute of Technology). p. 142.

Radiative fluxes on the surfaces of the crucible and holder assembly were predicted via MCRT, while initial absorptions at other locations in the reactor were neglected due to the reduced radiative flux at distances further from the focal point. Absorbed rays were binned into a radial MCRT coordinate system to produce fluxes and linearly interpolated to increase the flux map resolution, which was verified to produce comparable results to MCRT-CFD mapping for the UFR geometry. Experimental flux mapping in the HFSS focal plane as described in [121] was performed for the centermost HFSS lamp with an input power of 4.23 kW$_e$, as was used in experimentation. The spatial flux map within a 40mm circular area around the focal point was integrated to determine the total input radiation and calibrate MCRT results. These high-resolution fluxes were introduced to the energy model through steady, spatially varying boundary sources at the corresponding surfaces in a nearest-neighbor manner.

All non-quartz surface properties were assumed temperature independent, and re-emission was not modeled via ray tracing, allowing the MCRT to be decoupled from other computational modeling and making it unnecessary to re-compute the absorbed fluxes at each iteration. Radiative heat transfer within the reactor due to re-emission was modeled using a second-order upwind finite volume discretization of the radiative transport equation in three spectral bands to account for transmission, absorption, and diffuse reflection at the quartz tube and spectral sample surface properties. All UFR components except the quartz tube were approximated as diffuse, gray surfaces. The fluid volume within the reactor was assumed to be non-participating.

Heat transfer within the 2mm porous sample bed was modeled using energy conservation, represented as:

$$(\rho c)_{pm} \frac{\partial T}{\partial t} = \nabla (k_{eff} \nabla T) + \dot{S}_h \tag{5.1}$$

where $(\rho c)_{pm}$ is the porous media thermal capacitance; T is temperature; t is time; k_{eff} is total effective thermal conductivity in the bed; and $\dot{S}_h$ is a heat sink accounting for the endothermicity of the Co_3O_4 thermal reduction and defined for each cell and timestep, given as:

$$\dot{S}_{h,i}^p = r_i \left(\rho_{pm,i} \frac{\Delta H_{Co_3O_4}}{M_{Co_3O_4}} \right) \tag{5.2}$$

where i is the cell index; p is the current timestep; ρ_{pm} is the porous media density; M is molar mass; ΔH is the enthalpy of reaction; where the reaction rate was determined as

$$r_i = \frac{\partial \alpha}{\partial t}\bigg|_i = \begin{cases} f(\alpha_i, T_i) & , \ T_i \geq T_{\Delta G=0} \\ 0 & , \ T_i < T_{\Delta G=0} \end{cases} \tag{5.3}$$

where α is the conversion from Co_3O_4 to CoO and O_2; and $\Delta G = 0$ denotes the state at which the cell temperature and O_2 partial pressure are sufficient for spontaneous reactions. For an experimentally measured O_2 partial pressure of ~0.5 mbar and under the assumption of complete reaction, $\Delta H = 203.6 \ kJ \cdot mol^{-1}$ and $T_{\Delta G=0} = 1025.5$ K. r is the reaction rate, or the time rate of change of Co_3O_4 conversion α: a function of time and temperature T as proposed by [23] under the assumption of negligible O_2 partial pressure dependence.

The porous media density and porous media thermal capacitance were defined for each cell, respectively, as:

$$\rho_{pm,i} = \left(1-f_v\right)\rho_f(T_i) + f_v\rho_s \tag{5.4}$$

and

$$\left(\rho c\right)_{pm,i} = \left(1-f_v\right)\rho_f c_f(T_i) + f_v\rho_s c_s(T_i) \tag{5.5}$$

where ρ_f and ρ_s are the fluid and solid densities, respectively; f_v the solid volume fraction; and where $c(T)$ is temperature-dependent specific heat, taken from compiled Shomate equation forms for Co_3O_4 and CoO [133]. The total effective thermal conductivity for each cell accounting for optically thick radiative heat transfer and porous media heat transfer was determined as:

$$k_{eff,i} = k_{pm,i} + k_{r,i} = k_{pm,i} + \frac{16}{3\beta_{dep}}\sigma T_i^3 \tag{5.6}$$

where k_{pm} is the porous media effective conductivity [134]; k_r is the radiative-conductivity determined from the Rosseland diffusion approximation for optically thick media [87]; β_{dep} is the dependent scattering extinction coefficient; and σ is the Stefan-Boltzmann constant. Local thermal equilibrium was assumed for the porous media [135] and convection in the porous zones was neglected due to the low flow rates in the reactor and the sweep-over rather than flow-through configuration of the sample crucible. The inaccuracy of the Rosseland diffusion approximation near the irradiated boundary was assumed minor due to the high f_v. Previously, comparison to MCRT for a more porous, direct-irradiated

medium at high solar concentrations suggested the approximation had only a small effect on average temperature [114].

Table 5.2 contains a list of all relationships used to determine k_{eff} along with the related correlations.

Table 5.2 Parameters for the sample bed effective thermal conductivity.

Parameter	Definition	Source
Dependent scattering extinction coefficient	$\beta_{\text{dep}} = \gamma \beta_{\text{ind}} = \gamma Q_{\text{ext}} f_v \dfrac{3}{2d_p}$	Eq. 12.29 [87], [136]
Correction factor	$\gamma = 1 + 1.84 f_v - 3.15 f_v^2 + 7.20 f_v^3, \quad f_v < 0.7$	Eq. 5 [136]
Extinction efficiency, geometric optics	$Q_{\text{ext}} = 2, \quad \dfrac{\pi d_p}{\lambda} \gg 1$	Eq. 12.63 [87]
Porous media effective conductivity ratio, porous medium	$\dfrac{k_{\text{pm}}}{k_f} = 1 - \sqrt{f_v}\left(1 - \dfrac{k_c}{k_f}\right)$	Eq. 8 [137]
Deformation-dependent particle conductivity ratio	$\dfrac{k_c}{k_f} = \dfrac{2}{B}\left[\dfrac{B}{\mu^2}\dfrac{k_p - k_f}{k_p}\ln\left(\dfrac{k_p}{k_f B}\right) - \dfrac{B+1}{2} - \dfrac{B-1}{\mu}\right],$ $\mu = 1 - \dfrac{k_f B}{k_p}, \quad k_p = 10 \text{ W} \cdot \text{m}^{-1} \cdot \text{K}^{-1}$	Eq. 17 [137], [138, 139]
Particle deformation parameter approximation	$B = 1.25\left(\dfrac{f_v}{1 - f_v}\right)^{10/9}$	Eq. 7 [137]

A three-level sensitivity study was performed in order to determine the effects of variations in solid particle thermal conductivity k_p.

During transient simulations, all thermophysical properties for the solid particles in the porous bed were defined as a homogenous mixture of Co_3O_4 or CoO according to α for a specific cell, given as:

$$\theta_{p,i} = (1-\alpha_i)\theta_{Co_3O_4} + \alpha_i\theta_{CoO}$$

(5.7)

where θ is a generic thermophysical property. Complete conversion to CoO was assumed for all steady-state analysis.

Heat transfer through the outer reactor walls was approximated as one-dimensional conduction through constant thickness, homogenous material slabs. A temperature boundary condition equal to the ambient temperature (T_∞) was imposed for the steel body outer surface based upon its location below the water-cooled shield and distance from the focal point (Figure 5.2). A mixed radiative/convective boundary condition was imposed at the quartz tube outer surface, assuming gray, diffuse behavior. An overall convective heat transfer coefficient was used, approximating the surface geometry as a cylinder, given as:

$$h = \frac{\overline{Nu_L}k}{L}$$

(5.8)

where L is the cylinder height; k is the air conductivity; and $\overline{Nu}_L$ is the Nusselt number for free convection over a long, isothermal cylinder [140, 141]:

$$\overline{Nu}_L = \frac{4}{3}\left[\frac{7Ra_L \, Pr}{5(20+21Pr)}\right]^{1/4} + \frac{4(272+345\,Pr)L}{35(64+63\,Pr)d}$$

(5.9)

where Pr is the Prandtl number; d is the cylinder outer diameter; and Ra_L is the Rayleigh number, determined from an estimated average surface temperature T_s. This temperature was estimated from early model runs for the quartz tube with simplified boundary conditions.

Pressure and mass-flow boundary conditions were defined from average experimental measurements. For all non-quartz components, gray, diffuse surfaces were assumed, and surface properties were obtained from tabulated data when available [87]. The domain, mesh, and boundaries defined for modeling are shown in Figure 5.3, and the associated boundary conditions are given in Table 5.3, where all unlabeled boundaries are described by No. 6.
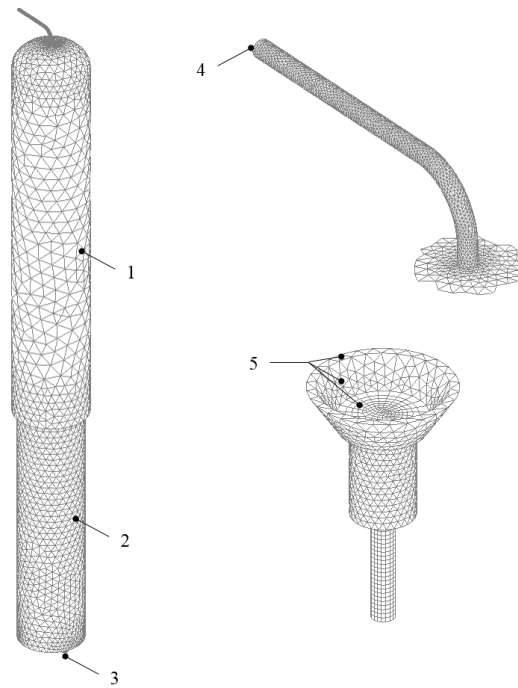
Figure 5.3 Mesh for upward flow reactor computational fluid dynamics and heat transfer modeling. The outer surface (left), outlet stem (top right), and sample crucible inside the reactor (bottom right) are depicted with annotations matching the boundary conditions in Table 5.3.

Table 5.3 Boundary conditions for reactor heat and mass transfer modeling.

№	Boundary	Material	Value(s)
1	no slip/penetration; multimode	quartz	$T_s = 500$ K $\varepsilon = \begin{cases} 0.93, & \lambda \geq 4 \ \mu m \\ 0, & \lambda < 4 \ \mu m \end{cases}$ $h = 1.563$ W·m^{-2}·K^{-1}
2	no slip/penetration; ambient temperature	stainless steel (304L)	$T_s = 300$ K $T_\infty = 300$ K
3	constant mass flow; ambient temperature	argon	$\dot{m} = 0.2974 \cdot 10^{-4}$ kg·s^{-1} $T_{in} = 300$ K $T_\infty = 300$ K
4	constant pressure; convective outlet	argon	$p_{out} = -87.5$ kPa
5	energy conservation	gas-solid interface	$\sum_i \dot{Q}_{HFSS} = 207$ W $\varepsilon_{Al_2O_3} = 0.26$ $\varepsilon_{pm} = \begin{cases} 0.68, & \lambda \geq 3 \ \mu m \\ 0.80, & \lambda < 3 \ \mu m \end{cases}$
6	temperature continuity; energy conservation	gas-solid, solid-solid interfaces	$\varepsilon = \begin{cases} 0.26, & Al_2O_3 \\ 0.36, & 304L \ SS \end{cases}$

Boundary heat sources were defined for specific surfaces (crucible top, crucible inner side wall, and sample top, each marked by Item 5 in Figure 5.3) based on MCRT. The emissivity of the Co_3O_4 and CoO sample bed was modeled via a two band-approximation, shown in Table 5.2, based upon surface property values for pure Co_3O_4 from literature [142] modified to account for packed bed enhancement [143], which for diffuse, gray bands resulted in a sample bed absorptivity of $\alpha_{pm} = \varepsilon_{pm}$ in each band. A three-level sensitivity study was performed in order to determine the effects of variations in α_{pm}.

To account for axial dispersion in the UFR, O_2 flows were introduced in separate experiments upstream and downstream of the UFR and the temporal concentrations were measured using a combination of MS and GC. The residence time and dispersion effects were accounted for by determining a residence time distribution E(t), given implicitly as:

$$C_{MS}(t) = \int_0^t C_{O_2}(t-t')E(t')dt'$$

(5.10)

where C_{MS} is concentration at the measurement point; C_{O_2} is concentration evolving off of the sample; and t' is an integration variable. To determine the RTD, prescribed inlet and outlet concentration tracer curves were substituted for C_{O_2} and C_{MS}, respectively, resulting in an expression for outlet vector concentration, given as:

$$\bar{\mathbf{C}}_{out} = \bar{\bar{\mathbf{C}}}_{in}\bar{\mathbf{E}}$$

(5.11)

where $\bar{\bar{\boldsymbol{C}}}_{in}$ is the Toeplitz or convolution matrix form of $(C_{in}\Delta t)$, and Δt is the uniform measurement timestep. A linear system of equations was solved to ensure stability for the discrete RTD via a combined least-squares and energy minimization method, given as:

$$\bar{\mathbf{E}} = \left(\bar{\bar{\mathbf{C}}}_{in}^T\bar{\bar{\mathbf{C}}}_{in} + \omega\bar{\bar{\mathbf{I}}}\right)^{-1}\bar{\bar{\mathbf{C}}}_{in}^T\bar{\mathbf{C}}_{out}$$

(5.12)

where ω is a weighting factor, selected as $5\cdot10^{-4}$. The solution was verified using a continuously-stirred tank reactors (CSTR) in series model, defined as [144]:

$$E(t) = \frac{t^{N-1}}{(N-1)!}\left(\frac{N}{\tau}\right)^N \exp\left(-\frac{t}{\tau}N\right)$$

(5.13)

where N is the integer number of tanks, defined via least-squares minimization, and τ is the space time or mean residence time of particles in the reactor, defined as:

$$\tau = \bar{t}_{\text{out}} - \bar{t}_{\text{in}}$$

(5.14)

where $\bar{t}$ is the concentration-weighted average time of the experimental tracer curves [144], represented as:

$$\bar{t} = \frac{\int_0^{C_{\text{step}}} t\, dC}{\int_0^{C_{\text{step}}} dC} \approx \frac{1}{C_{\text{step}}} \sum_{\text{k}} t_{\text{k}} \Delta C_{\text{k}}$$

(5.15)

where C_{step} is the steady-state tracer concentration. The RTD was then used to remove dispersion effects from MS/GC concentration curves, producing corrected O_2 evolution curves, given as:

$$\bar{\mathbf{C}}_{O_2} = \left(\bar{\bar{\mathbf{E}}}^{\mathrm{T}} \bar{\bar{\mathbf{E}}} + \omega \bar{\bar{\mathbf{I}}} \right)^{-1} \bar{\bar{\mathbf{E}}}^{\mathrm{T}} \bar{\mathbf{C}}_{\text{MS}}$$

(5.16)

An alternative form, without weighting and employing a transformation to Fourier space, was also used, given as:

$$\bar{\mathbf{C}}_{O_2} = F^{-1} \left[\frac{F\left(\bar{\mathbf{C}}_{\text{MS}} \right)}{F\left(\bar{\mathbf{E}} \right)} \right]$$

(5.17)

where F and F^{-1} represent the Fourier transform and its inverse, respectively, performed via fast-Fourier transform methods in MATLAB [145].

Fourteen tracer dispersion experiments were performed for flow inputs C_{in}, at a point close to the inlet of the mass spectrometer (A in Figure 5.2) and C_{out}, at the inlet of the UFR (B in Figure 5.2). An inlet flow of 1 L$_N$/min of Ar (where L$_N$ denotes liters at normal conditions; mass flow rates are calculated at 273 K and 1 bar) at a total pressure between 110 and 140 mbar was used, and O_2 step changes of 0.2 L$_N$/min were sequentially introduced and stopped with 60 s between steps to allow for the development of steady flow. The O_2 was temporally monitored at a MS sampling rate of 1 Hz for each O_2 step, and RTDs were determined from the averaged, normalized concentration curves.

The results for the average runs, comparing the inlet (solid, C_{in}^*) and outlet (dash-dotted, C_{out}^*) normalized O_2 concentrations, are shown in Figure 5.4a for cases where O_2 was added to the Ar stream and Figure 5.4b for where it was successively removed. The gray areas represent 95% confidence intervals, evaluated from the individual runs. The curves indicated an initial 2-5 s of lag, slightly longer for Figure 5.4b. As a result of dispersion, throughout the responses, the gap between C_{in}^* and C_{out}^* grew from the initial lag time to a difference roughly 5 s larger for both step-up and step-down.
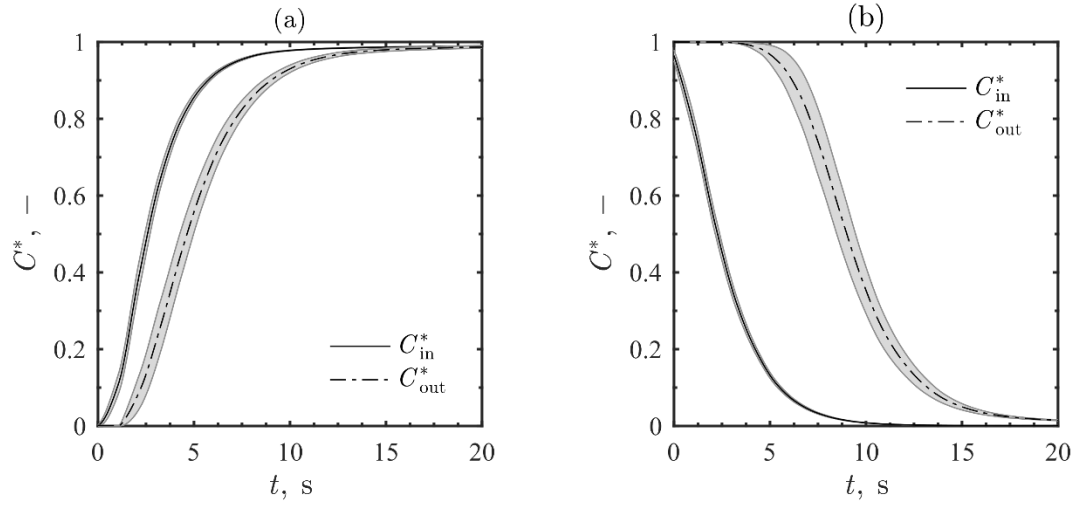
Figure 5.4 Average input (solid) and output (dash-dotted) dimensionless O_2 concentration curves for dispersion tracer step tests. Gray regions indicate 95% confidence intervals. Curves were measured for step changes (a) from 0 to 0.2 L_N/min and (b) from 0.2 to 0 L_N/min flow controller settings with 60 s between changes to reach steady flow.

To more robustly quantify lag and dispersion, the C_{in}^* and C_{out}^* shown in Figure 5.4a were numerically compared. The UFR RTDs calculated using deconvolution (solid, E_{DCNV}) and tanks-in series (dashed, E_{CSTR}) are shown in Figure 5.5. The two RTD methods produced average residence times of 2.15 and 2.14 s, respectively, with standard deviations of $6.06 \cdot 10^{-2}$ and $6.21 \cdot 10^{-2}$ s and minimal lag. While both methods indicated residence times no greater than 4 s for most of the O_2, E_{DCNV} had a tighter distribution during the first 4 s compared with E_{CSTR}. The resulting RTD from E_{CSTR} was more numerically stable compared with E_{DCNV} and was selected to correct GC-calibrated MS O_2 flow rate measurements via the Fourier-space deconvolution.
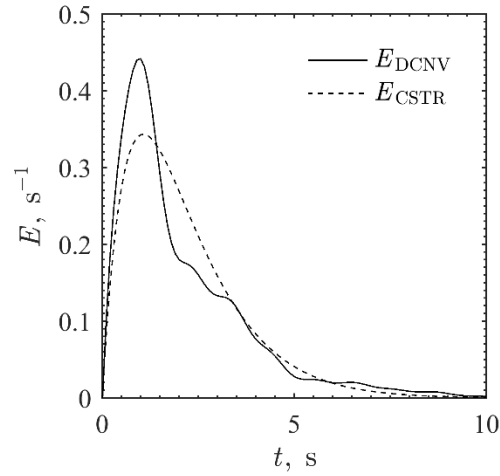
Figure 5.5 Residence time distribution of the reactor determined via the method of deconvolution (solid) and the continuously-stirred tank reactors in series model (dashed).

The minimal lag and dispersion found via tracer studies were consistent with the 3D streamlines from steady-state model results. Streamlines from the steady state model are shown in Figure 5.6 with a logarithmic gradient from orange to yellow based upon increasing velocity magnitude. The streamlines were overlaid on the model mesh, shown in gray, and exit at the outlet of the UFR. Steady-state velocity magnitudes ranged from approximately 0 to 7.6 m/s and the velocity decreased from the inlet pipes to the UFR due to large changes in areas. Computed streamlines indicated no major zones of stagnation or recirculation due to the upflow configuration and low vacuum operating conditions of the reactor, indicating minimal dispersion.
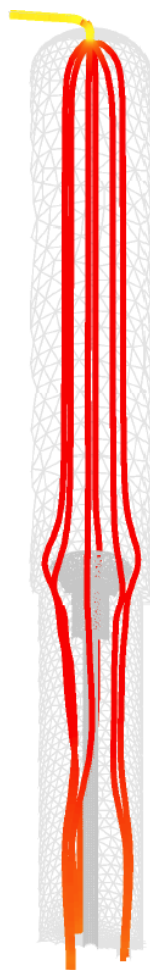
Figure 5.6 Three dimensional streamlines originating from the three reactor inlets, as predicted by steady-state heat and mass transfer modeling of the upward flow reactor. Fluid velocity is higher near the inlets and outlet, with a logarithmic color/value scale.

5.4   Experimental

An experiment was performed in the UFR to thermally reduce Co_3O_4 to CoO and O_2. A sample of ~0.2g of Co_3O_4 (Sigma-Aldrich, particle size <10 μm) with a bed thickness of roughly 2 mm was reduced in the HFSS with a single, center lamp set to an electrical input power of 4.23 kW_e. Sample bed temperatures, reactor pressure, and O_2 evolution were temporally monitored during the thermal reduction. Using an alternative feedthrough, a thermocouple was embedded directly in the sample to monitor temperatures for model comparisons. The experiment is summarized in Figure 5.7, which shows measurements of

lamp electrical input power (solid black, P_{HFSS}), thermocouple temperature (dash-dotted, T_{TC}), and plots of relative MS ion current measurements (I) for Ar (green) and O_2 (blue).

The reactor was evacuated to low-vacuum conditions and 1 L_N/min of Ar was then introduced, coinciding with the initial increase in Ar and brief spike then drop in O_2 as it was purged from the system. Steady flow resulted with an average operating inlet pressure of 125 mbar throughout the experiment and an initial O_2 partial pressure of ~0.5 mbar as measured by the GC. The HFSS lamp was switched on at roughly 100 s, as indicated by the P_{HFSS} step change from 0 to 4.23 kW_e. Thermocouple and MS measurements indicated rapid T_{TC} increase and O_2 evolution from the sample, respectively, within the following 60 s. T_{TC} remained below $T_{\Delta G=0} = 1025.5$ K during this time due to thermal resistance and capacitance in the porous sample and continued to increase afterward. Therefore, the sample was directly irradiated for 15 min to allow the sample to approach steady conditions and facilitate a comparison to modeled steady-state sample temperature.
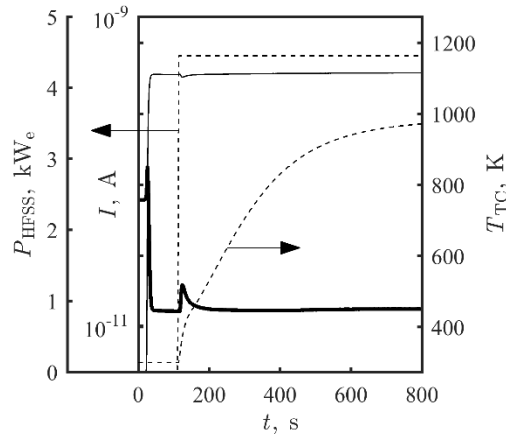
Figure 5.7 Experimental results of Co_3O_4 reduction performed in upward flow reactor for HFSS input power (dashed), thermocouple temperature, (dashed), and Ar (solid, light) and O_2 (solid, heavy) ion current.

The embedded thermocouple configuration prevented a post-experimental sample mass measurement due to unavoidable material loss during sample removal. Therefore, to verify complete reduction, a second sample of 0.3g Co_3O_4 was reduced under similar conditions using the standard feedthrough configuration with a thermocouple probe underneath the sample. The sample mass measured after experimentation was within 1% of the theoretical fully-reduced mass, assuming the sample was initially fully-oxidized.

5.5   Results and Discussion

The irradiation profile at the sample surface from the HFSS center lamp, as predicted by the MCRT, ranged from 287 to 1052 $kW \cdot m^{-2}$, with an area-weighted average of 512 $kW \cdot m^{-2}$. Smoothed MCRT results for the sample are shown in Figure 5.8. The MCRT predicted some skewing of the flux profile toward the back of the crucible (positive x-direction) due to the angle of the beam down mirror. Some local variations were also evident due to mirror slope errors and refraction through the complex-shaped quartz tube.
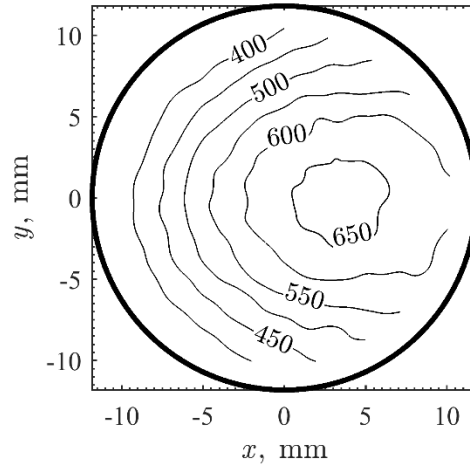
Figure 5.8 Modeled, smoothed sample surface heat fluxes for the center lamp of the high-flux solar simulator in kW·m^{-2}, produced from the Monte Carlo ray tracing model modified for beam down configuration.

For heat and mass transfer modeling, the default under-relaxation for pressure and momentum were modified to values of 0.2 and 0.5, respectively, in order to achieve convergence of the continuity and energy equations, which occurred within 621 iterations. Convergence was defined as a decrease to 10^{-3} for scaled residuals of continuity, momentum, and radiation and 10^{-6} for energy, although residuals continued to decrease below those limits. Average, maximum, and minimum temperatures in the sample bed were also monitored to ensure convergence. A mass imbalance of $< 0.01\%$ of the inlet flow was calculated for the flowfield.

Grid independence was demonstrated in the mesh by progressively refining it between model runs and comparing the results. The average sample temperature at each resolution was compared to demonstrate convergence with finer resolutions. Based on these results, a mesh of 257,807 cells and a sample cell depth of three cells was selected, as approximately doubling the number of cells and increasing the sample cell depth to four

81

only produced a <1 K difference. Discretization independence for radiation modeling was also studied, and a 7x7 mesh selected, as an increase to 9x9 only produced a <1 K difference while significantly increasing computation time.

The sample temperature contours for steady-state are given in Figure 5.9. The volumetric average sample temperature converged to a steady-state value $T_{pm} = 1260$ K. A significant average sample temperature drop $\Delta T_{pm} = 369$ K was found due to the low average $k_{eff} = 0.916$ W·m^{-1}·K^{-1}. A similar radial temperature drop along the sample surface was observed, however, the temperature gradient was found to be highly dependent upon sample alignment with respect to the HFSS focal point.
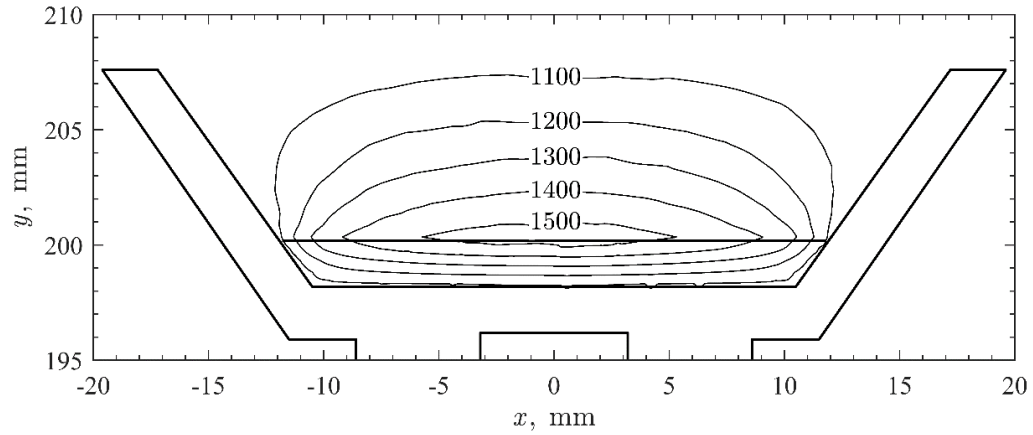
Figure 5.9 Modeled steady-state temperature contours for a cross-sectional detail view of the crucible, sample, and neighboring fluid field for temperatures between 1100 and 1500 K.

A three-level sensitivity study was used to determine the impact on modeled T_{pm} for deviations from the literature values for k_p and α_{pm} at wavelengths shorter than 3 μm, as this range most significantly affected the initial absorption of HFSS radiation. Ranges of 0.7 – 0.9 and 1 – 10 W·m^{-1}·K^{-1} were selected, respectively, for α_{pm} and k_p. The results

from the sensitivity study are given in Table 5.4 where Run 3 is the default case. Increases in k_p enhanced heat transfer, increasing temperatures at the bottom of the sample bed and decreasing ΔT_{pm}. Increasing the α_{pm} significantly enhanced the absorption of HFSS irradiation, increasing the temperatures throughout the bed, as seen by an increase in average T_{pm}.

Table 5.4 Sensitivity study results for average sample bed temperature, temperature drop, and total effective conductivity as functions of Co_3O_4 sample absorptivity and solid particle thermal conductivity.

Run	α_{pm}	k_p, W·m^{-1}·K^{-1}	Avg. T_{pm}, K		Avg. ΔT_{pm}, K		Avg. k_{eff}, W·m^{-1}·K^{-1}	
1	0.8	1	1281	(7.37%)	538	(45.7%)	0.373	(-59.3%)
2	0.7	10	1227	(-3.30%)	341	(-7.75%)	0.902	(-1.49%)
3	0.8	10	1260	-	369	-	0.916	-
4	0.9	10	1288	(2.91%)	398	(7.79%)	0.927	(1.21%)
5	0.8	100	1237	(-1.87%)	264	(-28.4%)	1.585	(73.1%)

The sensitivity analysis showed that the average k_{eff} was relatively insensitive to even a two orders of magnitude change in k_p due to the limiting nature of porous region heat transfer (runs 1, 3, 5). Similarly, the average T_{pm} only varied by 44 K. The average ΔT_{pm}, however, varied by 274 K across the selected values, showing that at least an order-of-magnitude determination of k_p is important for accurate modeling of sample heat transfer. The results were shown to be very dependent on the sample α_{pm} (runs 2-4), as varying α_{pm} by 0.1 produced variation in the average T_{pm} of similar magnitude as the large variation in k_p. Smaller variations in the average ΔT_{pm} were observed as a function of α_{pm}, with a difference of 57 K for a range of 0.2.

Figure 5.10 shows transient evolution of the average temperature at the sample top surface (dotted, $T_{pm, top}$,), bottom surface (dashed, $T_{pm, bottom}$), and throughout the volume of

sample (solid, T_{pm}), overlaid with the measured experimental thermocouple temperature (circles, T_{TC}) for the (a) entire experiment and (b) the first 60 s of the experiment. The sample surface rapidly heated due to the highly concentrated HFSS irradiation, while the sample bottom took several minutes to reach a temperature where the thermal reduction of Co_3O_4 was spontaneous. The thermocouple, embedded in the 2 mm deep sample bed, increased in temperature at a rate similar to the sample average prior to significant reduction. The measurement began to diverge as the sample reacted, but T_{TC} was bounded by the average top and bottom temperature for the duration of the experiment. The averages of T_{pm} and ΔT_{pm} converged to 1257 K and 370 K, respectively, in 1000 s, consistent with the steady-state model results. The thermocouple approached a steady-state temperature $T_{TC} = 1205 \pm 9$ K.
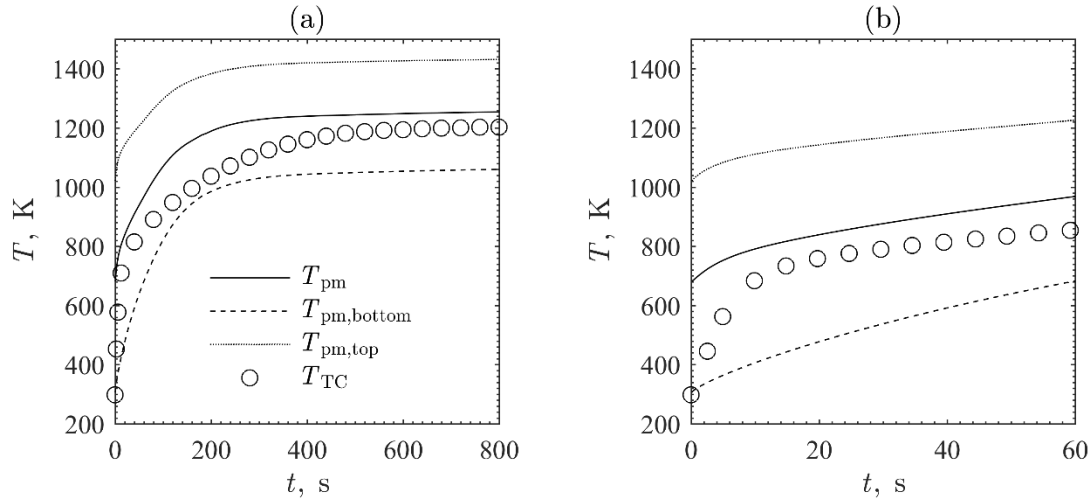
Figure 5.10 Modeled temporal temperature evolution averaged over the top surface (dotted), bottom surface (dashed), and bed (solid) compared with measured temporal temperatures (circles) for (a) the entire test and (b) the first 60 s of the test.

The modeled temporal temperature profiles and experimental temperatures followed the same general tends during the initial 60 s of heat-up (Figure 5.10b) and prior

to significant α in the bed. As the reaction progressed, the experimental temperature profile displayed a different curvature than the modeled results, taking longer to approach steady-state conditions. Contact resistance between the thermocouple and particle bed coupled to spectral dependencies of ε_{pm} and α_{pm} likely influenced this disparity. These effects were readily observable at higher temperatures where the impacts were consistent with the differences between measured and modeled temperatures in Figure 5.10a.

Temporal O_2 evolution via (a) MS/GC measurements and corresponding (b) Co_3O_4 conversion are given in Figure 5.11 for measured (solid) and dispersion corrected (dashed) results. The majority of the sample reacted within the first 60 s, and complete conversion was reached in less than 180 s. While dispersion and lag clearly had some impact in the initial 2-3 s of the experiment, the overall impact was relatively minute.
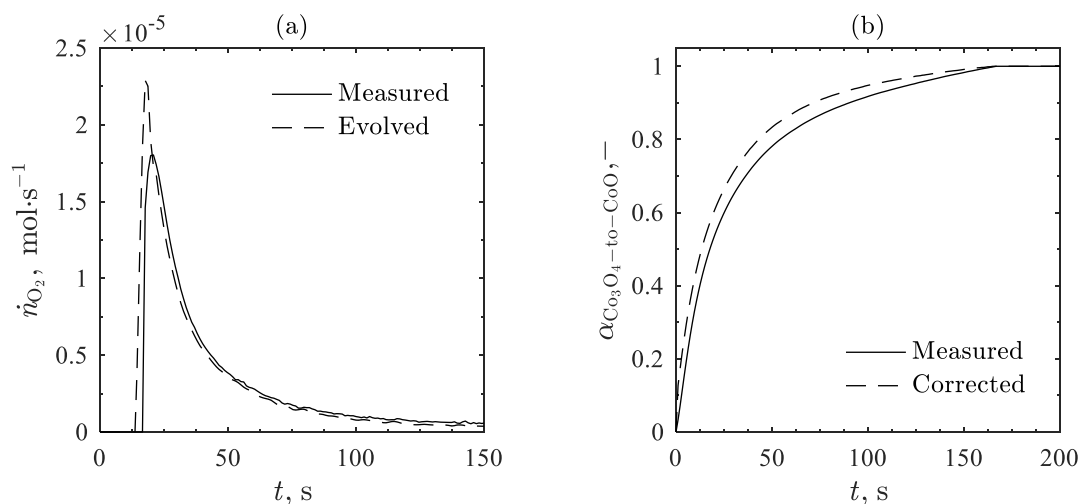
Figure 5.11 Thermal reduction of Co_3O_4 as measured by mass spectrometer and gas chromatographer (solid) and corrected for dispersion (dashed), presented as (a) O_2 molar flow rates and (b) Co_3O_4 to CoO conversion.

5.6   Conclusions

An upward flow reactor coupled to a high flux solar simulator was designed, fabricated, and characterized to accurately determine spatial and temporal temperature changes within a reacting sample and account for dispersion in the reactor under vacuum. Characterization included a combination of computational fluid dynamics and heat transfer modeling and experimental measurements in the sample bed and flowfield. Steady-state model results suggested rapid, efficient transport of product gases from the reactor with no evident eddies or recirculation downstream of the sample. Experimental tracer studies also revealed minimal lag and dispersion in the reactor. Both experimental and modeled transient temperatures indicated rapid initial heating rates in the sample, well in excess of 50 K/s, and the measured temporal temperature was bounded by the modeled average top and bottom transient surface temperatures for the duration of the experiment. Contact resistance between the bed and the thermocouple and spectral changes in absorptivity and

emissivity likely affected experimental measurements, causing differences between modeled and measured temperature profiles as the reaction progressed.

Model sensitivity analysis showed that large changes in sample solid thermal conductivity were mitigated by the bed porosity and did not drastically alter the average bed temperature; however, these parameters did have a large effect on temperature drop through the bed. Changes in sample absorptivity of ± 0.1 significantly increased the average bed temperature but had a minor effect on temperature drop. All levels of the analysis indicated significant radial and axial temperature gradients within the bed. These gradients, in conjunction with the impact of contact resistance, highlight the difficulty of measuring sample temperatures, even in thin sample beds, and support the use of experimentally calibrated, spatially-varying model temperature results. These results provide the foundation for studying reaction rates for redox-active materials used in two-step solar thermochemical cycles.

CHAPTER 6. Fe₂O₃/Fe₃O₄ CYCLES FOR ENERGY STORAGE

6.1   Introduction

Kinetic and thermodynamic analyses of the Fe₂O₃/Fe₃O₄ binary pair are presented in order to evaluate the oxides for thermochemical energy storage (TCES). Fe₂O₃ has a higher thermal reduction temperature than most other viable binary oxides, permitting higher theoretical Air Brayton cycle efficiencies in TCES/solar electricity cycles. The Fe₂O₃/Fe₃O₄ redox pair are also are relatively inexpensive and widely available compared to Co₃O₄/CoO materials, and they carry fewer environmental/human health concerns [41], making the redox pair a more practical and economically appealing candidate for large-scale deployment. The reversible redox reaction of Fe₂O₃/Fe₃O₄ is represented as:

$$3Fe_2O_3 \leftrightarrow 2Fe_3O_4 + \frac{1}{2}O_{2(g)} \;,\Delta H_{298.15\ K} = 78.3 \text{ kJ·mol}^{-1} \qquad (6.1)$$
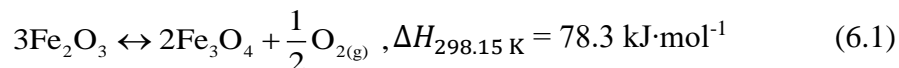
Based upon known thermodynamic properties and relative abundance, Fe₂O₃/Fe₃O₄ were identified for TCES applications via integration into an Air Brayton cycle. A thermodynamic analysis of the cycle was performed as a function of molar flow rate of air, reactor temperature, compressor outlet/turbine inlet pressure, and solar concentration ratio. The thermal reduction and oxidation reactions were examined using thermogravimetric analysis (TGA) for a range of heating rates and O₂ partial pressures to measure reaction rates, identify rate limiting mechanism(s), and determine kinetic parameters. A cycling study was performed to examine material stability and scanning electron microscopy (SEM) and room and high-temperature x-ray diffractometry (XRD) were performed to

study particle size, morphology, post-reaction chemical composition, and Fe_2O_3/Fe_3O_4 crystalline structure.

The Fe_2O_3 thermal reduction temperature was reduced by operating at decreased O_2 partial pressures to shift the equilibrium to a more favorable temperature range according to Le Chatelier's principle. The impact of decreasing the O_2 partial pressure is shown in Figure 6.1. For an O_2 partial pressure of 10^{-3} bar, Fe_2O_3 begins to reduce to Fe_3O_4 at a temperature of 1432 K. The Fe_2O_3/Fe_3O_4 pair allows for higher oxidation temperatures and, therefore, greater Air Brayton cycle theoretical efficiencies, at the cost of decreasing receiver absorption efficiencies due to greater re-radiative losses to the environment [40]. Therefore, a comprehensive thermodynamic cycle analysis was performed to assess the potential of the Fe_2O_3/Fe_3O_4 pair.
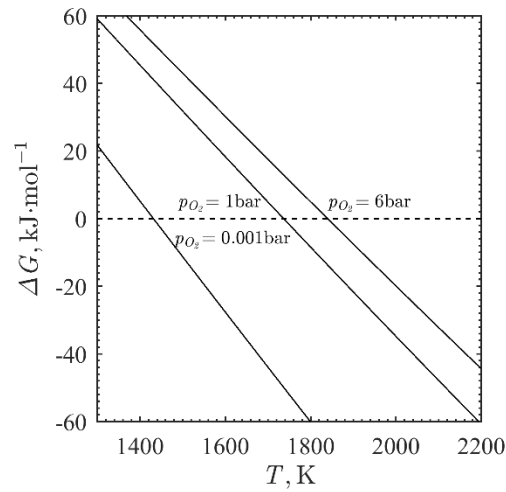
Figure 6.1 Change in Gibbs free energy for the reduction of Fe_2O_3 at O_2 partial pressures of 0.001, 1, and 6 bar.

6.2   Thermodynamic Analysis

A schematic from previous work [19], modified for Fe_2O_3/Fe_3O_4 redox reactions, is provided in Figure 6.2. The cycle employs a windowed, directly irradiated solar receiver/reactor at low vacuum ($p_{O_2} = 10^{-3}$ bar) to promote the thermal reduction of metal oxide particles at a temperature $T_{reactor}$. Reduced particles are then re-oxidized in a counter-flow configuration with a pressurized airflow at p_{comp} supplied by a compressor. The high-temperature, O_2-deficient air exits the re-oxidizer and expands through a turbine, while the re-oxidized particles are returned to the receiver/reactor to complete the cycle.
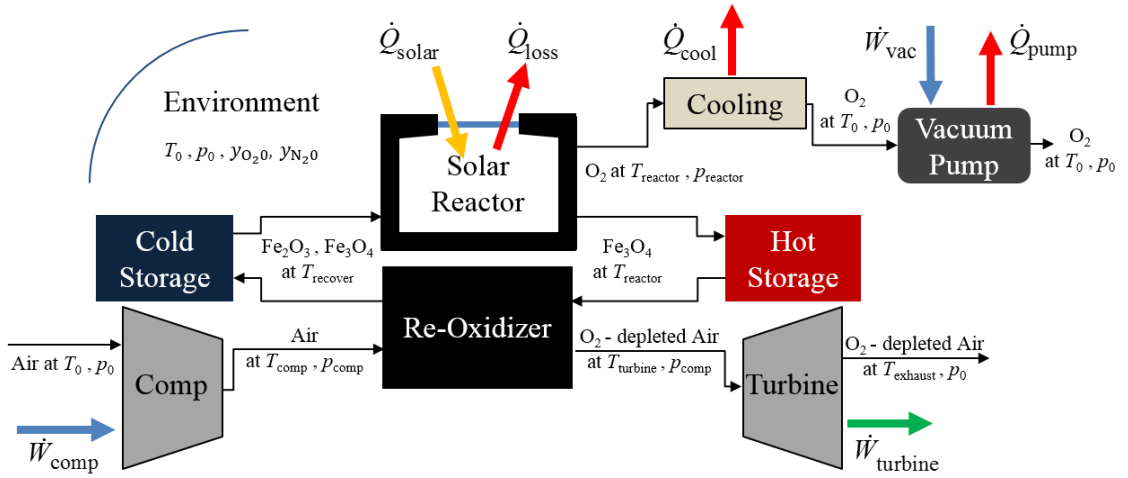
Figure 6.2 System schematic of the Air Brayton cycle with an integrated two-step thermochemical energy storage cycle based on Fe_2O_3/Fe_3O_4 redox reactions with relevant mass and energy flows.

A thermodynamic analysis of the system was performed independently of subcomponent design considerations and kinetic limitations to ascertain theoretical efficiency limits by imposing first and second thermodynamic law constraints. Ideal gas behavior, homogeneous gas/solid mixtures, and local thermal equilibrium between the gas and solid phases were assumed, and thermophysical properties were extracted from the NIST Chemistry Webbook [146]. The thermal reduction step was fixed at constant values

ranging from $T_{reactor} = T_{\Delta G = 0} = 1432$ K, corresponding to $\Delta G = 0$ for an oxygen partial pressure $p_{O_2} = 10^{-3}$ bar (*i.e.* conditions where the reaction becomes spontaneous) to $T_{reactor}$ = 1632 K, selected due to material limitations and rapidly increasing radiative losses. The solar thermochemical reactor was idealized as a windowed cavity comprised of two diffuse, isothermal surfaces, one opaque and one semi-transparent to shortwave radiation, and radiative exchange was modeled using a two-band gray approximation. Full conversion of Fe_2O_3 to Fe_3O_4 and O_2 at solar concentration ratios between $C = 1000$ and 5000 suns was assumed due to the thermodynamic favorability of the thermal reduction that resulted from the continuous removal of O_2 by the vacuum pump during the process. The analysis was normalized to 2/3 mol·s^{-1} of Fe_3O_4 exiting the solar thermochemical reactor.

The re-oxidizer was modeled in a counterflow configuration with the minimum particle outlet temperature $T_{recover}$ limited to the temperature of air exiting the compressor T_{comp}. Airflow into the compressor was controlled to ensure $T_{turbine}$, the temperature of O_2-deficient air exiting the re-oxidizer and entering the turbine, was not so high as to prevent re-oxidation. In order to define an upper bound on cycle performance independent of subcomponent designs, the compressor and turbine were idealized as operating isentropically, and the vacuum pump used to hold the reactor at a low vacuum pressure $p_{reactor}$ as isothermal and reversible at the environment temperature $T_0 = 298.15$ K. The work, heat, and pressure losses from material transport/storage were neglected as in previous analyses [19]. Rough estimates of these nonidealities for similar thermodynamic cycles have been made elsewhere [147], as have estimates for the work requirements of real vacuum pumps and/or air separation methods, both of which are expected be significantly higher than ideal performance calculations [61].

The $T_{recover}$ and $T_{turbine}$ resulting from the re-oxidizer chemical equilibrium and energy balances for fixed $T_{reactor} = 1432$ K and $p_{comp} = 30$ bar are shown in Figure 6.3. For the entire range of $\dot{n}_{air}$ shown, the entering Fe_3O_4 particle flow was fully re-oxidized to Fe_2O_3. $T_{turbine}$ gradually increased until $\dot{n}_{air} = 5.1$ mol·s^{-1}, for which the sensible heat extracted from the solid particle flow was maximized due to $T_{recover}$ reaching the minimum thermodynamically allowable value of $T_{recover} = T_{comp}$. For $\dot{n}_{air} > 5.1$ mol·s^{-1}, $T_{turbine}$ therefore rapidly decreased.
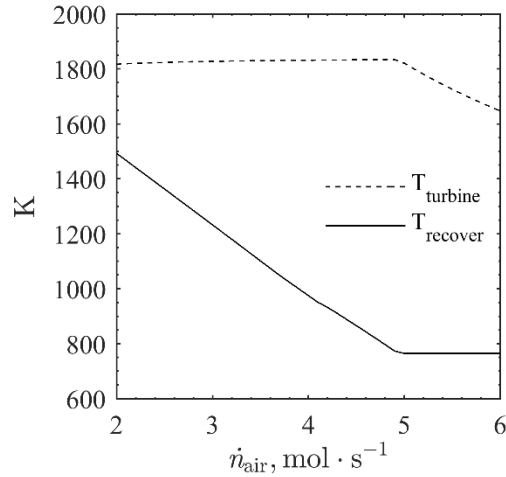
Figure 6.3 Fe_2O_3/Fe_3O_4 particle temperature exiting the re-oxidizer (solid) and O_2-depleted air temperature entering the turbine (dashed), as a function of molar air flow rate and for a solar thermochemical reactor temperature of 1432 K, solar concentration ratio of 1000 suns, and re-oxidizer pressure of 30 bar.

Figure 6.4 shows the resulting subcomponent heat transfer rate $\dot{Q}$ and power $\dot{W}$ values for the same $T_{reactor}$ and p_{comp} as Figure 6.3 and $C = 1000$ suns. The heat rejection via O_2 exiting the reactor $\dot{Q}_{cool}$ remained constant, as complete re-oxidation occurred for all $\dot{n}_{air}$ shown. Consistent with the abrupt $T_{recover}$ minimum in Figure 6.3, the required input reactor heat transfer rate $\dot{Q}_{solar}$ reached a maximum for $\dot{n}_{air} = 5.1$ mol·s^{-1}, as the particles

were fully re-oxidized at the minimum allowable temperature, providing no more chemical

or sensible energy storage potential for higher $\dot{n}_{air}$. The turbine power $\dot{W}_{turbine}$ grew more

slowly for $\dot{n}_{air} > 5.1$ mol·s^{-1} but did not become zero, as the increasing $\dot{n}_{air}$ continued to

increase the power output.
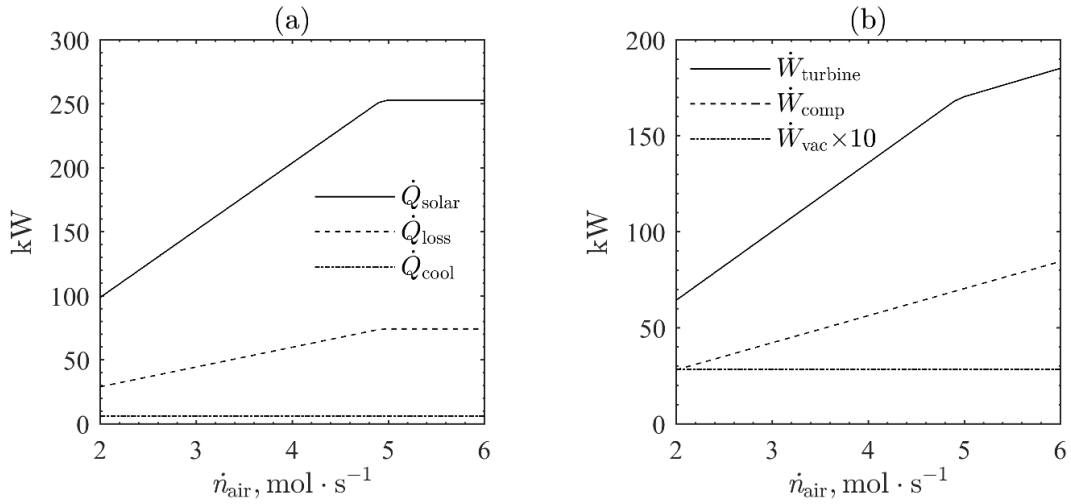
Figure 6.4 Energy balance components for the integrated thermochemical cycle, including (a) for the solar thermochemical reactor, heat transfer rates associated with concentrated solar irradiation (solid), thermal losses (dashed), and rejected high-temperature O₂ from thermal reduction (dashed-dot); and (b) power associated with turbine output (solid), compressor input (dashed), and vacuum pump input (dashed-dot) as functions of the molar air flow rate and for a solar thermochemical reactor temperature of 1432 K, solar concentration ratio of 1000 suns, and a re-oxidizer pressure of 30 bar.

The maximum theoretical thermodynamic cycle efficiency for the Air Brayton-

integrated thermochemical cycle was defined as:

$$\eta_{cycle} = \frac{\dot{W}_{turbine} - \dot{W}_{comp} - \dot{W}_{vac}}{\dot{Q}_{solar}}$$

(6.2)

At $C = 1000$ suns, $T_{reactor} = 1432$ K, $p_{comp} = 30$ bar, and $\dot{n}_{air} = 5.1$ mol·s^{-1}, a $\eta_{cycle} =$

38.4% was determined, which is significantly lower than the $\eta_{cycle} = 43.4\%$ from the

Co_3O_4/CoO analysis under equivalent conditions [19]. The lower η_{cycle} was primarily due to significantly higher $T_{reactor}$ and, therefore, higher $\dot{Q}_{loss}$ for the Fe_2O_3/Fe_3O_4 pair. However, because $\dot{Q}_{loss}$ is mitigated by increasing C [40, 59], an analysis of both redox pairs was performed to determine how η_{cycle} varies with C for $T_{reactor} = T_{\Delta G=0}$ and $\dot{n}_{air}$ fixed to achieve full re-oxidation and maximum sensible energy recovery in the re-oxidizer. Relevant model property value inputs for the analysis are shown in Table 6.1.

Table 6.1 Model property values for the analysis of cycle efficiency vs. solar concentration ratio for the Air Brayton cycle with paired thermochemical energy storage using Fe_2O_3/Fe_3O_4 and Co_3O_4/CoO reduction-oxidation pairs.

Property	Fe_2O_3/Fe_3O_4	Co_3O_4/CoO
$T_{reactor}$	1037 K	1432 K
$\dot{n}_{air}$	5.1 mol·s^{-1}	13.6 mol·s^{-1}
p_{comp}	30 bar	30 bar
p_{O_2}	0.001 bar	0.001 bar

The η_{cycle} for Fe_2O_3/Fe_3O_4 increased more rapidly with C than for Co_3O_4/CoO due to a higher $T_{reactor}$, as shown in Figure 5, and the η_{cycle} for the Fe_2O_3/Fe_3O_4 TCES cycle exceeded the Co_3O_4/CoO cycle at $C \geq 4352$ suns.
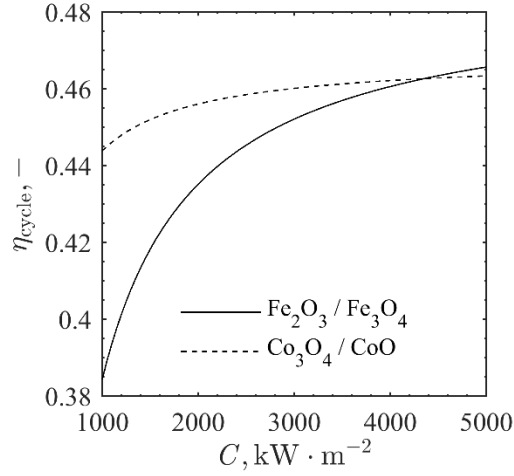
Figure 6.5 Theoretical cycle efficiencies for Fe_2O_3/Fe_3O_4 (solid) and Co_3O_4/CoO (dashed) thermochemical cycles as a function of solar concentration ratio at receiver temperatures of 1432 and 1037 K and compressor airflow rates of 5.1 and 13.6 mol·s^{-1}, respectively, and a re-oxidizer pressure of 30 bar.

Figure 6.6 shows $\dot{n}_{air}$ for a range of p_{comp} and $T_{reactor}$. A $\eta_{cycle} = 46.0\%$ was achieved for $C = 4000$ suns, $T_{reactor} = 1432$ K, $p_{comp} = 30$ bar, and $\dot{n}_{air} = 5.1$ mol·s^{-1}, and the η_{cycle} increased with diminishing returns for greater $\dot{n}_{air}$ and C. Increasing p_{comp} increased η_{cycle} as the O_2-deficient airflow entering the turbine expanded across a greater temperature difference, while increasing $T_{reactor}$ decreased η_{cycle} due to rapid increases in $\dot{Q}_{loss}$ from reradiation.

95
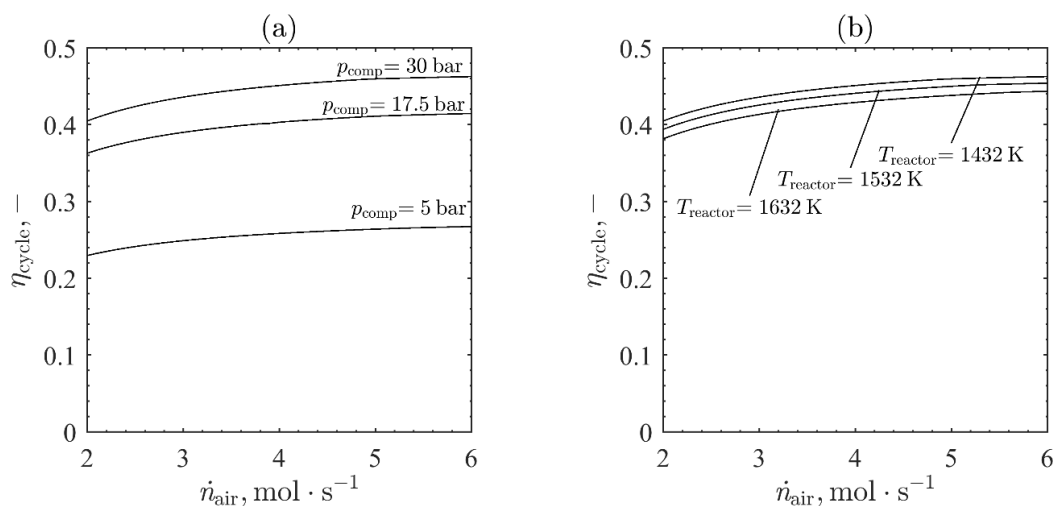
Figure 6.6 Theoretical cycle efficiency as a function of molar air flow rate entering the re-oxidizer for (a) compressor pressures of 5, 17.5, and 30 bar and a solar thermochemical reactor temperature of 1432 K; and (b) solar thermochemical reactor temperatures of 1432, 1532, and 1632 K and a compressor pressure of 30 bar.

6.3   Kinetic Analyses

The thermal reduction of Fe_2O_3 to Fe_3O_4 and O_2 and re-oxidation of Fe_3O_4 to Fe_2O_3 were examined in a thermogravimetric analyzer (TGA, Netzsch STA 449 F3 Jupiter, ± 1μg). Separate unreacted, high-purity Fe_2O_3 and Fe_3O_4 samples were selected for the two reaction steps to ensure that samples were not initially in partially reduced or oxidized states, respectively. Powder samples were placed on an Al_2O_3 crucible shielded with a platinum foil (Sigma-Aldrich 0.025MM Thick 99% Pt Foil 267244-1.4G). Sample temperatures were measured by an S-type thermocouple. Sample masses were measured before and after testing with an analytical balance (Mettler-Toledo ML54, ± 0.1mg) to verify the total mass change measured by TGA. Blank runs under identical conditions were performed following each experiment to correct for the influences of buoyancy and gas dynamics.

The temporal conversion from Fe_2O_3 to Fe_3O_4 and vice versa were calculated as:

$$\alpha(t) = \frac{m(t) - m_0}{m_\infty - m_0} \tag{6.3}$$

where $m(t)$ is the mass at time t; m_0 is the initial sample mass, between 90 to 100 mg; and m_∞ is the stoichiometric equilibrium mass for the fully-reacted sample. The reaction rate was defined as:

$$r = \frac{d\alpha}{dt} = h(p_{O_2}) k(T) f(\alpha) \tag{6.4}$$

where the temporal conversion rate $d\alpha/dt$ was calculated with a fourth-order finite difference approximation; and a reaction rate constant $k(T)$, partial pressure dependence $h(p_{O_2})$, and conversion-dependent kinetic model $f(\alpha)$ were fitted to r using a Nelder-Mead nonlinear minimization algorithm with a standard squared error objective function, given as:

$$SSE = \sum_i \left[r_i - \hat{r}_i(t, T, \alpha, p_{O_2}; p_1, p_2, \ldots, p_j) \right]^2 \tag{6.5}$$

where a least squares criterion was used to determine $\hat{r}$, the modeled reaction rate; t, T, α, and p_{O_2} were known for the datapoints i; and the unknown parameters $p_1 \ldots p_j$ were simultaneously fitted. An Arrhenius-type temperature dependency was assumed, given as:

$$k(T) = k_0 \exp\left(-\frac{E_a}{RT}\right) \tag{6.6}$$

where k_0 is the apparent pre-exponential factor; E_a is the apparent activation energy; and R is the universal gas constant. A Monte Carlo error analysis using 500 iterations was performed to determine 95% confidence intervals for the parameters $p_1 \dots p_j$ using the 2.5th and 97.5th percentile values of each fitted parameter [148].

The rate limiting mechanism of the Fe_2O_3 thermal reduction was described with a variable-order Avrami-Erofe'ev nucleation-controlled model (AN), given as:

$$f(\alpha) = n(1-\alpha)\left[-\ln(1-\alpha)\right]^{\frac{n-1}{n}}$$

(6.7)

where n is the reaction order. k_0, E_a, and n were simultaneously fitted at multiple heating rates to verify that the reaction was not heat transfer limited [149]. The three fitted values were then fixed and $h(p_{O_2})$ was described using a power-law relationship, given as:

$$h(p_{O_2}) = \left[1 - \frac{p_{O_2}}{p_{O_2,eq}(T)}\right]^m$$

(6.8)

where $p_{O_2,eq}$ is the equilibrium partial pressure for T and m is the constant reaction order for the p_{O_2} dependence, which was simultaneously fitted to experimental runs performed at multiple p_{O_2}.

All non-isothermal reduction experiments were performed with a constant total gas flow of 100 $mL_N \cdot min^{-1}$ (where L_N refers to liters at standard conditions, *i.e.* 273 K and 1 bar). Fe_2O_3 samples (Sigma-Aldrich ≥99.995 trace metals basis, particle size <5 μm) were heated to 1723 K in Ar at heating rates of 10–20 $K \cdot min^{-1}$ in the TGA high temperature

graphite furnace. The thermal reduction proceeded at elevated temperatures, and samples agglomerated and turned dark gray, similar to unreacted Fe_3O_4.

The relationship between α and T was found to be independent of β, indicating no heating rate (heat transfer) limitations. The reaction rate consistently slowed significantly for values $\alpha > 0.90$, and an isoconversional analysis [150] revealed large changes in E_a for such values. Thus, the analysis was limited to $0 < \alpha < 0.90$, and $k_0 = 2.768 \pm 0.783 \cdot 10^{14}$ s^{-1}, $E_a = 487.0 \pm 3.6$ kJ·mol^{-1}, and $n = 1.264 \pm 0.010$ were simultaneously fitted with 95% confidence intervals from the Monte Carlo analysis.

Two methodologies were employed to validate the model-fitted parameters. To evaluate the nucleation model, reaction order, and the appropriateness of the Arrhenius form of k, an Arrhenius plot was produced by calculating k as:

$$k\left(T_i\right) = \frac{r_i}{f\left(\alpha_i, \hat{n}\right)}$$

(6.9)

where r_i, α_i, and T_i are the same experimental data used to compute the nonlinear fit for k_0, E_a and n. Figure 6.8 contains the Arrhenius plot with calculated (markers) k's and modeled (line) values as a function of temperature, where the modeled k curve was determined from the fitted k_0 and E_a above. The calculated k's showed a clear Arrhenius temperature relationship for the fitted reaction order. The calculated data were matched by the modeled curve for most temperatures, although the curve somewhat underpredicted k at low temperatures and β's (*i.e.*, where the fixed measurement resolution and steeper r_i during early conversion would increase numerical errors).
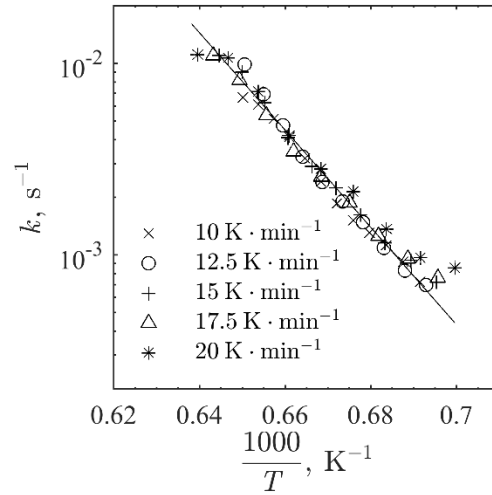
Figure 6.7 An Arrhenius plot of the reaction rate constant for the non-isothermal thermal reduction of Fe_2O_3 at 10-20 K·min^{-1}, calculated from: 1) the reaction model, fitted reaction order, and measured reaction rates (markers), and 2) the fitted pre-exponential factor and activation energy (line).

E_a was also calculated independently of the conversion model from the same experiments using an Avrami plot and the Kissinger method [151], given as:

$$\ln\left|\frac{\beta}{T_m^2}\right| = -\frac{E_a}{R}\left(\frac{1}{T_m}\right) + A$$

(6.10)

where T_m is the temperature at which r was maximized in each experiment, A is an undetermined constant, and E_a was determined from linear regression. Figure 6.8 is an Avrami plot and accompanying linear regression applied with the Kissinger method to determine $E_a = 574$ kJ·mol^{-1}.
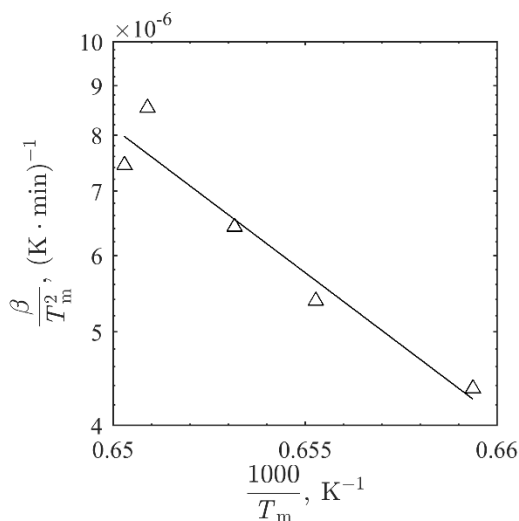
Figure 6.8 An Avrami plot and regression line for the non-isothermal thermal reduction of Fe_2O_3 at 10-20 K·min⁻¹, where the five markers correspond to the temperature of maximum conversion rate during an experiment at 10, 12.5, 15, 17.5 and 20 K·min⁻¹, respectively.

Previous analyses of the reduction of Fe_2O_3 in CO, H_2, or reducing H_2O–H_2 environments used both AN nucleation and zero-order phase boundary reaction mechanisms, and found that reduction occurred at lower temperatures and with a lower range of E_a = 33.28-139.2 kJ·mol⁻¹ [152, 153]. While varying factors such as sample purity, specific surface area, and particle size affect activation energy, the much higher fitted E_a = 487.0 kJ·mol⁻¹ for an inert environment was consistent with the higher reduction temperatures and suggested a gas composition dependence.

Further non-isothermal thermal reduction experiments were performed for 2–5% O_2–Ar to evaluate the impact of p_{O_2} with the determined kinetic parameters, and m = 8.317 $\pm$ 0.233 was determined via non-linear regression. The modeled and measured α's are given as a function of temperature in Figure 6.9. The temperature of the onset of reduction rose for increasing p_{O_2} due to thermodynamic limitations as descibed by Le Chatelier's

Principle, while the temperature range for the reaction was significantly reduced due to an increased k at higher temperatures. The model accurately captured changes in α as a function of p_{O_2} for $p_{O_2} < 0.05$ bar, a range which could reasonably be attained with a windowed receiver, vacuum pump and/or inert gas flow.
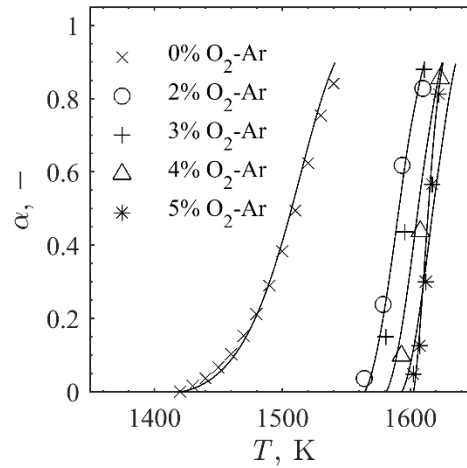
Figure 6.9 Measured (markers) and predicted (lines) conversions of Fe_2O_3 to Fe_3O_4 as functions of temperature and O_2 concentration between 0 and 5% O_2–Ar.

Fe$_3$O$_4$ oxidation to Fe_2O_3 has been described by a series of structure-dependent intermediate reactions detailed in previous work [154-157]. Fe_3O_4 has a cubic $[Fe^{2+}][Fe^{3+}]_2O$ inverse spinel structure with O^{2-} anions ordered in a close-packed face-centered cubic (FCC) lattice and Fe cations that occupy interstitial locations within the lattice: Fe^{2+} cations at tetrahedral sites Fe_{tet} and Fe^{3+} cations evenly divided between octahedral Fe_{oct} and tetrahedral sites [158]. The remaining interstitial sites exist as cation vacancies, at a 1:1 vacancy to cation ratio for octahedral sites and 7:1 ratio for tetrahedral.

As shown in Figure 6.10a, oxidation initially proceeds via Fe_{oct} ion diffusion through the particle to bond with adsorbed O^{2-}, accompanied by $Fe^{2+} \rightarrow Fe^{3+}$ oxidation,

which results in the formation of cation vacancies V_{Fe} [159, 160]. The process is represented as:

$$Fe_3O_4 + \left[\frac{2x}{3-x}\right]O_{2(g)} \rightarrow \left[\frac{3}{3-x}\right]Fe_{3-x}O_4$$

(6.11)
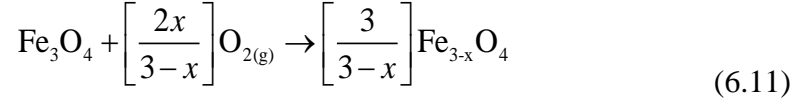
where x is the deviation from stoichiometry. As shown in Figure 6.10b, in sufficiently small particles of diameter $d_p < D = 300$ nm [155], and under thermodynamically favorable conditions, the reaction proceeds until $x_m = 1/3$ and the Fe^{3+}:O^{2-} ratio is 2:3, while the anion lattice structure remains unchanged, resulting in cubic γ-Fe_2O_3, or maghemite. Elevated temperatures induce nucleation of rhombohedral α-Fe_2O_3, or hematite, in which the O^{2-} anion lattice transitions to a hexagonal close packed (HCP) structure and the Fe^{3+} cations occupy octahedral interstitial positions.

As shown in Figure 6.10c, when $d_p > D$, a phase change occurs at $x_m < 1/3$ with sufficiently high temperatures and cation vacancy gradients to induce lattice strain, resulting in a disproportionated solid solution of α-Fe_2O_3 and stoichiometric Fe_3O_4, represented as:

$$Fe_{3-x_m}O_4 \rightarrow [4x_m]Fe_2O_3 + [1-3x_m]Fe_3O_4$$

(6.12)
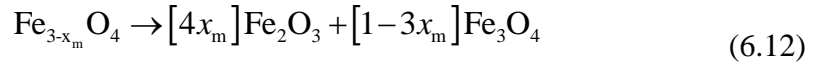
where x_m may vary with β and temperature due to their influence on cation vacancy gradients and lattice strain. As shown in Figure 6.10d, further oxidation of the remaining Fe_3O_4 occurs after disproportionation rather than via the nonstoichiometric reaction. Oxidation then proceeds via direct conversion to α-Fe_2O_3 facilitated by α-Fe_2O_3 nucleation sites, represented as:

$$\text{Fe}_2\text{O}_3 + \left[\frac{1-3x_m}{4x_m}\right]\text{Fe}_3\text{O}_4 + \left[\frac{1-3x_m}{16x_m}\right]\text{O}_{2(g)} \rightarrow \left[\frac{3-x_m}{8x_m}\right]\text{Fe}_2\text{O}_3$$

(6.13)
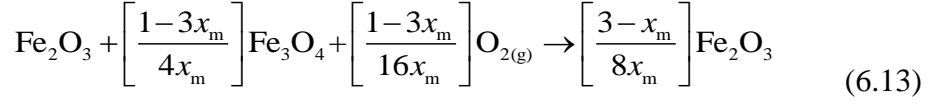
Together, Equations 6.11 – 6.13 are the back reaction of Equation 6.1.
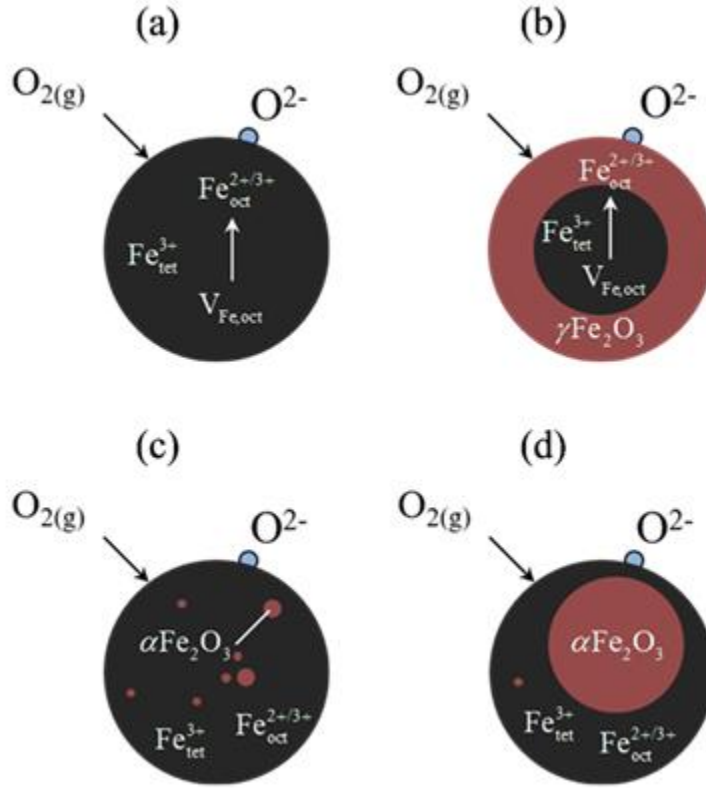
Figure 6.10 Schematic of Fe_3O_4 oxidation pathways (a) at the onset of the diffusion-limited regime, resulting in (b) oxidation to maghemite, or γ-Fe_2O_3; and (c) at the transition to the nucleation-limited regime, resulting in (d) oxidation to hematite, or α-Fe_2O_3.

The oxidation of Fe_3O_4 to Fe_2O_3 was examined via TGA with a constant total gas flow of 100 $\text{mL}_N \cdot \text{min}^{-1}$. Fe_3O_4 particle samples (Alfa Aesar Puratronic® 99.997% metals basis) were sieved with a size #170 (88 μm) mesh before each experiment. Samples were heated to 1623 K in 80% O_2-Ar in the TGA high temperature graphite furnace at 10–20 $\text{K} \cdot \text{min}^{-1}$, where different β's were used to ensure the reaction was not heat transfer limited. Additional non-isothermal experiments were performed for 20%–80% O_2-Ar to examine

p_{O_2} dependence, as shown in Figure 6.11. As no such dependence was observed, it was assumed that the reaction was not limited by surface O_2 adsorption for $p_{O_2} > 0.2$ bar, including conditions expected in the re-oxidizer. For each experiment, two local maxima in $d\alpha/dt$ were observed at (1) $T \approx 525$ K and (2) $T \approx 650$K, as shown for a single $d\alpha/dt$ curve in Figure 6.11. This translated to an inflection point at $\alpha \approx 0.74$, indicated by a vertical dashed line. The isoconversional method [150] revealed significant changes in E_a near the same α. As the proposed oxidation pathway contains multiple reaction steps with different mechanisms, it is likely that the second $d\alpha/dt$ maximum and observed E_a changes resulted due to an apparent two-step oxidation process.
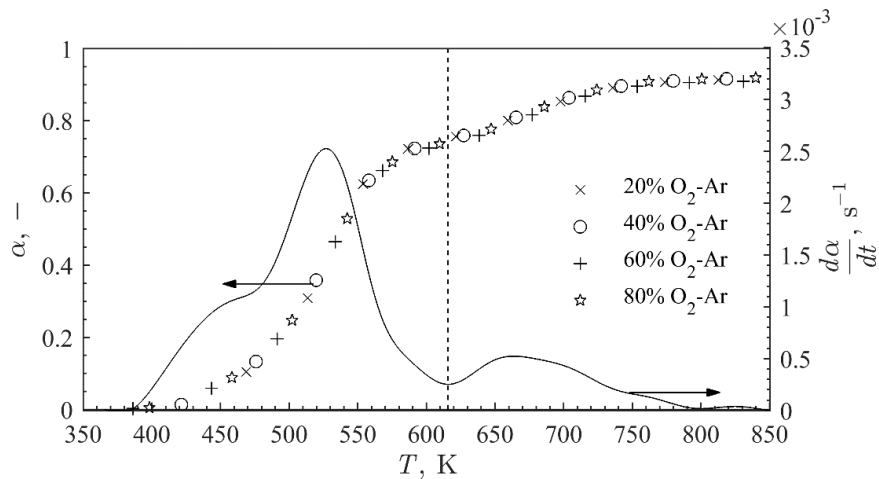
Figure 6.11 Experimental conversion (markers) and temporal conversion rate (solid line) for non-isothermal Fe_3O_4 oxidation at O_2 concentrations between 20% and 80%.

Because oxidation reached high α's at $T < 620$ K, a suite of isothermal experiments was performed to study oxidation at higher T, closer to conditions expected in the re-oxidizer. Samples were heated in 100% Ar at $\beta = 20$ K·min^{-1} to between $T = 673$ and 973 K, followed by a 20 min isothermal step to allow the sample to equilibrate. The flow was then switched to 80% O_2-Ar, after which the oxidation reaction proceeded rapidly (within $t < 20$ s) but did not achieve complete conversion, as shown in Figure 6.12a-b. Compared

to the non-isothermal experiments, the first peak in $d\alpha/dt$ occurred at lower $\alpha \lesssim 0.12$, resulting in an abrupt change in the slope of the $\alpha's$ in Figure 6.12a. For $\alpha > 0.12$, r was mostly invariant between experiments. The total oxidation time differed almost solely due to varying r for $\alpha \lesssim 0.12$, as shown in Figure 6.12b. As $D < d_p < 88$ μm for the Fe_3O_4 particles, the earlier α transition in isothermal experiments may have resulted from an effective minimization of x_m, and therefore earlier onset of α-Fe_2O_3 nucleation, by initiating oxidation at higher temperatures.
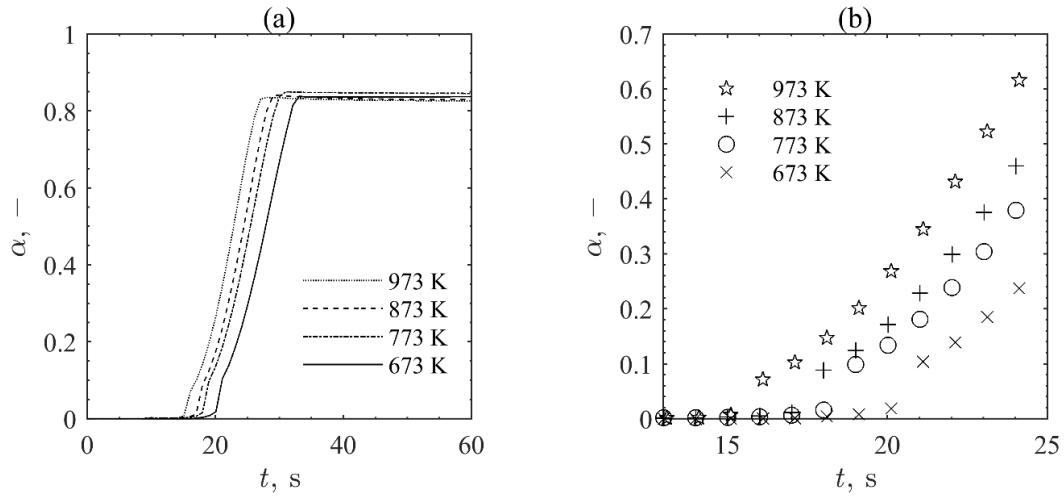
Figure 6.12 Experimental conversion for isothermal Fe_3O_4 oxidation at an O_2 concentration of 80% and temperatures between 673 and 973 K: (a) the full oxidation profiles and (b) detail-views of the first 25 seconds of oxidation.

Two step models have been previously used to capture Fe_3O_4 oxidation. A study of Fe_3O_4 pellet oxidation in air found two oxidation regimes: 1) for $T \lesssim 693$ K, a surface-controlled regime with $E_a \approx 155$ kJ·mol^{-1}, and 2) for $T \gtrsim 693$ K, a diffusion-controlled regime with 10.5 kJ·mol^{-1} [161]. In more recent work, Fe_3O_4 pellet oxidation in air for 1023 to 1173 K was described by 1) nucleation, with $E_a = 4.21 \pm 0.45$ kJ·mol^{-1}, then 2) diffusion, with $E_a = 53.58 \pm 3.56$ kJ·mol^{-1} [162]. Both studies used pellets of $d_p \gg 88$ μm, which

presumably accounted for a diffusion-limited regime following nucleation. However, in this study, isothermal thermogravimetry was strongly impacted by both rapid, complex reaction behavior at low α and uncertainty due to transients related to gas switching. As a result, both the non-isothermal and isothermal methods were inadequate for modeling Fe_3O_4 oxidation and determining rate-limiting mechanism(s), and this was left for future work.

6.4   Reduction-Oxidation Cycling

Fe_2O_3 samples were cycled between reduced and oxidized states via an isothermal p_{O_2} swing to evaluate their suitability for use in TCES cycles. Samples were heated to and held at 1623 K under an oxidizing environment, then cycled between 0% and 20% O_2–Ar in 15 min intervals at a flow rate of 100 $mL_N{\cdot}min^{-1}$. $T = 1623$ K was selected to allow for the thermodynamic favorability of both cycle steps for the given change in p_{O_2}, and to achieve rapid reaction kinetics. The relative temporal mass change $\Delta m/m_0$ is shown in Figure 6.13, and a dotted line indicates the theoretical $\Delta m/m_0$ for full conversion. Including an initial bakeout (cycle 0), the sample underwent 10 redox cycles and a cooldown in an oxidizing environment, shown in gray. The sample did not fully re-oxidize during the bakeout cycle nor in any cycle after, consistent with thermodynamic equilibrium calculations ($\Delta G = 0$) which forecast a Fe_3O_4—Fe_2O_3 mixture for $p_{O_2} = 0.2$ bar and $T > 1100$ K. While there was some variation in the oxidation extents per cycle due to slowed reaction rates as the sample neared thermodynamic equilibrium, there was no apparent systematic change in redox capacity during cycles 1-9.
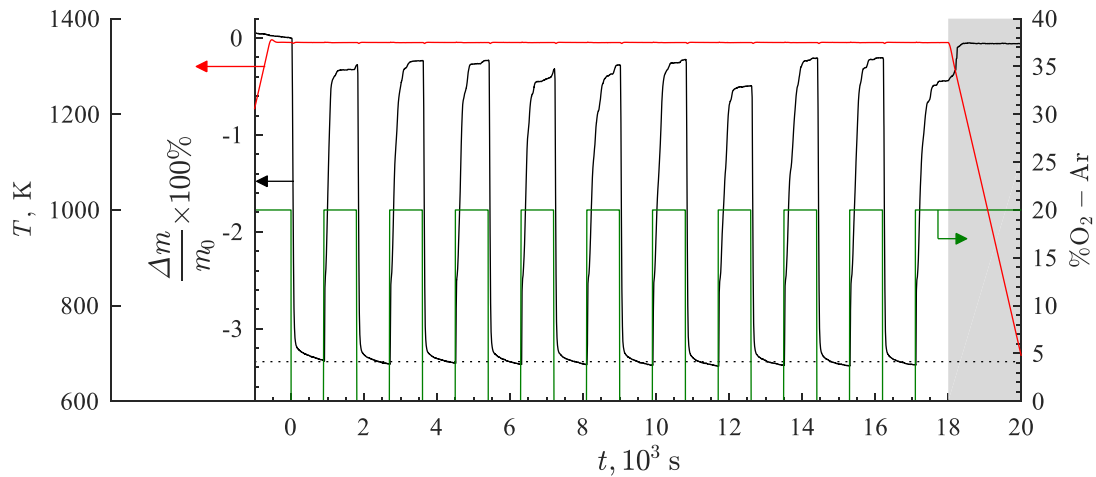
Figure 6.13 Sample temperature (red) and mass change relative to initial mass (solid black) for redox cycling of Fe_2O_3 compared to the theoretical value (dotted black), driven by isothermal O_2 partial pressure swings (green), where the gray region denotes cooldown in an oxidizing environment.

Figure 6.14 depicts (a) the relative temporal sample mass changes for cycles 0, 1, 5, and 9 superimposed for comparison and parity plots showing α from cycles 3, 5, 7, and 9 as a function of α from cycle 1 for (b) thermal reduction and (c) oxidation, respectively. Both Fe_2O_3 thermal reduction and initial Fe_3O_4 oxidation proceeded rapidly, consistent with the kinetic analyses. During the thermal reduction stage, full conversion was achieved, supporting the assumption of complete thermal reduction in the solar reactor for the thermodynamic analysis. For the re-oxidation stage, the final conversion varied significantly from cycle to cycle, with a maximum near $\alpha = 0.8$. However, the sample did approach $\alpha = 1$ during the oxidizing cooldown, as shown in the gray region ($t > 18000$ s) of Figure 6.13, as the full oxidation of Fe_3O_4 to Fe_2O_3 became thermodynamically favorable at lower temperatures. According to Figure 6.14c, the oxidation rates did not slow with cycle number, and in fact the oxidation of cycles 2-9 was consistently more rapid than cycle 1, as the majority of α_n values were above the identity line.
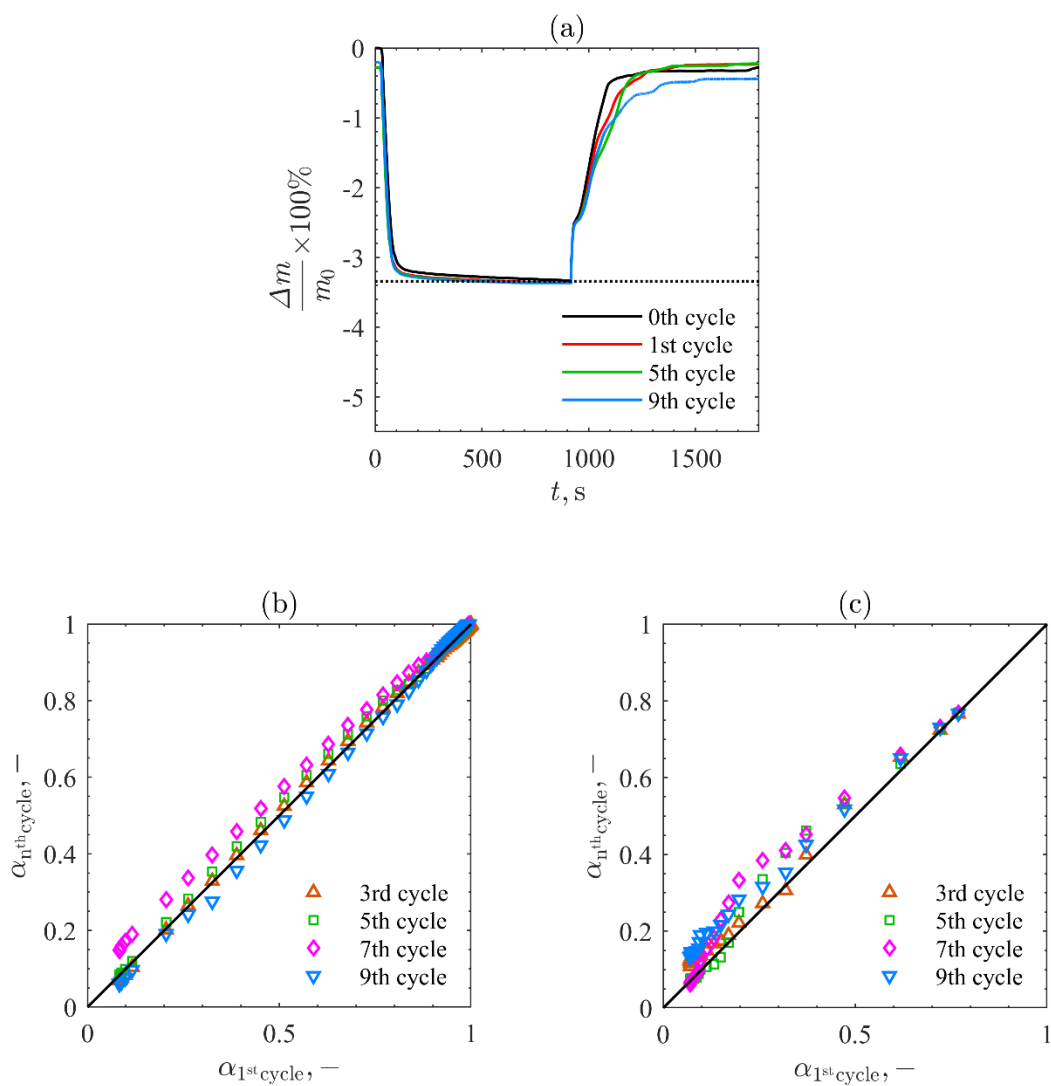
Figure 6.14 For initially-Fe_2O_3 samples, (a) superimposed reduction-oxidation cycle mass changes relative to initial sample mass; parity plots for (b) thermal reduction and (c) re-oxidation comparing conversion to the first cycle.

6.5   Solid Characterization

X-ray diffractometry (XRD, PANalytical X'Pert PRO Alpha-1 diffractometer) was performed on reacted and unreacted samples of Fe_2O_3 and Fe_3O_4 at diffraction angles 2θ of 20–70° to verify sample compositions. Figure 6.15 shows the intensity peaks for both species, with the unreacted (a) Fe_3O_4 and (b) Fe_2O_3 sample peaks shifted up for comparison with the corresponding (a) thermally reduced and (b) oxidized samples, respectively. The unreacted sample crystalline structures were first verified via comparison to star-quality XRD peaks from the PDF4+ database [163]. Reacted samples were then compared to their unreacted form to confirm complete thermal reduction and/or oxidation. Good agreement between sample peak locations and relative intensities was observed for both oxidation states with their unreacted counterparts, without apparent 2θ shifting or evidence of intermediate phases.
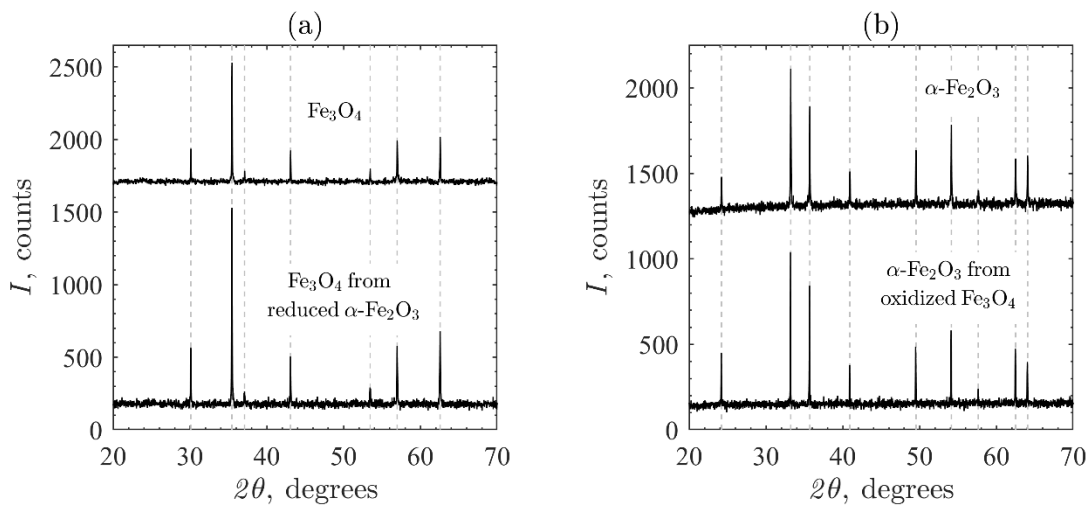
Figure 6.15 Intensity as a function of 2θ angle from X-ray diffractometry measurements for (a) an unreacted Fe_3O_4 sample and Fe_3O_4 produced via thermal reduction of Fe_2O_3, (b) an unreacted Fe_2O_3 sample and Fe_2O_3 produced from oxidation of Fe_3O_4.

In-situ XRD (PANalytical Empyrean with Anton-Paar 1200N Hot Stage) was also performed to examine changes in the crystalline structures of oxidized Fe_3O_4 samples at elevated temperatures. Non-reacting samples of Fe_2O_3 were heated to 1073 K in an atmospheric environment with diffraction peaks obtained in intervals of 200 K. The resulting structures were compared to PDF4+ database entries for both α-Fe2O3 and γ-Fe_2O_3 and are shown in Figure 6.16. While there was some evidence of peak shifting, particularly at higher *2θ* peaks, to lower angles, phase transition to γ-Fe_2O_3, indicated by loss of the first high-intensity peak between $30° < 2θ < 40°$, was not observed. It was, therefore, concluded that the Fe_3O_4 samples from the kinetic analysis were oxidized to α-Fe_2O_3, consistent with the proposed oxidation pathway hypothesized in Figure 6.10c-d.
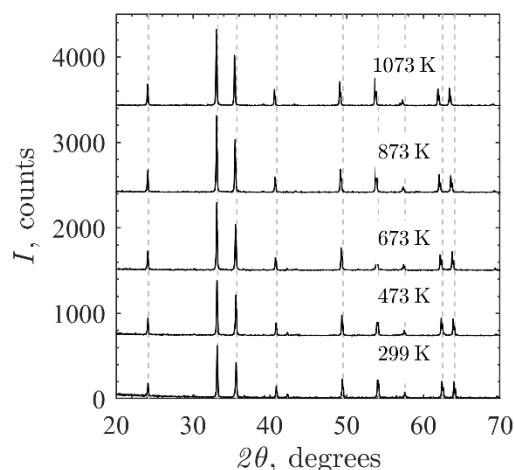
Figure 6.16 Intensity as a function of *2θ* angle from X-ray diffractometry measurements of a non-reacting Fe_2O_3 sample for temperatures of 299 – 1073 K.

Scanning electron microscopy (SEM, Zeiss Ultra 60 FE-SEM) was used to study particle size and morphology for the Fe_2O_3 and Fe_3O_4 samples (a) before and (b) after thermal reduction, shown in Figure 6.17, and oxidation, shown in Figure 6.18, respectively. The majority of unreacted Fe_2O_3 particles were much smaller than the 5 μm maximum

specified diameter, with smooth surfaces and near spherical shapes. Following thermal reduction, the particle sizes grew significantly, resulting in less spherical, slightly porous particles. The unreacted Fe_3O_4 particles had a relatively wide range of particle sizes despite sieving, as well as more angular initial surface shapes. Oxidation resulted in a porous, angular particle sample in which the smaller particles were no longer present. However, the apparent particle size growth was less significant relative to the initially-Fe_2O_3 sample.
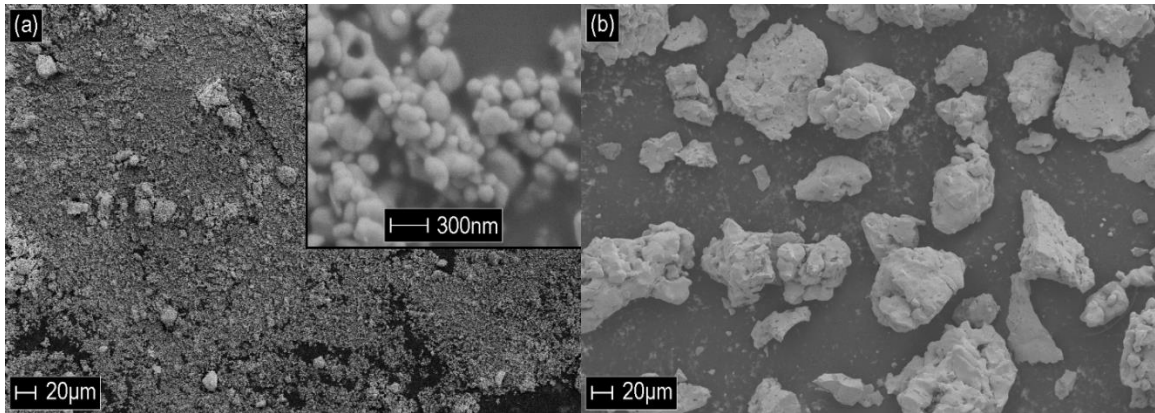
Figure 6.17 Scanning electron microscopy images for (a) an unreacted Fe_2O_3 sample and (b) Fe_3O_4 produced via thermal reduction of Fe_2O_3.
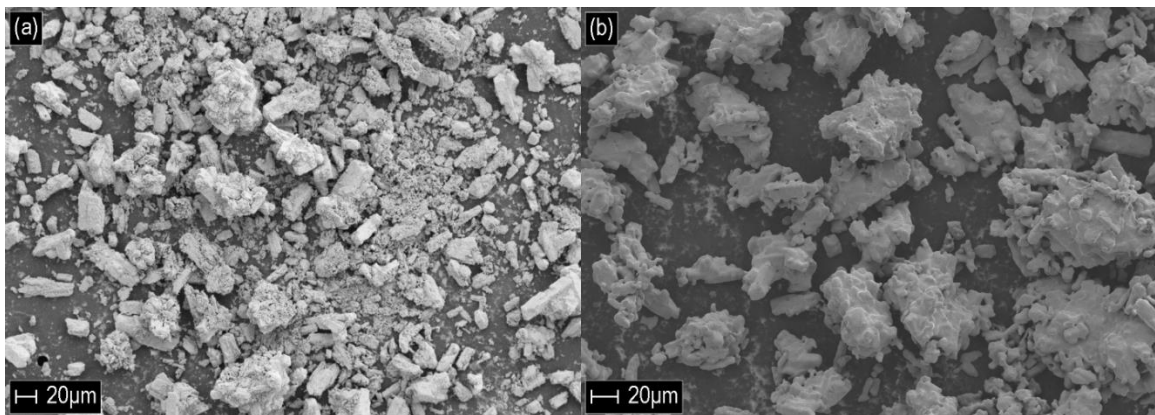
Figure 6.18 Scanning electron microscopy images for (a) an unreacted Fe_3O_4 sample and (b) Fe_2O_3 produced via oxidation of Fe_3O_4.

6.6   Conclusions

Thermodynamic and kinetic analyses were performed to evaluate two-step, Fe_2O_3/Fe_3O_4 reduction-oxidation reactions coupled to an Air Brayton cycle for thermochemical energy storage and electricity production. Due to high Fe_2O_3 thermal reduction temperatures, increasing the solar concentration ratio to 4000 suns mitigated radiative losses and produced a cycle efficiency of 46.0%, comparable to Co_3O_4/CoO at equivalent conditions. Fe_2O_3 thermal reduction was described by an Avrami-Erofe'ev nucleation model of order $n = 1.26$ and a power-law O_2 partial pressure dependency. Non-isothermal Fe_3O_4 oxidation revealed two reaction rate peaks, suggesting a mechanism transition consistent with known oxidation pathways but not fully captured by modeling. Further study of early oxidation mechanisms is required. At higher isothermal temperatures, significant Fe_3O_4 oxidation occurred within 20 s. Pressure-swing redox cycling showed reduced conversion after a bakeout due to thermodynamic limitations, but the capacity did not systematically change over the following nine cycles. SEM revealed significant Fe_2O_3 particle growth and apparent surface area loss from thermal reduction.

The combined thermodynamic-kinetic analysis indicated superior maximum theoretical efficiencies for concentrating solar infrastructure capable of very high solar concentration ratios. Kinetic analyses and cycling demonstrated rapid conversion at representative temperature and pressure conditions for both reactions. This work is an important prerequisite for guiding the design and optimization of solar thermochemical reactors and non-solar re-oxidizers. These results establish an important upper bound on the performance of future implementations and inform the design and optimization of thermochemical infrastructure.

CHAPTER 7. AL-DOPED SrFeO$_{3-\delta}$ CYCLES FOR AIR SEPARATION

7.1   Introduction

The reversible reduction and oxidation (redox) of Al-doped SrFeO$_{3-\delta}$ is presented for air separation, where the redox reaction is represented in Kröger–Vink notation as:

$$2Fe_{Fe}^{\times} + O_O^{\times} \rightleftharpoons 2Fe_{Fe}^{'} + V_O^{\cdot\cdot} + \frac{1}{2}O_{2(g)} \tag{7.1}$$
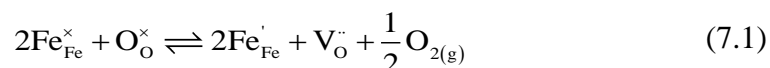
where the non-labile Sr and Al are omitted, and where the oxygen vacancies V$_O$ may assume a variety of forms including ideal or interacting point defects or clusters. Thermodynamic characterization was performed by applying the compound energy formalism (CEF) to thermogravimetry at chemical equilibrium for Al-concentrations from 0 to 0.20, temperatures from 673 – 1373 K, and O$_2$ partial pressures from 0.01 – 0.90 bar, capturing oxygen vacancy formations and complex sublattice interactions. Model results were used to determine the partial molar enthalpies and entropies. These were input to a thermodynamic cycle analysis for separating O$_2$ from air to produce pure streams of N$_2$ for NH$_3$ production, and the cycle performance was analyzed over a range of conditions. Additionally, 10 redox experiments were performed in an upward flow reactor directly irradiated by a high-flux solar simulator to examine oxide cyclability.

7.2   Experimental

Samples of $SrFe_{1-y}Al_yO_{3-\delta_0}$, $0 \leq y \leq 0.20$ (SAF) were synthesized using a sol-gel method [164] from hydrated metal nitrate salts (ALFA AESAR, ACS, ≥98%). ~0.1 M solutions in ultrapure H_2O were prepared and mixed with citric acid at 3.5:1 molar ratios to full dissolution, producing yellow-orange, semitransparent liquids. The solutions were heated under constant stirring to nearly 100 °C to drive evaporation. When most of the liquid was evaporated, stirring was halted, and the samples gelated, characterized by volume growth and color change to a mixture of yellow and dark red/brown. Samples were dried, heated at > 300 °C to produce ash, then further heated until auto-ignition of the citric acid. The products were ground with a pestle and mortar and transferred to alumina crucibles for calcination.

Samples were calcined in a high temperature box furnace (SENTROTECH 4x4x5" 1600C High Temperature Box Furnace) in two steps: 1) heating twice to 2/3 the minimum melting temperature (K) of the expected binary metal oxides for 10h, to combust remaining organics and form binary metal oxides; 2) heating once to 1573 K for 24h, to promote the formation of perovskite phases. A temperature of 1573 K was required for homogenous, single-phase perovskites approaching a cubic structure. Samples agglomerated in the furnace and were again ground with a pestle and mortar.

Crystalline structures were determined by comparing results from powder x-ray diffractometry (XRD), shown in Figure 7.1 for a) undoped $SrFeO_{3-\delta_0}$ and b) $SrFe_{1-y}Al_yO_{3-\delta_0}$ with Al-dopant levels of 0.05, 0.10, 0.15 and 0.20, to reference peaks from the PDF 4+ Database [163]. The vertical dashed lines represent the peaks of a cubic $SrFeO_{3-\delta}$

reference. Samples showed increasing peak broadening and shifting with increasing values of y. While compositions with y = 0.25, 0.50, and 0.75 were also synthesized, XRD indicated an increasing presence of secondary phases. Therefore, those samples were not considered in the thermodynamic analysis.
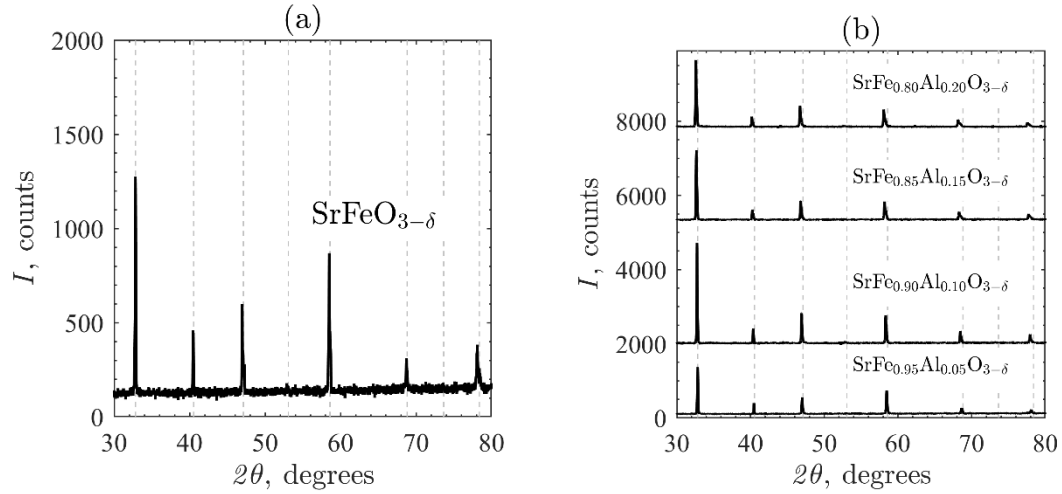
Figure 7.1. Intensity as a function of 2θ angle from X-ray diffractometry measurements for (a) three $SrFeO_{3-\delta}$ samples synthesized with maximum temperatures of 1373, 1373, and 1573 K and final cooling rates of 3, 20, and 20 K·min^{-1}, respectively and (b) $SrFe_{1-y}Al_yO_{3-\delta}$ samples with dopant concentrations of 5, 10, 5, and 20%, respectively. Vertical dashed lines are from a cubic $SrFeO_{3-\delta}$ reference in the PDF4+ Database.

A series of thermogravimetric analysis experiments (TGA, Netzsch STA 449 F3 Jupiter ±1 μg) was performed using the experimental process summarized in Figure 7.2 to determine non-stoichiometry at chemical equilibrium [35]. Powder samples were mounted on an Al_2O_3 crucible shielded with a platinum foil (Sigma-Aldrich 0.025MM Thick 99% Pt Foil 267244-1.4G), and sample temperatures were measured by an S-type thermocouple. The initial masses were measured before and after testing with an analytical balance (Mettler-Toledo ML54, ± 0.1mg) to verify the total mass change measured by TGA. Samples were progressively heated at rates of 20 K·min^{-1} to four temperatures from T =

116

673 to 1373 K and were thermally reduced and oxidized in $\Delta t = 30$ min steps in 1-90% O_2–Ar. All steps were performed at a total pressure of 1 bar and a constant total gas flow of 200 $mL_N \cdot min^{-1}$ (where L_N refers to liters at standard conditions, *i.e.*, 273 K and 1 bar). After, samples were cooled to room temperature under 200 $mL_N \cdot min^{-1}$ Ar. A blank run under identical conditions was performed to correct for the influences of buoyancy and gas dynamics.
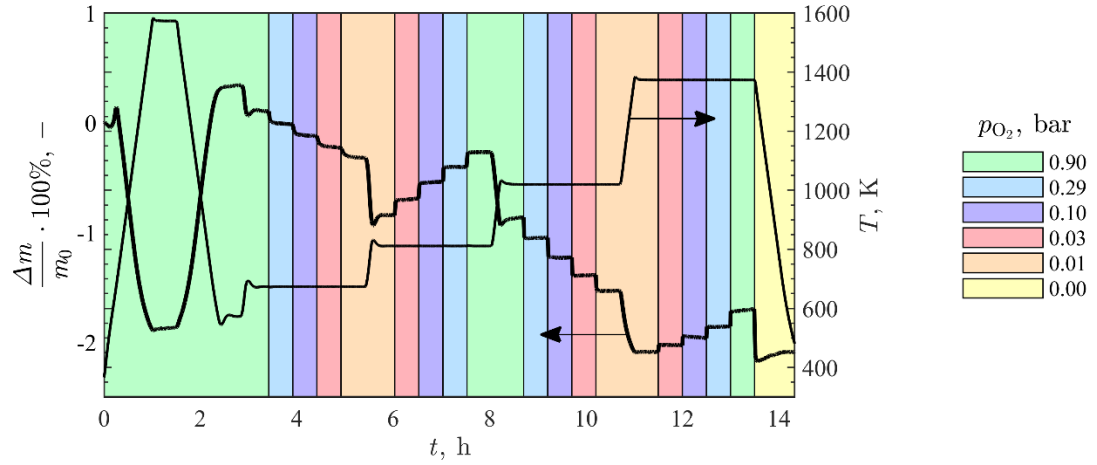
Figure 7.2. $SrFe_{1-y}Al_yO_{3-\delta}$ sample temperature, and relative mass change, and O_2 partial pressure settings for an equilibrium experiment, where pairs of conditions between 673–1373 K and 1–90% O_2–Ar were established with 30 min dwell times to allow for sample equilibrium.

The temporal sample nonstoichiometry was calculated from the temporal mass change as:

$$\Delta\delta(t) = -2\frac{M_0(\delta_0)}{M_{O_2}}\left[\frac{\Delta m(t)}{m_0}\right] \tag{7.2}$$

where $\Delta m(t)$ is the mass change at time t; m_0 is the initial sample mass, from 100-200 mg according to particle density; M_{O_2} is the molar mass of oxygen; δ_0 is the initial nonstoichiometry; and M_0 is the initial sample molar mass, defined as:

$$M_0\left(\delta_0\right) = M_{Sr} + \left(1-y\right)M_{Fe} + yM_{Al} + \frac{3-\delta_0}{2}M_{O_2} \qquad (7.3)$$

At the end of each 30 min (T, p_{O_2}) step, δ was assumed to be the equilibrium state of the sample, $\delta = \delta_\infty(T, p_{O_2})$, and was used to model the non-stoichiometry as a function of T and p_{O_2}. The δ_0 was determined during computational modeling via the minimization of the sum of square errors SSE between modeled and experimental δ.

To examine repeatability of the redox reactions, cycling experiments, summarized in Figure 7.3 and Table 7.1, were performed in an upward flow reactor (UFR) [110] coupled to a high flux solar simulator (HFSS) [121]. A SrFeO$_{3-\delta}$ sample was placed on a platinum foil within the UFR crucible and thermally reduced at low vacuum by the HFSS center lamp. Oxidation was performed off-sun immediately after, while the sample cooled to near room temperature, under an O_2 flow at atmospheric pressure. The Ar sweep gas and oxidizing O_2 flows were maintained by mass flows controllers (Bronkhorst F-201CV-20K-MAD-33-V). The pressure during the thermal reduction was measured by a pressure transducer (Omega PXM309-0.35A10V), and the temperature below the sample bed was monitored by a thermocouple probe (Omega OMEGACLAD XL Type K KQXL-116). This configuration ensured that cycles proceeded under similar conditions, without causing mass loss due to thermocouple embedding.

The thermal reduction was temporally measured downstream of the sample by mass spectrometry (MS; Omnistar ThermoStar GSD320 Gas Analysis System). The MS O_2 ion current readings were calibrated to O_2 molar flow rates using the mass flow controller and corrected for O_2 dispersion. There was no apparent systematic decline in the calculated molar O_2 flow rates with increasing cycle number. One final cycle was performed on the sample with a K-type thermocouple embedded directly in the sample bed, in order to better estimate the thermal reduction temperatures.
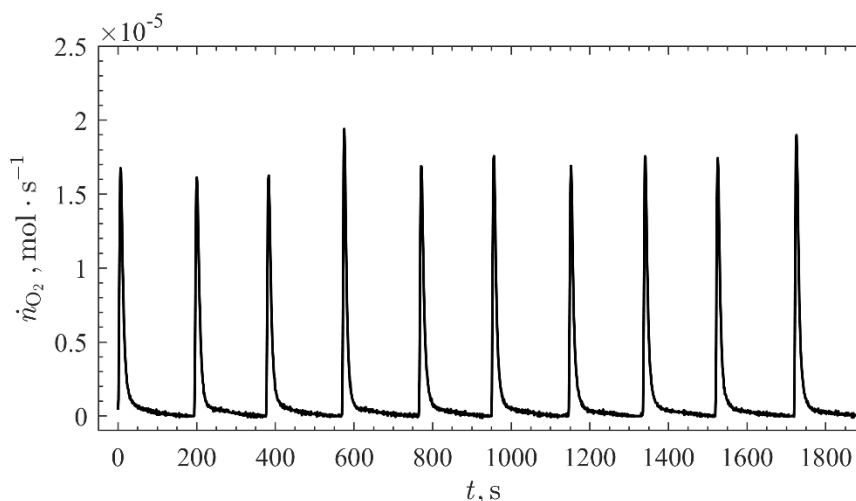
Figure 7.3. Molar O_2 flow rates with time from 10 SrFeO$_{3-\delta}$ thermal reduction-oxidation cycles performed in an upward flow reactor coupled to a high-flux solar simulator, at pressures and temperatures of approximately 59.4 mbar and 1153 K, respectively.

Table 7.1. SrFeO$_{3-\delta}$ cycling conditions during the on-sun thermal reduction and off-sun oxidation steps. Mean values from the 10 cycles are reported with 95% confidence intervals estimated via a t-distribution. Temperature are reported at their final, near-steady state values.

Variable	Thermal Reduction	Oxidation
Initial sample mass, g	0.250 ± 0.000	–
Lamp power, kW	5.01 ± 0.00	–
Total pressure, mbar	59.4 ± 0.2	1.01
Bed temperature, K	1153	< 1153
Bottom temperature, K	796 ± 5	$< 796 \pm 5$
Ar flow rate, $L_N \cdot min^{-1}$	1.02 ± 0.00	0
O$_2$ flow rate, $L_N \cdot min^{-1}$	0	1.00
O$_2$ partial pressure, mbar	(8.13 ± 0.15) E-3	–

7.3   Modeling

To predict $\delta = f(T, p_{O_2})$, the standard Gibbs free energy of the nonstoichiometric perovskite phase of SrAl$_y$Fe$_{1-y}$O$_{3-\delta}$ was defined using the CEF [78] as:

$$G_{SAF}^{P} = \sum_i \left({}^{\circ}G_i \prod_{k \in S_i} y_k \right) + RT \sum_m \left(\nu_m \sum_{k \in S_m} y_k \ln y_k \right) + {}^{E}G_{SAF}^{P} \qquad (7.4)$$

where R is the universal gas constant. The end members i in the first term are defined in Table 7.2, and S_i is the subset of site fractions y_k of the constituent ions and oxygen vacancies V_O present in the corresponding end member. The second term represents the mixing entropies for the A, B, and O sublattices at stoichiometric ratios of $\nu_1 = \nu_2 = 1$ and $\nu_3 = 3$, respectively, and S_m is the subset of y_k present on each sublattice m. The third term represents the excess Gibbs energy, which accounted for intra-sublattice interactions via Redlich-Kister Polynomial expressions [165] as:

$$
{}^{E}G_{SAF}^{P} = \begin{aligned}
& y_{Fe^{4+}} y_{O^{2-}} \sum_{n} y_{Fe^{3+}} L^{n}_{Sr^{2+}:\{Fe^{4+},Fe^{3+}\}:O^{2-}} \left(y_{Fe^{4+}} - y_{Fe^{3+}} \right)^{n} + \ldots \\
& y_{Fe^{4+}} y_{O^{2-}} \sum_{n} y_{Al^{3+}} L^{n}_{Sr^{2+}:\{Fe^{4+},Al^{3+}\}:O^{2-}} \left(y_{Fe^{4+}} - y_{Al^{3+}} \right)^{n} + \ldots \\
& y_{Fe^{4+}} y_{O^{2-}} \sum_{n} y_{V_O} L^{n}_{Sr^{2+}:Fe^{4+}:\{O^{2-},V_O\}} \left(y_{O^{2-}} - y_{V_O} \right)^{n} + \ldots \\
& y_{Fe^{4+}} y_{O^{2-}} \sum_{n} y_{Fe^{3+}} y_{Al^{3+}} L^{n}_{Sr^{2+}:\{Fe^{4+},Fe^{3+},Al^{3+}\}:O^{2-}}
\end{aligned}
\tag{7.5}
$$

where the interaction terms $L_{A:B:O}$ are defined in Table 7.3 and where brackets $\{\ \}$ indicate the interacting constituents. The site fractions were defined from $\Delta\delta$ measurements by applying sublattice conservation and electroneutrality conditions. The site fraction of Al^{3+} was $y_{Al^{3+}} = y$. A detailed definition of the CEF model and is provided in Appendix C.

Table 7.2. The six end members used in the compound energy model for the standard Gibbs free energy of $SrFe_{1-y}Al_yO_{3-\delta}$ and their definitions in terms of the known standard Gibbs free energies of binary metal oxides, O_2, and linear fitted terms with temperature.

End Member	Definition
${}^{\circ}G_{Sr^{2+}:Fe^{4+}:O^{2-}}$	$G_{SrO} + \dfrac{1}{2}{}^{\circ}G_{Fe_2O_3} + \dfrac{1}{4}{}^{\circ}G_{O_{2(g)}} - (16.9 \pm 0.62) - (1.78 \pm 0.00)\,T$
${}^{\circ}G_{Sr^{2+}:Fe^{3+}:O^{2-}}$	${}^{\circ}G_{SrO} + \dfrac{1}{2}{}^{\circ}G_{Fe_2O_3} + \dfrac{1}{4}{}^{\circ}G_{O_{2(g)}} + (24.4 \pm 0.62) - (1.45 \pm 0.00)\,T$
${}^{\circ}G_{Sr^{2+}:Al^{3+}:O^{2-}}$	${}^{\circ}G_{SrO} + \dfrac{1}{2}{}^{\circ}G_{Al_2O_3} + \dfrac{1}{4}{}^{\circ}G_{O_{2(g)}}$
${}^{\circ}G_{Sr^{2+}:Fe^{4+}:V_O}$	${}^{\circ}G_{Sr^{2+}:Fe^{4+}:O^{2-}} - \dfrac{3}{2}{}^{\circ}G_{O_{2(g)}}$
${}^{\circ}G_{Sr^{2+}:Fe^{3+}:V_O}$	${}^{\circ}G_{Sr^{2+}:Fe^{3+}:O^{2-}} - \dfrac{3}{2}{}^{\circ}G_{O_{2(g)}}$
${}^{\circ}G_{Sr^{2+}:Al^{3+}:V_O}$	${}^{\circ}G_{Sr^{2+}:Al^{3+}:O^{2-}} - \dfrac{3}{2}{}^{\circ}G_{O_{2(g)}}$

Table 7.3. The nine interaction terms of order $n = 0$, 1, or 2 used in the excess Gibbs free energy term of the compound energy model for the standard Gibbs free energy of $SrFe_{1-y}Al_yO_{3-\delta}$. Definitions are given as second-order fitted terms with temperature.

Interaction Term	Definition		
	n = 0	n = 1	n = 2
$L^n_{Sr^{2+}:\{Fe^{4+},Fe^{3+}\}:O^{2-}}$	$(2.99 \pm 1.87) - (0.26 \pm 0.00)\,T$	$(-0.02 \pm 0.00)\,T$	-
$L^n_{Sr^{2+}:\{Fe^{4+},Al^{3+}\}:O^{2-}}$	$(0.21 \pm 0.01)\,T$	$(0.25 \pm 0.01)\,T$	-
$L^n_{Sr^{2+}:Fe^{4+}:\{O^{2-},V_O\}}$	$(1.08 \pm 0.01)\,T$	$(0.47 \pm 0.01)\,T$	-
$L^n_{Sr^{2+}:\{Fe^{4+},Fe^{3+},Al^{3+}\}:O^{2-}}$	$(-0.91 \pm 0.02)\,T$	$(-0.30 \pm 0.02)\,T$	$(1.44 \pm 0.02)\,T$

The modeled δ were determined via minimization of the differential change in the Gibbs free energy of the reacting $SrAl_yFe_{1-y}O_{3-\delta}$–$O_2$ system, represented as:

$$dG^P_{SAF} = -\frac{1}{2}\left[\,^\circ G_{O_2} + RT \ln p_{O_2}\right]d\delta \tag{7.6}$$

where $\,^\circ G_{O_2}$ is the standard Gibbs free energy of O_2 and a χ^2 form was used for the objective function, given as:

$$\lambda^2_{min} = \sum_s \sum_r \frac{\left[\dfrac{d\,^\circ \hat{G}^P_{SAF}}{d\delta_{s,r}}\left(\Delta\delta_{s,r}, T_{s,r}, y_s; \beta_j, \delta_{0,s}\right) + \frac{1}{2}RT_{s,r}\ln\left(p_{O_2}\right)_{s,r}\right]^2}{\sigma^2_{s,r}} \tag{7.7}$$

where the T, p_{O_2} and $\Delta\delta$ data for each sample s and experimental measurement r were used to simultaneously fit the unknown parameter vectors β_j and $\delta_{0,s}$ via a Nelder-Mead nonlinear minimization algorithm. The empirical terms β_j are compiled in Table 7.2 and for the end members and interaction terms, respectively, and the δ_0 for each sample in Table

7.4. The derivative of G_{SAF}^P was approximated by central differencing, performed at each experimental $\Delta\delta$.

The experimental data were assumed to be independent and identically distributed, allowing the total variance $\sigma_{s,r}^2$ to reduce to an undetermined constant. Ninety-five percent confidence intervals for the fitted parameters shown in Table 7.2 though Table 7.4 were computed from the upper 95% χ^2 value of λ_{min}^2. As the β_j were correlated, 95% confidence intervals for the thermodynamic parameters were computed from the input measurement errors via a Monte Carlo analysis with 200 iterations.

The SrAl$_y$Fe$_{1-y}$O$_{3-\delta}$ partial reduction enthalpy $\partial H_{O_2}/\partial\delta$ and standard entropy $\partial°S_{O_2}/\partial\delta$ were represented implicitly in the Van't Hoff equation, given as:

$$-R\ln\frac{p_{O_2}}{p_0} = \frac{\partial H_{O_2}}{\partial\delta}\left(\frac{1}{T}\right) - \frac{\partial°S_{O_2}}{\partial\delta} \tag{7.8}$$

Both property partial derivatives were computed via regression of the experimental $\ln p_{O_2}$ vs. T^{-1} at each δ, assuming approximately constant values with temperature. The total molar redox enthalpy of SrAl$_y$Fe$_{1-y}$O$_{3-\delta}$ from some δ to some $\delta + \Delta\delta$ was calculated as:

$$\Delta H_{SAF} = \frac{1}{2}\int_{\delta}^{\delta+\Delta\delta} \frac{\partial H_{O_2}}{\partial\delta'}d\delta' \tag{7.9}$$

A thermodynamic analysis of an idealized air separation cycle, shown in Figure 7.4, was performed using SrAl$_y$Fe$_{1-y}$O$_{3-\delta}$ as an air-purification material. The cycle operates in two steps: 1) the SrAl$_y$Fe$_{1-y}$O$_{3-\delta}$ thermal reduction in a solar thermochemical reactor with concentrated solar radiation to produce an oxygen-deficient oxide and O$_2$ gas; and 2) the

123

re-oxidation of the reduced $SrAl_yFe_{1-y}O_{3-\delta-\Delta\delta}$ with air in an air separator reactor to close the cycle and produce a high-purity stream of N_2.
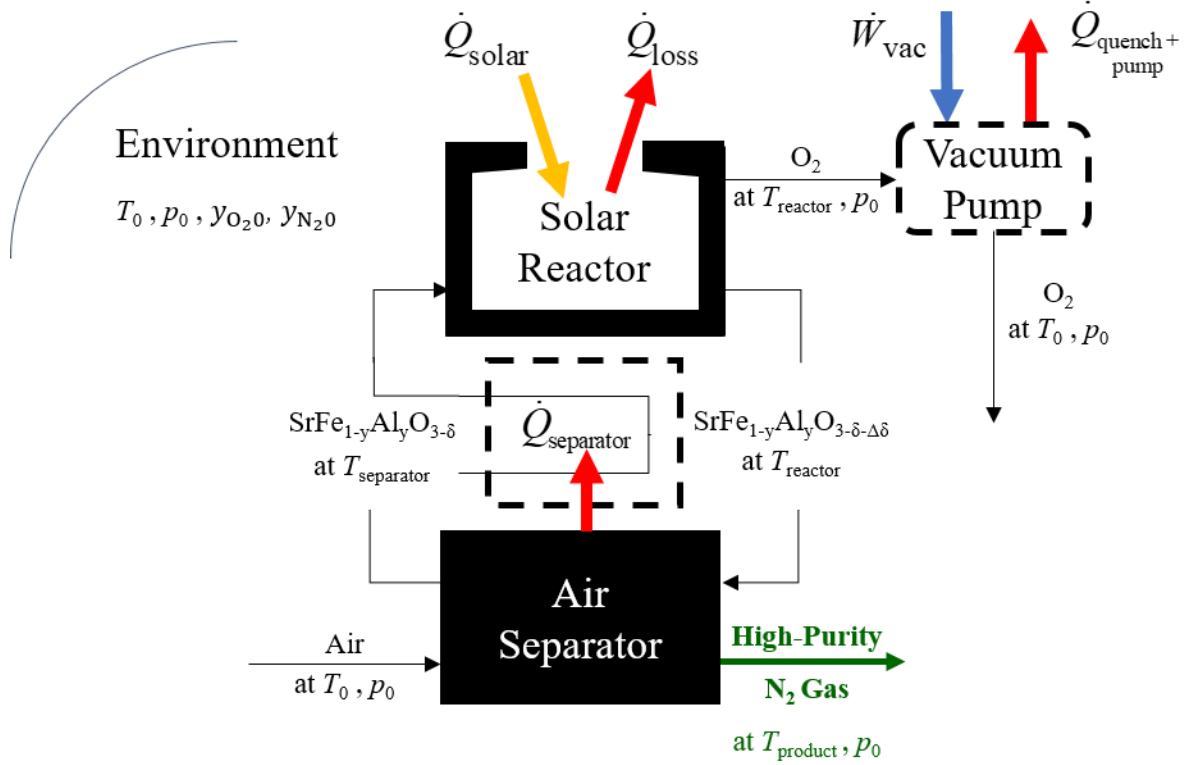
Figure 7.4. System schematic of the solar thermochemical air separation cycle for producing high-purity N_2, based on $SrFe_{1-y}Al_yO_{3-\delta}$ redox reactions. Optional recuperative and vacuum pumping stages, shown as dashed outlines, are included.

The solar thermochemical reactor was modeled as a directly-irradiated, well-insulated, isothermal, blackbody receiver containing atmospheric air, with a steady flow of reacting $SrAl_yFe_{1-y}O_{3-\delta}$ particles at $T_{reactor}$, normalized to 1 mol·s^{-1}. Isothermal, reversible vacuum pumping at T_0 to promote the reduction favorability according to Le Chatelier's principle was optionally considered. The air separator was modeled as an idealized counterflow configuration where reduced $SrAl_yFe_{1-y}O_{3-\delta-\Delta\delta}$ particles entered at $T_{reactor}$ and $\delta + \Delta\delta$ and came into thermochemical equilibrium with the exiting N_2-rich product gas stream at $T_{product}$ via heat transfer and oxidation. The atmospheric airstream entered

opposite the particles and similarly came into thermochemical equilibrium with the exiting, re-oxidized particles at $T_{separator} \geq T_0$ and δ. The air separator was assumed to be closed to the atmosphere apart from the entering air stream. Waste heat $\dot{Q}_{separator}$ recovery was considered via an ideal counter-flow heat exchanger, but it could also be utilized in an NH_3-production cycle downstream. The specific heat of $SrAl_yFe_{1-y}O_{3-\delta}$ was approximated using the high-temperature limit of Debeye theory as $c_p = 3R(5 - \delta)$.

Throughout the analysis, atmospheric air was thermodynamically approximated as a $y_{O_2,0} = 0.21$ $O_2 : y_{N_2,0} = 0.79$ N_2 ratio mixture at a pressure $p_0 = 1$ bar and $T_0 = 298.15$ K. Ideal gas behavior and local gas/solid thermal equilibrium were assumed. The N_2 purity was reported as:

$$\phi = 0.99\phi' = 0.99\left(\frac{\dot{n}_{N_2,product}}{\dot{n}_{N_2,product} + \dot{n}_{O_2,product}}\right) \tag{7.10}$$

where the 0.99 scaling corrected for the presence of Ar and trace gases in atmospheric air, compared to the purity according to the thermodynamic approximation of air ϕ'. $\dot{n}$ is the molar flow rate and was calculated for the product gases exiting the separator.

The maximum theoretical thermodynamic cycle efficiency for the thermochemical air separation cycle including heat recuperation was defined as:

$$\eta = \frac{\dot{W}_{ideal}}{\dot{Q}_{solar} - \dot{Q}_{separator} + \dot{W}_{vac}} \tag{7.11}$$

where $\dot{W}_{vac}$ is the vacuum pump work, zero for a solar reactor with atmospheric air; $\dot{Q}_{separator} \geq 0$ was defined from the air separator energy balance; and $\dot{W}_{ideal}$ is the work requirement of the ideal air separation process, given as:

$$\dot{W}_{ideal} = \dot{n}_{air} R T_0 \ln \frac{\left(\phi'\right)^{\phi'} \left(1-\phi'\right)^{1-\phi'}}{\left(y_{N_2,0}\right)^{y_{N_2,0}} \left(y_{O_2,0}\right)^{y_{N_2,0}}} \tag{7.12}$$

The solar energy $\dot{Q}_{solar}$ required to drive the endothermic reduction of SrAl$_y$Fe$_{1-y}$O$_{3-\delta}$ was represented as:

$$\dot{Q}_{solar} = \frac{\dot{n}_{SAF} \Delta H_{SAF}}{\eta_{abs}} = \dot{n}_{SAF} \Delta H_{SAF} \left(1 - \frac{\sigma T_{reactor}^4}{IC}\right)^{-1} \tag{7.13}$$

where η_{abs} is the solar absorption efficiency, σ is the Stefan-Boltzmann constant, $I = 1$ kW·m^{-2} is the direct normal solar irradiance, and $C = 1000$ is the concentration ratio of the concentrating infrastructure.

7.4   Perovskite Characterization

Equilibrium δ for SrAl$_y$Fe$_{1-y}$O$_{3-\delta}$ were determined using TGA and are given in Figure 7.5 for $0.0 < y < 0.2$ as functions of a) T at 29% O$_2$-Ar and b) p_{O_2} at $T = 1100$ K. The $\Delta\delta$ values were defined relative to measurements at $T = 673$ K, $p_{O_2} = 0.29$ bar, the measured values closest to expected conditions for SrAl$_y$Fe$_{1-y}$O$_{3-\delta}$ exiting the air separator. The reducibility of SrAl$_y$Fe$_{1-y}$O$_{3-\delta}$ in air for the ΔT was between $\Delta\delta = 0.24$ and 0.17 for $y = 0$ and 0.20, respectively. Relative to the calculated δ_0, however, maximum $\Delta\delta$ values exceeded 0.30. Decreasing p_{O_2} to 0.01 bar, as shown in Figure 7.5b, increased all $\Delta\delta$ by

approximately 0.03 at 1373 K, illustrating the $\Delta\delta$ attainable in a windowed solar receiver with an inert sweep gas and/or vacuum pump.
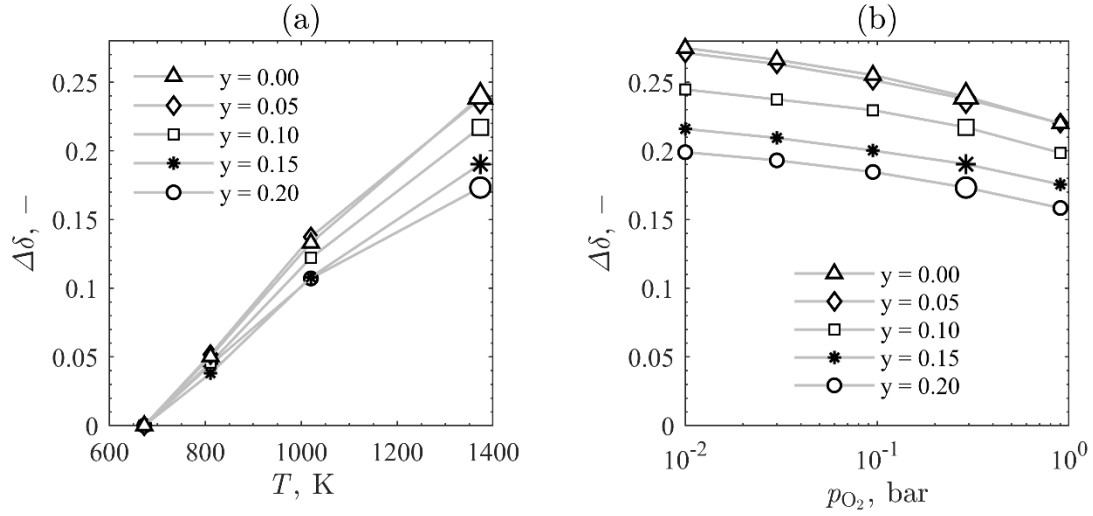
Figure 7.5. Measured $SrFe_{1-y}Al_yO_{3-\delta}$ nonstoichiometry with Al-dopant concentrations of $0-0.20$, at: (a) 29% O_2–Ar for temperatures from 673 to 1373 K; and (b) at 1100 K for 1 to 90% O_2–Ar.

The δ_0 were bounded during fitting by: 1) a maximum of $0.5 - \Delta\delta_{max}$, the largest measured nonstoichiometry difference; and 2) a minimum of $y/2$ according to electroneutrality, assuming non-labile Al^{3+} cations and a maximum iron charge of Fe^{4+}. The δ_0 at each y were between $\delta_0 = 0.08$ and 0.15 and are shown in Table 7.4 with $\Delta\delta_{max}$ and the difference from theoretical minimum.

Table 7.4. For 0–20% Al, from left to right: modeled initial $SrFe_{1-y}Al_yO_{3-\delta}$ sample nonstoichiometry; the maximum measured difference in sample nonstoichiometry; and the difference between the modeled value and the theoretical minimum value.

y, –	δ_0 (± 0.01), –	$\Delta\delta_{max}$, -	$(\delta_0 - \frac{y}{2})$, –
0	0.08	0.36	0.08
0.05	0.13	0.32	0.10
0.10	0.12	0.31	0.07
0.15	0.14	0.27	0.06
0.20	0.15	0.24	0.05

Predicted δ for $SrAl_yFe_{1-y}O_{3-\delta}$ using the CEF are compared to the δ from equilibrium experiments in Figure 7.6. The model was able to accurately capture $SrAl_yFe_{1-y}O_{3-\delta}$ redox behavior for the full range of T, y and p_{O_2}. The most noticeable deviations were at the low $T = 673$ K and high $p_{O_2} = 0.90$ bar for undoped $SrFeO_{3-\delta}$. The excess terms were found to be important in accurately predicting thermodynamic behavior, as ideal solution models generally overestimated the slope of the experimental data on the $3 - \delta$ vs. p_{O_2} plot. As expected, the predicted $3 - \delta$ monotonically increased with p_{O_2}, with slopes approaching zero around $\delta = 0$ and 0.5.
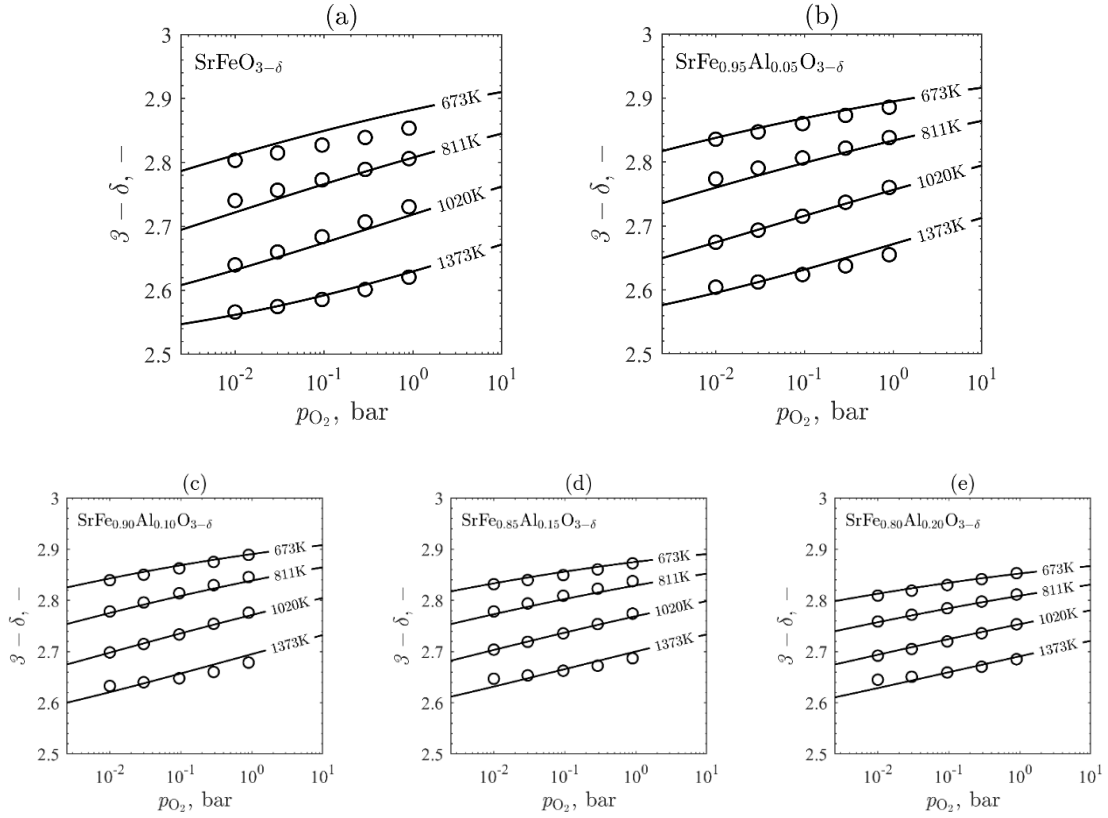
Figure 7.6. Measured (markers) vs. fitted (lines) $SrAl_yFe_{1-y}O_{3-\delta}$ nonstoichiometry via the compound energy formalism for (a) undoped $SrFeO_{3-\delta}$; and Al-dopant concentrations of (b) 0.05, (c) 0.10, (d) 0.15, and (e) 0.20 at 90% O_2–Ar for temperatures between 673 and 1373 K.

As expected for the non-labile dopant Al, increasing y produced smaller changes in δ for equivalent changes in T and p_{O_2}, resulting in increasingly compact $3 - \delta$ curves across T for increasing y. This trend showed that Al-doping produced higher O_2-affinity and a correspondingly higher $\partial H_{O_2}/\partial\delta$. In general, these results suggest a decrease in attainable $\Delta\delta$ for $y > 0$. However, at sufficiently low $p_{O_2} \lesssim 0.1$, the model predicted slightly lower δ for doped $SrAl_yFe_{1-y}O_{3-\delta}$ (Figure 7.6b-e) than undoped $SrFeO_{3-\delta}$ (Figure 7.6a) for some T, suggesting the existence of states between which $\Delta\delta$ and, therefore, the air separation capacity could be comparable between doped and undoped oxides. For air separation at a minimum $T = 673$ K, the doping $\Delta\delta$ penalty was significantly reduced for low $p_{O_2} = 0.001$

bar compared to atmospheric air, as shown in Figure 7.7. For some reduction temperatures between 1073 and 1373 K, low dopant concentrations $y \leq 0.05$ produced $\Delta\delta$ approximately equal to those of $SrFeO_{3-\delta}$.
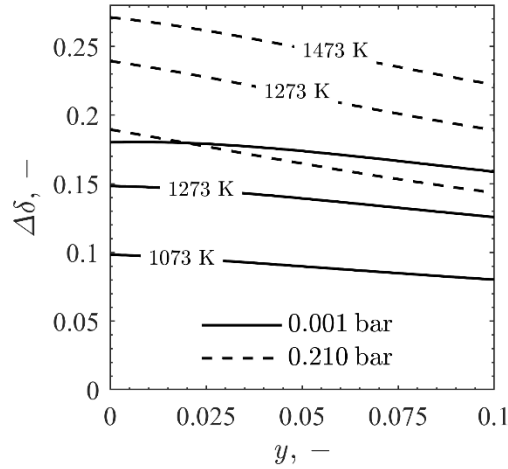
Figure 7.7. Modeled change in $SrAl_yFe_{1-y}O_{3-\delta}$ nonstoichiometry, as a function of dopant concentration, from a) the solar reactor at temperatures of 1073, 1273, and 1473 K and 21% O_2–Ar to b) the air separator particle exit at a temperature of 673 K for atmospheric (21% O_2–Ar, dashed line) and low O_2 (0.1% O_2–Ar, solid line) air.

The $\partial H_{O_2}/\partial\delta$ shown in Figure 7.8a were consistently larger for higher y, consistent with the increased O_2-affinity of $SrAl_yFe_{1-y}O_{3-\delta}$. The $\partial H_{O_2}/\partial\delta$ reached local minima before $\delta = 0.5$. The $\partial°S_{O_2}/\partial\delta$ shown in Figure 7.8b were positive for most $\delta < 0.5$ and decreased to become negative near $\delta = 0$, where nearly all $Fe^{4+} \rightarrow Fe^{3+}$. $\partial°S_{O_2}/\partial\delta$ decreased more rapidly with increasing Al^{3+} site fraction.
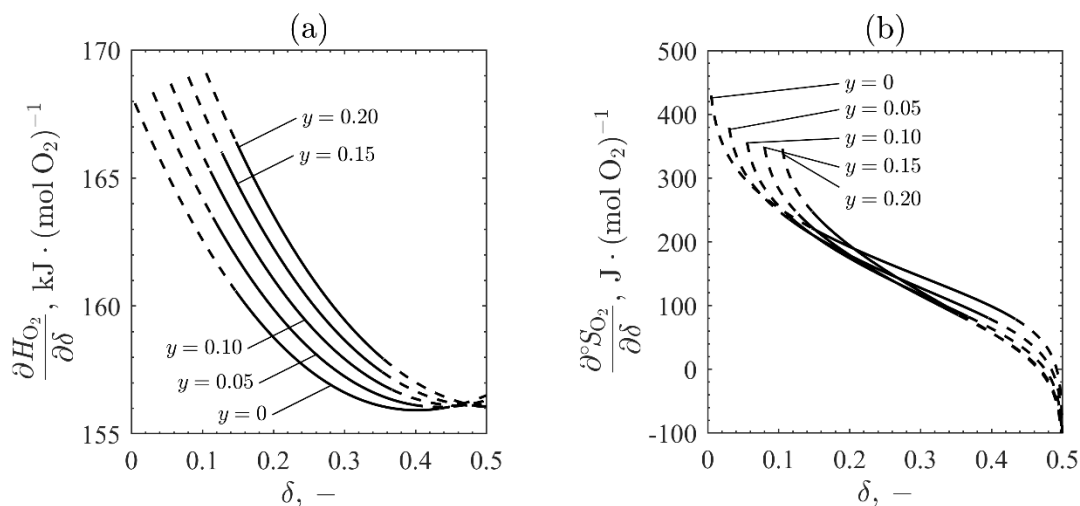
Figure 7.8. SrAl$_y$Fe$_{1-y}$O$_{3-\delta}$ (a) enthalpy and (b) entropy of reduction for Al dopant concentrations of 0.05 to 0.20, represented as partial derivatives with respect to nonstoichiometry. Solid sections of lines indicate the nonstoichiometry ranges of experimental measurements for a given dopant concentration.

The average $\partial H_{O_2}/\partial\delta = 166 \pm 5$ kJ·mol-O$_2$$^{-1}$ over the range of measured δ for undoped SrFeO$_{3-\delta}$, was somewhat lower than previously reported [70, 73, 75, 167] but similar to those for full reduction to brownmillerite from density functional theory [64]. The average $\partial°S_{O_2}/\partial\delta = 264 \pm 22$ J·mol-O$_2$$^{-1}$ was comparable to or slightly higher than other findings, presumably due to the CEF inclusion of the excess entropy compared to ideal solution models.

An SrFeO$_{3-\delta}$ sample was cycled ten times between reduced and oxidized states in an HFSS-coupled UFR, not including an initial bakeout. During redox cycling, the SrFeO$_{3-\delta}$ reached $\Delta\delta$ values near to or exceeding 0.30 within 30 s during the thermal reduction, as shown in Figure 7.9a, in which the first, fourth, seventh and tenth cycles from the onset of reduction are overlaid. The parity plot shown in Figure 7.9b revealed no systematic decrease in reducibility with cycle number, as the fourth and tenth cycle $\Delta\delta$ measurements

exceeded the first cycle after the bakeout, while the seventh cycle showed slightly lower $\Delta\delta$. Variations with cycle number were due to variations in sample heating and O_2 partial pressure, as well as the δ reached in each prior oxidation step.
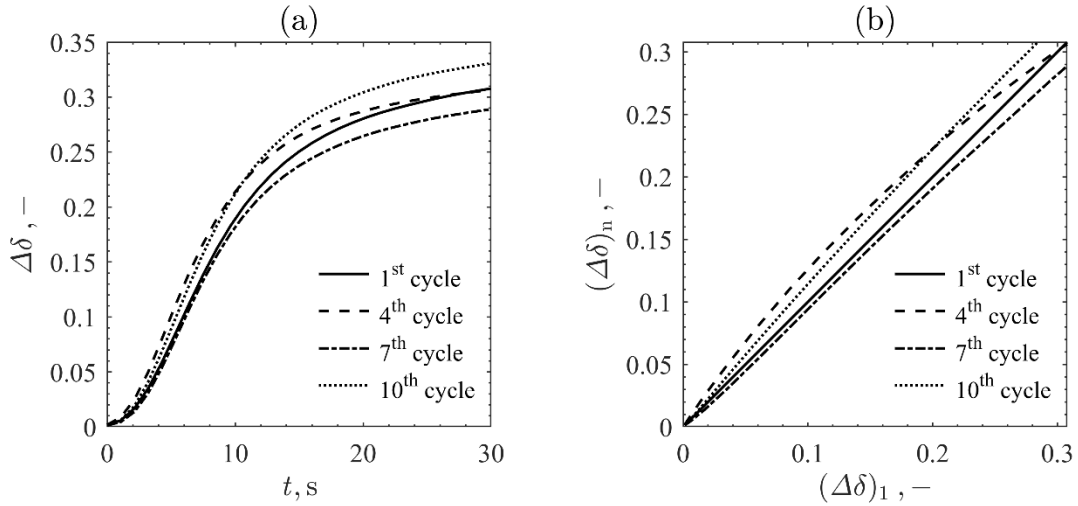
Figure 7.9. For the first, fourth, seventh, and tenth SrFeO$_{3-\delta}$ thermal reduction-oxidation cycles performed in an upward flow reactor: (a) temporal nonstoichiometry change for the first 30s of thermal reduction; (b) a parity plot of nonstoichiometry change during thermal reduction, compared to the values from the first cycle.

7.5   Thermodynamic Cycle Analysis

The modeled equilibrium δ and thermodynamic properties were coupled to an idealized air separation cycle model to predict separation purities, energy requirements, and efficiencies. Figure 7.10a summarizes the air separation cycle performance for undoped SrFeO$_{3-\delta}$ as a function of $\dot{n}_{air}$. With a fixed $T_{reactor} = 1073$ K and $T_{separator} = T_0$, SrFeO$_{3-\delta}$ entered the separator at a constant $\delta = 0.33$ and was oxidized to approach $\delta = 0$ as sufficient airflow was introduced. For $\dot{n}_{air} \gtrsim 0.8$ mol·s^{-1}, $\Delta\delta$ increased only very slightly with airflow. As a result, φ quickly decreased from a maximum near 99%, as there was no further air separation capacity. The corresponding heat flows, depicted in Figure 7.10b,

varied accordingly for $\dot{n}_{air} \gtrsim 0.8\,\text{mol·s}^{-1}$: $\dot{Q}_{solar}$ plateaued at 133 kW due to full reoxidation of the SrFeO$_{3-\delta}$, while $\dot{Q}_{separator}$ decreased from a peak of 102 kW due to greater heat transfer to the airflow. The corresponding $\dot{W}_{ideal}$ peaked simultaneously and decreased slightly due to lower φ despite increasing $\dot{n}_{air}$. The $\dot{W}_{ideal}$ were considerably smaller than the cycle heat flows, attributable to a high cycle ΔT and gas separation irreversibilities, and produced low η compared to similar cycles for electricity production [19, 60].
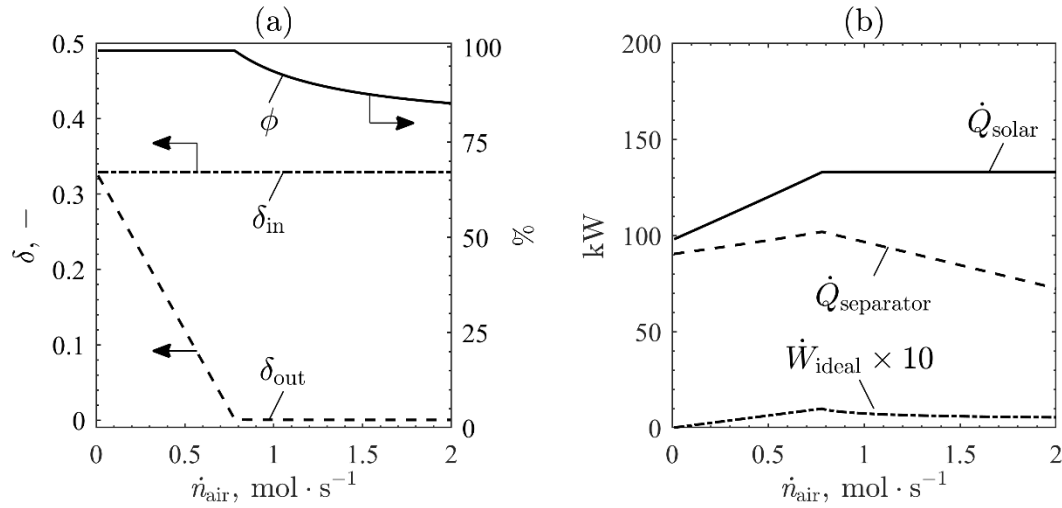
Figure 7.10. For an atmospheric air separation cycle with a solar reactor temperature of 1073 K and a SrFeO$_{3-\delta}$ air separator exit temperature of 298 K, as functions of molar air flow rate: (a) nonstoichiometry at the air separator inlet and outlet and the resulting N$_2$ purity; (b) solar input and air separator waste heat compared to the power input for a reversible air separation process.

The η consistently peaked just prior to the drop in φ, as shown for the non-recuperative ($\dot{Q}_{separator} = 0$) cycle in Figure 7.11 for varying a) $T_{reactor}$ and b) $T_{separator}$, respectively. Increases in $T_{reactor}$ expanded the $\dot{n}_{air}$ range of high-φ N$_2$ production and the increased the $\dot{n}_{air}$ of maximum η. However, they were accompanied by eventual decreases in η due to greater re-radiative losses from the solar reactor. Increases in $T_{separator}$,

potentially necessary to overcome air separation kinetic limitations, decreased the high-φ

$\dot{n}_{air}$ range due to a smaller $\Delta\delta$ between the solar reactor and air separator.
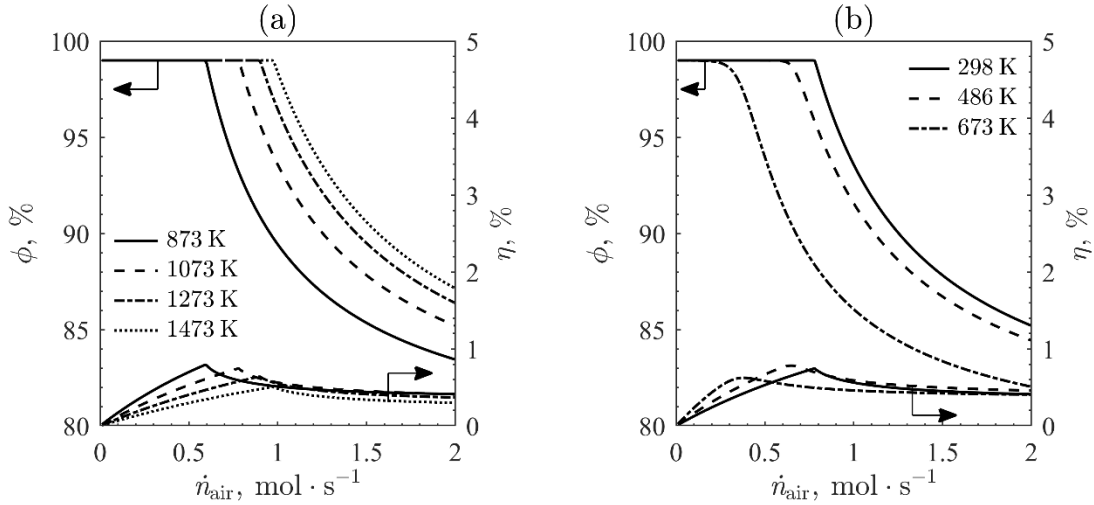
Figure 7.11. For an atmospheric air separation cycle without heat recuperation, N_2 purity and cycle efficiency as functions of molar air flow rate for: a) solar reactor temperatures between 873 and 1473 K and a $SrFeO_{3-\delta}$ air separator exit temperature of 298 K; (b) a solar reactor temperature of 1073 K and $SrFeO_{3-\delta}$ air separator exit temperatures between 298 and 673 K.

As shown in Figure 7.12a, lowering the solar reactor p_{O_2} via vacuum pumping

expanded the $\dot{n}_{air}$ range of high-φ N_2 production while slightly increasing η, despite the

$\dot{W}_{vac}$ penalty. This was due to higher $\Delta\delta$ from greater reduction in the solar reactor, as

shown in Figure 7.12b. $\dot{W}_{vac}$ was low relative to the other energy balance components and

plateaued after reaching sufficient $\dot{n}_{air}$, after which the $SrAl_yFe_{1-y}O_{3-\delta}$ did not oxidize

further in the air separator.
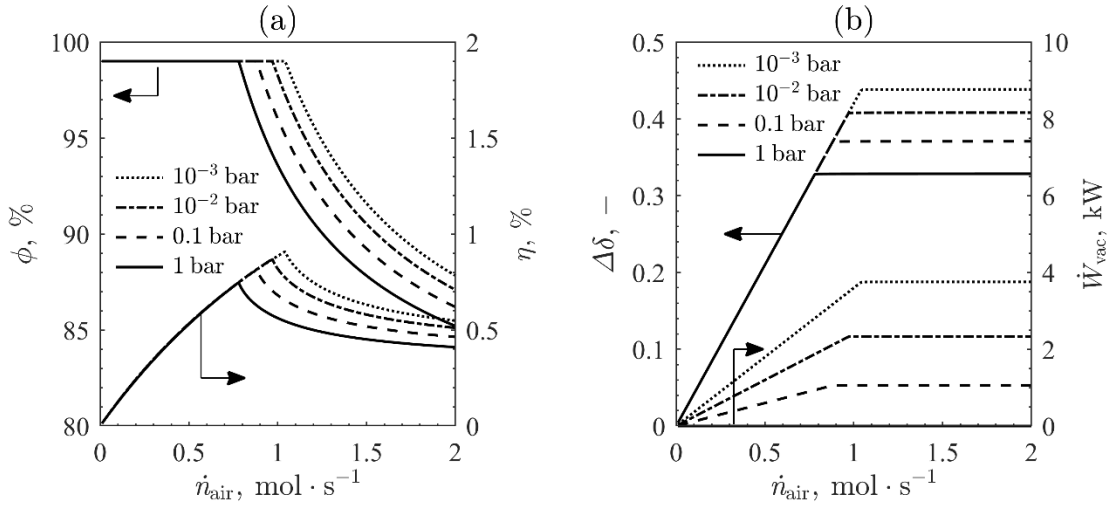
Figure 7.12. For an atmospheric air separation cycle with a solar reactor temperature of 1073 K and pressures of 1, 0.1, 0.01, and 0.001 bar, and a $SrFeO_{3-\delta}$ air separator exit temperature of 298 K, as functions of molar air flow rate: (a) N_2 purity and cycle efficiency (b) total cycle nonstoichiometry range and vacuum pump input power.

Similar cycle trends for $SrAl_yFe_{1-y}O_{3-\delta}$ compared to $SrFeO_{3-\delta}$ were observed, along with a consistently reduced capacity for N_2 production due to smaller attainable $\Delta\delta$. The relationship between η and φ for $y = 0$ and $y = 0.20$ is summarized in Figure 7.13 for a fixed $T_{reactor} = 1073$ K and $T_{separator} = T_0$. For all concentrations, η increased with φ due to greater required $\dot{W}_{ideal}$ for more-complete gas separation. Doping slightly but monotonically lowered the predicted cycle performance with increasing y. A recuperation stage significantly increased η at higher φ. The recuperative and non-recuperative η converged at low $\varphi \ll 0.90$, as more heat was removed by the product stream and $\dot{Q}_{separator}$ approached zero.
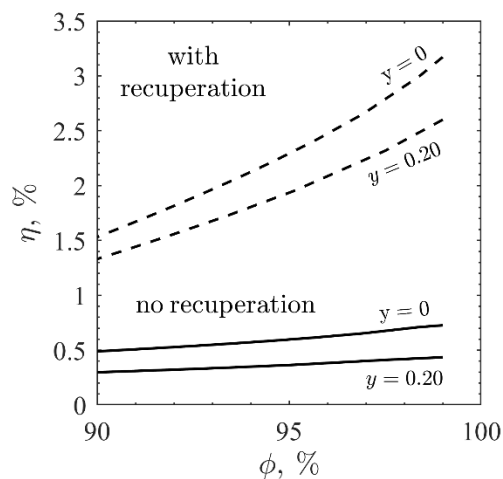
Figure 7.13. Cycle efficiency compared to N_2 purity for an atmospheric air separation cycle with a solar reactor temperature of 1073 K and a $SrAl_yFe_{1-y}O_{3-\delta}$ air separator exit temperature of 298 K, for Al-dopant concentrations of 0, 0.05, 0.10, and 0.15.

7.6   Conclusions

Strontium ferrite perovskite oxides with aluminum dopant concentrations of 0 to 20% were synthesized using a sol-gel method, as confirmed by x-ray powder diffraction. The compound energy formalism was used to successfully predict sample nonstoichiometry across a range of temperatures, O_2 pressures, and dopant concentrations, and the excess entropy components were determined to be highly important in capturing the redox behavior of the oxides. Aluminum doping produced modest increases in the redox enthalpy and limited the range of attainable nonstoichiometries. Redox cycling in upward flow reactor rapidly heated by a high flux solar simulator revealed no systematic decline in redox capacity over ten cycles. Using the determined nonstoichiometry-specific partial enthalpies of reaction, a thermodynamic analysis confirmed the production of high-purity N_2, nearing the maximum concentration of 99% with increasing cycle efficiency at

136

defined molar air flow rates. Vacuum pumping in the solar reactor slightly increased high-purity N_2 output and the overall cycle efficiency due to greater thermal reduction extents.

The compound energy formalism model was integral for capturing the redox equilibria and represents an important step in modeling perovskite oxides in which complicated defect behavior aren't fully captured by ideal solution models. The inverse relationship between N_2 yield and efficiency determined by the thermodynamic cycle analysis is an indication that the design of a real process may not necessarily pursue a thermodynamic optimum, but instead may be based on desired N_2 purities, production rates, and acceptable efficiency levels as they relate to economics and scale.

CHAPTER 8. RESEARCH IMPACTS AND FUTURE WORK

8.1   Research Impacts

The impacts of this research include: rigorous characterization and mapping of radiation from a high-flux solar simulator to computational reactor models, the development of an upward flow reactor capable of studying rapid, on-sun thermal reduction reactions and high reduction temperatures, and the successful spatial, temporal modeling of on-sun experimental temperatures of a reducing binary metal oxide using the instrument. Furthermore, binary Fe_2O_3/Fe_3O_4 oxides were demonstrated to achieve thermochemical energy storage comparable with the less benign, less economical Co_3O_4/CoO binary pair at high concentration ratios, and to undergo rapid thermal reduction and oxidation reactions. Finally, Al-doped $SrFeO_{3-\delta}$ oxides were successfully synthesized and thermodynamic models were developed that predicted redox extent as a function of temperature, pressure, and dopant concentration. The materials were analyzed in a thermodynamic cycle analysis for air separation, and they were shown to be viable for high-purity N_2 production. Cycling experiments in the upward flow reactor were performed to demonstrate rapid, repeatable thermal reduction reactions, with high nonstoichiometries achieved in less than 30 s.

While a variety of methods have been used in the characterization of high flux solar simulators, in this work the correction for a variety of image acquisition errors in flux mapping was robustly performed, including corrections for camera lens distortion, off-centering brightness loss, and perspective distortion due to off-normal viewing angle. While these errors are considerations in a variety of photographic methods for

concentrating solar power, they typically were neglected in flux mapping applications, and specifically flux mapping in high flux solar simulators.

The detailed accounting for a variety of types of spatial variation in the modeling and validation of the upward flow reactor was an improvement on the approximations made in other works. The directional Monte Carlo input to computational heat and mass transfer models was performed in a way which not only preserved the spatial and directional nature of incoming radiation to within mesh precision, but also maintained energy conservation to within machine precision. The generalized ray sorting algorithm and boundary source method allowed the implementation of realistic boundary conditions on unstructured meshes for 2D and 3D absorption. Typical previous methods either relied on surface-averaging of irradiation profiles, which introduces significant inaccuracies in many reactor designs, or spatial interpolation, which fails to maintain energy conservation.

The computational heat and mass transfer model showed that large temperature gradients were present in the reacting sample, and that kinetic analyses, when necessary, should account for such spatial variation. The temporal variation of sample temperature was shown to be bounded by the computational model at all timesteps, an important prerequisite for analyzing the temporal behavior of thermal reduction reactions.

The use of the compound energy formalism in predicting nonstoichiometry, thermodynamic parameters, and thereby the thermochemical energy consumption and production in solar applications was an improvement over previous methods. The compound energy formalism is less restrictive than lattice defect models, allowing for a

wider range of thermodynamic conditions, and was successful in predicting nonstoichiometry and thermodynamic properties as a function of dopant concentration.

8.2   Future Work

The high flux solar simulator-coupled upward flow reactor demonstrated the rapid reaction rates of the perovskite oxides studied in this thesis, and revealed evidence suggesting heating rate rather than chemical limitations in the reactions. This was a welcome result and suggested the materials would be appealing for incorporation into solar receivers/reactors. However, the upward flow reactor is well-suited to analyzing materials with other kinetic limitations and could be used for the following tasks:

- On-sun validation of reduction kinetics models developed by thermogravimetric methods for metal oxides such as Co_3O_4/CoO and Fe_3O_4/Fe_2O_3 (Chapter 6) via solar thermal reduction experiments, followed by coupling model equations to the computational heat transfer and fluid dynamics model (Chapter 5) and calculating molar O_2 flow rates exiting the reactor.

- Development of kinetic models for high temperature ranges unattainable in thermogravimetric instruments, due to low maximum heating rates during nonisothermal experiments and/or gas changeover transients during isothermal experiments.

The thermal reduction kinetics of Fe_2O_3 were determined for a wide range of temperatures and O_2 partial pressures via thermogravimetry (Chapter 6). Furthermore, the oxidation of Fe_3O_4 to Fe_2O_3 with O_2 was shown to proceed rapidly even at moderate temperatures. However, the discovery of multiple reaction rate peaks and therefore a high

likelihood of multiple kinetic regimes confounded kinetic modeling for the early conversion extents. It is likely that some combination of diffusion-limited (for oxidation prior to the maghemite → hematite crystalline phase change) and nucleation-limited (during the crystalline phase change) mechanisms could describe the reaction. More experimentation would be required, however, to ensure that meaningful models were determined and were not simply an exercise in curve fitting with the greater degrees-of-freedom afforded by sequential or parallel models. The following work would likely be necessary for the successful kinetic modeling:

- Reactions performed at a wider range of temperatures and O_2 partial pressures, to determine whether consistent evidence of a two-regime process can be found.
- A systematic study of the influence of reaction rate and starting temperature on the location of the two reaction rate peaks, to determine whether a predictive expression can be developed.
- Nonlinear fitting of parallel models to allow for the gradual transition between limiting mechanisms, if determined necessary.

Finally, the compound energy formalism was found to be a powerful method for predicting the redox behavior not just of single perovskite compositions, but of doped perovskites as a function of dopant concentration alongside temperature and O_2 partial pressure. The successful application of the formalism to a non-labile dopant such as aluminum is a good foundation for future use of compound energy models for labile dopants which undergo sequential or parallel reduction and oxidation with the primary B-cation. The model could be extended to capture labile dopant reduction and oxidation, assuming sufficient data could be gathered.

A key advantage of the compound energy formalism is the ability of the method to incorporate large amounts of experimental data, from different sources and with multiple types of physical measurements. Indeed, the works cited in this thesis make use of a variety of literature resources in the development of thermodynamic models. This is most feasibly done using commercial or open source software diagrams that perform calculation of phase diagrams (CALPHAD) modeling (*e.g.* Thermo-Calc^{TM}). Therefore, a longer-term improvement of the thermodynamic models would be the incorporation of other studies of strontium ferrite, starting with those cited in this thesis, for the purposes of further validating the experimental measurements obtained here and improving the quality of the semi-empirical fitted terms in the model.

APPENDIX A. MAPPING MCRT SURFACE/VOLUME PROFILES

IN ANSYS FLUENT

The below procedure details the method of mapping MCRT surface irradiation to ANSYS Fluent v19.0. The example files and directions have been tested and confirmed compatible for both serial and parallel operation at float or double precision from within the ANSYS Workbench environment. In the provided form, the example files are only compatible with a single coupled surface in Fluent. However, the files are constructed in such a way that extension to two or more surfaces is possible with trivial modifications, and lines of code provided as comments demonstrate how to do so.

Steps:

1. Reserve user-defined memory (UDM) locations for storing incident rays via **User Defined > Memory > Number of User-Defined Memory Locations: [1]**.
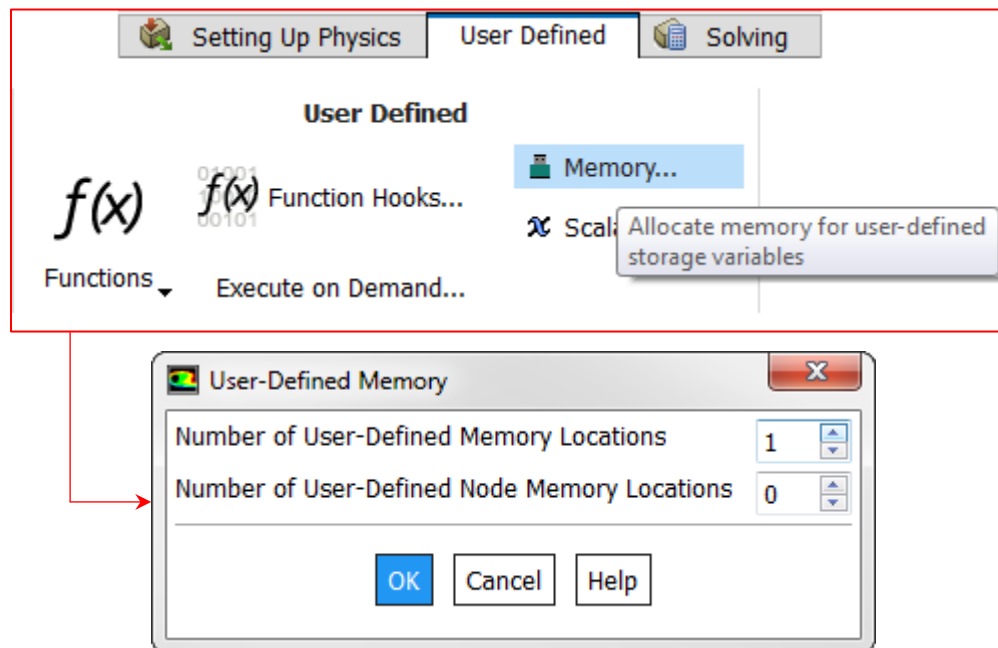
2. Load, compile .c and .h files for UDF via **User Defined > Functions > Compiled >**

    a. (Source Files) Add > [coupleMCRT.c]

    b. (Header Files) Add > [coupleHeader.h]

    c. [Build]

    d. [Load]
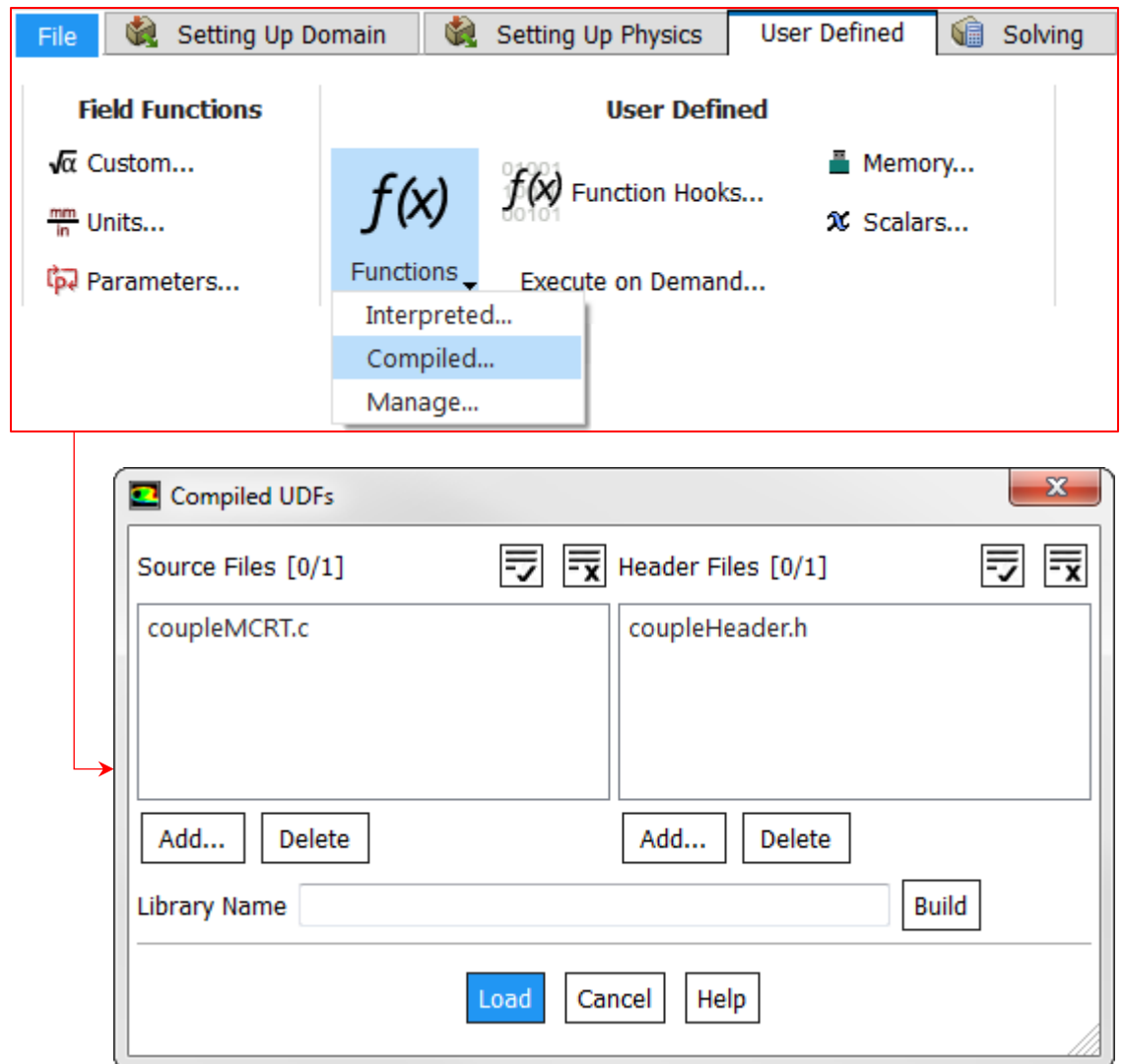
3. Integrate the MCRT-CFD mapping procedure into the solution initialization feature as a function hook, via: **User Defined > Function Hooks > (Initialization) Edit: [import_MCRT::libudf] >**

   a. [Add]

   b. [OK]
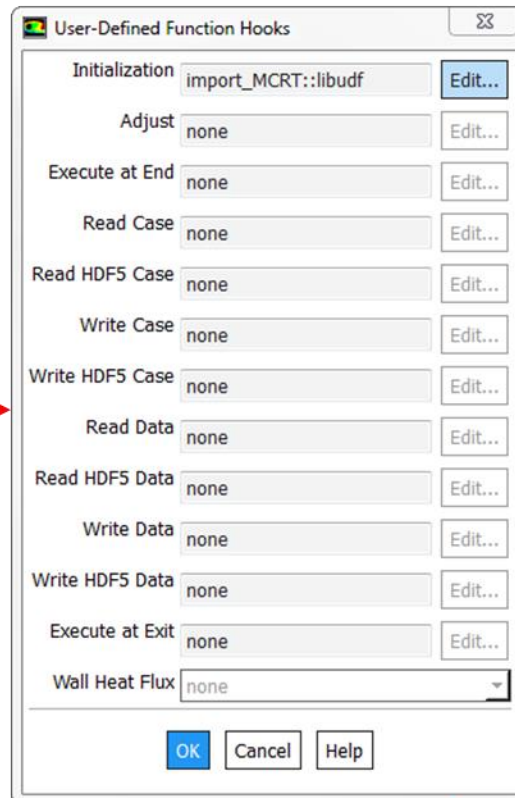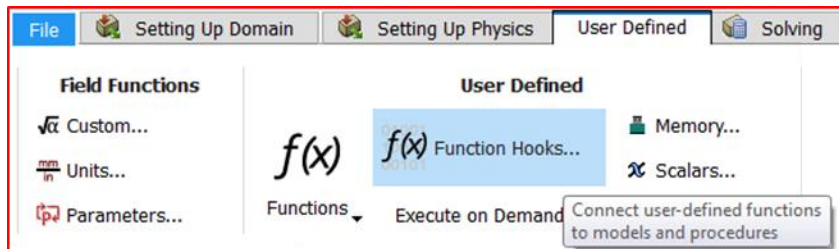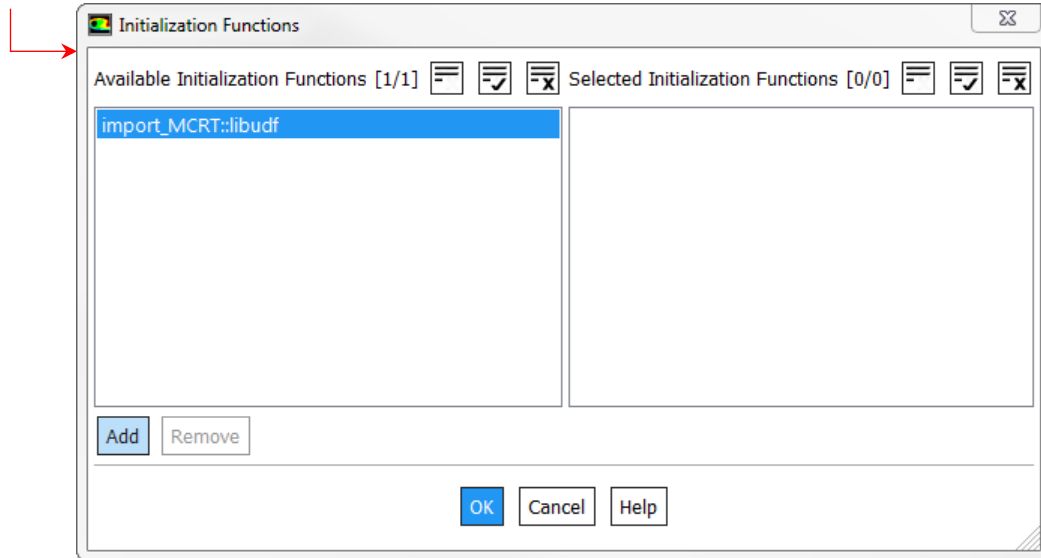
4. Couple the power from incident rays to the thermal energy equation via volumetric boundary source terms, with a boundary thickness defined in the **coupleHeader.h** header file, via **Setup > Boundary Conditions > [irradiated boundary] > Thermal > Heat Generation Rate (W/m3) > [udf absorbed_irradiation::libudf]**.
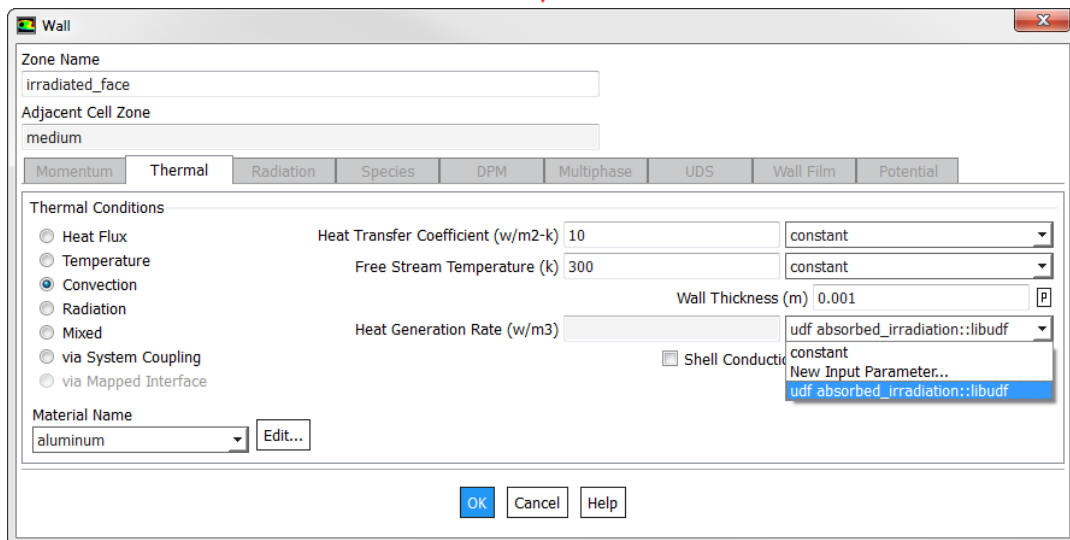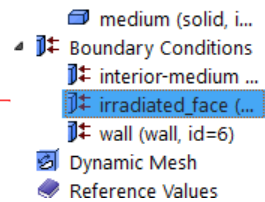
For volumetric mapping (*i.e.* a volumetric source term), the source would instead be included via **Setup > Cell Zone Conditions > [absorbing volume] > Source Terms > Energy > [udf absorbed_radiation_cell::libudf]**, with the Source Terms box checked and the Number of Energy Sources set to [1].

Monte Carlo irradiation data for each surface should be in the form of a space-separated ASCII text file of N lines, where N is the number of ray intersections, and where each line is four decimal numbers long:

$$x_1 \ y_1 \ z_1 \ E_1$$
$$x_2 \ y_2 \ z_2 \ E_2$$
$$\vdots \ \ \vdots \ \ \vdots \ \ \vdots$$
$$x_N \ y_N \ z_N \ E_N$$

The file should have neither header nor footer and lines should be generated by a single newline character ("\n"), or manually with the Enter key. The spatial coordinates x_k, y_k, and z_k should be in units of [m] and E_k in units of [W].

The following files necessary for implementation of the ray mapping procedure in ANSYS Fluent as compiled UDFs may be found in Appendix B:

coupleMCRT.m

coupleHeader.h

APPENDIX B. USER-DEFINED C FUNCTION FOR MCRT-CFD

MAPPING

coupleMCRT.m

```c
#include "udf.h"

#include <stdio.h>
#include <stdlib.h>
#include <math.h>

#include "coupleHeader.h"


// Function used to import and map volumetric/surface Monte Carlo results files to user-defined memory
//  locations at specific cells/faces each time the solution is initialized. Can be modified to a
//  DEFINE_ON_DEMAND macro if preferred.
DEFINE_INIT(import_MCRT,d)
{

// Procedure for coupling one Monte Carlo results file to one model surface/volume. Commented lines
//  demonstrate how to couple up to N results files and surfaces/volumes.


    char rayPathSurf[34] = "C:\\Model\\MCRT_Example_Surface.txt";
    char rayPathVol[33] = "C:\\Model\\MCRT_Example_Volume.txt";
    //                      .
    //                      .
    //                      .
    // char rayPathN[27] = "C:\\Model\\MCRT_ExampleN.txt";


    importMCRT(rayPathSurf,COUPLED_SURFACE_ID,0); // 0 indicates surface coupling
    // importMCRT(rayPath2,COUPLED_SURFACE2_ID,0);
    //                      .
    //                      .
    //                      .
    // importMCRT(rayPathN,COUPLED_SURFACEN_ID,0);


    importMCRT(rayPathVol,COUPLED_VOLUME_ID,1); // 1 indicates volume coupling
    // importMCRT(rayPath2,COUPLED_VOLUME2_ID,1);
    //                      .
    //                      .
    //                      .
    // importMCRT(rayPathN,COUPLED_VOLUMEN_ID,1);

}
```

```c
// Function used to couple surface-absorbed Monte Carlo rays saved in user-defined memory to a boundary
//   source.
DEFINE_PROFILE(absorbed_irradiation_face,t,i)
{

    face_t f;

    real boundaryVolume;
    real faceArea;

    real NV_VEC(faceAreaVec);


    begin_f_loop_int(f,t) {

        F_AREA(faceAreaVec,f,t);
        faceArea = NV_MAG(faceAreaVec);
        boundaryVolume = faceArea * WALL_THICKNESS;

        F_PROFILE(f,t,i) = F_UDMI(f,t,0) / boundaryVolume;

    } end_f_loop_int(f,t)
}


// Function used to couple volumetrically-absorbed Monte Carlo rays saved in user-defined memory to a
//   volumetric source.
DEFINE_SOURCE(absorbed_radiation_cell,c,t,dS,eqn)
{

    real cellVolume;
    real source;

    cellVolume = C_VOLUME(c,t);

    source = C_UDMI(c,t,0) / cellVolume;

    dS[eqn] = 0.0;

    return source;

}


void importMCRT(char *rayPath,int threadID,int volThread) {

    FILE *fID;

    real *Ek;
    real *rk;
    real tPow;

    int clSt;
    int flag;
    int go;
    int k;
    int N;
    int nSortedRays;

    char buff[40];

    flag = 0;
    nodesync(flag);
```

```
#if !RP_NODE
    // Open MCRT file and count number of rays.
    Message("\n\n------------------------\n\nLoading MCRT ray file from:\n\n%s\n\n",rayPath);
    fopen_s(&fID,rayPath,"r");
    Message("DONE\n\n");

    go = 1; N = 0;
    while ( fgets(buff,40,fID) != NULL ) {
        ++N;
    }
    Message("%d rays in file\n\n",N);

#endif


// Read file data into intersection location and energy packet arrays.
host_to_node_int_1(N);
rk = (real*) calloc(N * 3, sizeof(real) );
Ek = (real*) calloc(N, sizeof(real) );


#if !RP_NODE

    // Rewind MCRT file to beginning and read in rays.
    rewind(fID);

    Message("Attempting to read in rays ... ");
    for ( k = 0; k < N; ++k ) {
        if ( sizeof(real) == sizeof(double) ) {
            fscanf_s(fID,"%lf %lf %lf %lf\n",&rk[k],&rk[k + N],&rk[k + 2*N],&Ek[k]);
        } else if ( sizeof(real) == sizeof(float) ) {
            fscanf_s(fID,"%f %f %f %f\n",&rk[k],&rk[k + N],&rk[k + 2*N],&Ek[k]);
        }
    }
    Message("DONE.\n\n");


    // Close file.
    Message("Closing file ... ");
    clSt = fclose(fID);
    if ( clSt ) {
        Message("\n\nERROR ON CLOSE OF DATA FILE. Press any button to continue.\n\n."); getchar();
        exit(0);
    }
    else {
        Message("DONE\n\n");
    }

#endif

host_to_node_real(rk,3*N);
host_to_node_real(Ek,N);

nodesync(flag);


// Call ray sorting routine.
#if !RP_NODE
    if ( volThread ) {
        Message("Attempting to sort rays into cells of volume with zone ID %d ... ",threadID);
    } else {
        Message("Attempting to sort rays into faces of surface with zone ID %d ... ",threadID);
    }
#endif
```

150

```c
    nSortedRays = 0; tPow = 0;
    #if !RP_HOST
        if ( volThread ) {
            coupleVolumeMCRT(&tPow,&nSortedRays,rk,Ek,threadID,N);
        } else {
            coupleSurfaceMCRT(&tPow,&nSortedRays,rk,Ek,threadID,N);
        }
    #endif

    free(rk);
    free(Ek);

    nodesync(flag);

    node_to_host_real_1(tPow);
    node_to_host_int_1(nSortedRays);

    #if !RP_NODE
        Message("DONE.\n\n");
        Message("%d of %d rays were sorted, for a total power of %lf [W]\n ",nSortedRays,N,tPow);
        Message(\n-------------------------------------------------------------------\n\n");

    #endif

}


int nodesync(int flag) {

    #if !RP_HOST

        ++flag;

    #endif

    PRF_GSYNC();
    node_to_host_int_1(flag);

    return flag;

}


void coupleSurfaceMCRT(real *tPowOut, int *nSortedRaysOut, real *r,real *E,int faceID,int N) {

    // Variable Name    Description                                         Size
    // ---------------------------------------------------------------------------
    // r                Monte Carlo intersection coordinates per ray     [Nx3]
    // E                Monte Carlo ray energies array                   [Nx1]
    // faceID               Fluent face ID                                   [1x1]
    // N                Number of Monte Carlo rays                       [1x1]


    Domain *d;
    Thread *t;
    Node *v;

    face_t f;

    int k;
    int n;
    int faceType;
    int nFaces;
    int nSortedRays;
    int withinFace;
```

```c
    real pow;
    real tPow;

    real xN[4];
    real yN[4];
    real zN[4];

    real P[3];

    real *usedRay = (real*) calloc(N,sizeof(real));


    // Get identifying information about coupled surface.
    d = Get_Domain(1);
    t = Lookup_Thread(d,faceID);
    nFaces = THREAD_N_ELEMENTS_INT(t);


    // Loop over all faces.
    nSortedRays = 0; tPow = 0;
    begin_f_loop_int(f,t) {


        // Obtain vertices of current face element and determine whether it is triangular or
        //  quadrilateral.
        faceType = F_NNODES(f,t);

        f_node_loop(f,t,n) {
            v = F_NODE(f,t,n);
            xN[n] = NODE_X(v);
            yN[n] = NODE_Y(v);
            zN[n] = NODE_Z(v);
        }


        // Loop over all (unsorted) rays, determining which (if any) fall within current face.
        pow = 0;
        for ( k = 0; k < N; k++ ) {

            if ( !usedRay[k] ) {

                P[0] = *(r + k);
                P[1] = *(r + k + N);
                P[2] = *(r + k + 2*N);

                if ( faceType == 3 ) {
                    withinFace = point_in_triangle(xN,yN,zN,P);
                } else if ( faceType == 4 ) {
                    withinFace = point_in_quadrilateral(xN,yN,zN,P);
                }


                // Calculate total power on face.
                pow = pow + *(E + k) * withinFace;


                // If a ray is sorted into a face, remove it from consideration for future faces.
                if ( withinFace ) {
                    usedRay[k] = 1;
                    ++nSortedRays;
                }
            }
        }
    }
```

```
        // Calculate total power on surface (all faces).
        tPow = tPow + pow;


        // Place summed ray powers into user-defined memory for access by DEFINE_PROFILE().
        F_UDMI(f,t,0) = pow;

    } end_f_loop_int(f,t)

    nSortedRays = PRF_GISUM1(nSortedRays); tPow = PRF_GRSUM1(tPow);

    *nSortedRaysOut = nSortedRays;
    *tPowOut = tPow;

}


void coupleVolumeMCRT(real *tPowOut, int *nSortedRaysOut, real *r,real *E,int cellID,int N) {

    // Variable Name    Description                                              Size
    // ------------------------------------------------------------------------------
    // r                Monte Carlo intersection coordinates per ray      [Nx3]
    // E                Monte Carlo ray energies array                    [Nx1]
    // cellID           Fluent cell ID                                    [1x1]
    // N                Number of Monte Carlo rays                        [1x1]


    Domain *d;
    Thread *t;
    Node *v;

    cell_t c;

    int k;
    int n;
    int cellType;
    int nCells;
    int nNodes;
    int nSortedRays;
    int withinCell;

    real pow;
    real tPow;

    real xN[8];
    real yN[8];
    real zN[8];

    real P[3];

    real *usedRay = (real*) calloc(N,sizeof(real));


    // Get identifying information about coupled volume.
    d = Get_Domain(1);
    t = Lookup_Thread(d,cellID);
    nCells = THREAD_N_ELEMENTS_INT(t);
```

```c
    // Loop over all cells.
    nSortedRays = 0; tPow = 0;
    begin_c_loop_int(c,t) {


        // Obtain vertices of current cell element and determine whether it is tetrahedral or hexahedral.
        cellType = C_NFACES(c,t);
        nNodes = C_NNODES(c,t);

        c_node_loop(c,t,n) {
            v = C_NODE(c,t,n);
            xN[n] = NODE_X(v);
            yN[n] = NODE_Y(v);
            zN[n] = NODE_Z(v);
        }


        // Loop over all (unsorted) rays, determining which (if any) fall within current cell.
        pow = 0;
        for ( k = 0; k < N; k++ ) {
            if ( !usedRay[k] ) {

                P[0] = *(r + k);
                P[1] = *(r + k + N);
                P[2] = *(r + k + 2*N);

                if ( cellType == 4 ) {
                    withinCell = point_in_tetrahedron(xN,yN,zN,P);
                } else if ( cellType > 4 ) {
                    withinCell = point_in_polyhedron(xN,yN,zN,P,nNodes);
                }


                // Calculate total power on cell.
                pow = pow + *(E + k) * withinCell;


                // If a ray is sorted into a cell, remove it from consideration for future cells.
                if ( withinCell ) {
                    usedRay[k] = 1;
                    ++nSortedRays;
                }
            }
        }


        // Calculate total power in a volume (all cells).
        tPow = tPow + pow;


        // Place summed ray powers into user-defined memory for access by DEFINE_PROFILE().
        C_UDMI(c,t,0) = pow;

    } end_c_loop_int(c,t)

    nSortedRays = PRF_GISUM1(nSortedRays); tPow = PRF_GRSUM1(tPow);

    *nSortedRaysOut = nSortedRays;
    *tPowOut = tPow;

}
```

```
int point_in_triangle(real x[],real y[],real z[],real P[]) {

    int i;
    int inside;

    real di1;
    real di2;
    real dp1;
    real dp2;

    real ds;

    real D;
    real n;
    real s;

    real u;
    real v;

    real Q[3];

    real vN[3];
    real nN[3];

    real vAB[3];
    real vAC[3];
    real vAP[3];
    real vAQ[3];


    // Create vectors from arbitrary anchoring vertex of triangle (A) to other vertices and to point being
    //  tested.
    vAB[0] = x[1] - x[0];
    vAB[1] = y[1] - y[0];
    vAB[2] = z[1] - z[0];

    vAC[0] = x[2] - x[0];
    vAC[1] = y[2] - y[0];
    vAC[2] = z[2] - z[0];

    vAP[0] = P[0] - x[0];
    vAP[1] = P[1] - y[0];
    vAP[2] = P[2] - z[0];


    // Compute normal vector of triangular face.
    vN[0] = vAB[1] * vAC[2] - vAB[2] * vAC[1];
    vN[1] = vAB[2] * vAC[0] - vAB[0] * vAC[2];
    vN[2] = vAB[0] * vAC[1] - vAB[1] * vAC[0];

    n = sqrt(norm(vN,3));

    for ( i = 0; i < 3; i++ ) {
        nN[i] = vN[i] / n;
    }

    // Project point into plane of triangular face.
    s = dot(vAP,nN,3);

    for ( i = 0; i < 3; i++ ) {
        Q[i] = P[i] - s * nN[i];
    }


    // Create vector from arbitrary anchoring vertex of triangle (A) to projected point being tested.
    vAQ[0] = Q[0] - x[0];
    vAQ[1] = Q[1] - y[0];
    vAQ[2] = Q[2] - z[0];
```

```
    // Compute all needed dot product combinations for three vectors.
    dp1 = dot(vAQ,vAB,3);
    dp2 = dot(vAQ,vAC,3);
    ds  = dot(vAB,vAC,3);
    di1 = dot(vAB,vAB,3);
    di2 = dot(vAC,vAC,3);


    // Compute denominator of constants used to define location of point in barycentric coordinate system.
    D = ds * ds - di1 * di2;


    // Create constants (scalar multiples of basis pair vAB and vAC).
    u = (dp2 * ds - dp1 * di2) / D;
    v = (dp1 * ds - dp2 * di1) / D;


    // Test to see whether constants are positive and sum to less than one (requirement for interior
    //  point).
    inside = 0;
    if (u > 0. && v > 0. && u + v < 1. && s < (sqrt(norm(vAB,3))+sqrt(norm(vAC,3))) && fabs(D) > 1e-20) {
        inside = 1;
    }

    return inside;
}


int point_in_quadrilateral(real x[],real y[],real z[],real P[]) {


    int inside;
    int inTri;
    int sum;

    real xTri[3];
    real yTri[3];
    real zTri[3];

    size_t i;
    size_t n = 4;


    // Create virtual triangles between every combination of three points and run point-in-triangle
    //  routine for each.
    inside = 0;
    for (i = 0; i < n; ++i) {

        xTri[0] = x[i%n];
        xTri[1] = x[(i+1)%n];
        xTri[2] = x[(i+2)%n];

        yTri[0] = y[i%n];
        yTri[1] = y[(i+1)%n];
        yTri[2] = y[(i+2)%n];

        zTri[0] = z[i%n];
        zTri[1] = z[(i+1)%n];
        zTri[2] = z[(i+2)%n];

        inTri = point_in_triangle(xTri,yTri,zTri,P);
```

```
            // If ray intersection is found to be within any virtual triangles, declare the point inside the
            //  quadrilateral face.
            if ( inTri ) {
                inside = 1;
                i = n;
            }

        }

        return inside;
}


int point_in_tetrahedron(real x[],real y[],real z[],real P[]) {


    int inside;

    real di1;
    real di2;
    real di3;

    real dp1;
    real dp2;
    real dp3;

    real ds1;
    real ds2;
    real ds3;

    real Du;
    real Dv;
    real Dw;

    real Nu;
    real Nv;
    real Nw;

    real u;
    real v;
    real w;

    real vAB[3];
    real vAC[3];
    real vAD[3];
    real vAP[3];


    // Create vectors from arbitrary anchoring vertex of triangle (A) to other vertices and point being
    //  tested.
    vAB[0] = x[1] - x[0];
    vAB[1] = y[1] - y[0];
    vAB[2] = z[1] - z[0];

    vAC[0] = x[2] - x[0];
    vAC[1] = y[2] - y[0];
    vAC[2] = z[2] - z[0];

    vAD[0] = x[3] - x[0];
    vAD[1] = y[3] - y[0];
    vAD[2] = z[3] - z[0];

    vAP[0] = P[0] - x[0];
    vAP[1] = P[1] - y[0];
    vAP[2] = P[2] - z[0];
```

```
    // Compute all needed dot product combinations for four vectors.
    dp1 = dot(vAP,vAB,3);
    dp2 = dot(vAP,vAC,3);
    dp3 = dot(vAP,vAD,3);
    ds1 = dot(vAB,vAC,3);
    ds2 = dot(vAB,vAD,3);
    ds3 = dot(vAC,vAD,3);
    di1 = dot(vAB,vAB,3);
    di2 = dot(vAC,vAC,3);
    di3 = dot(vAD,vAD,3);


    // Create constants (scalar multiples of bases vAB, vAC, and vAD) used to define location of point in
    //  barycentric coordinate system.
    Nu = (dp1*di2 - dp2*ds1) * (ds3*ds3 - di2*di3) - (dp2*ds3 - dp3*di2) * (ds2*di2 - ds1*ds3);
    Du = (di1*di2 - ds1*ds1) * (ds3*ds3 - di2*di3) - (ds1*ds3 - ds2*di2) * (ds2*di2 - ds1*ds3);

    Nv = (dp1*ds3 - dp2*ds2) * (ds1*di3 - ds2*ds3) - (dp2*di3 - dp3*ds3) * (di1*ds3 - ds1*ds2);
    Dv = (ds1*ds3 - di2*ds2) * (ds1*di3 - ds2*ds3) - (di2*di3 - ds3*ds3) * (di1*ds3 - ds1*ds2);

    Nw = (dp1*di2 - dp2*ds1) * (ds1*ds3 - ds2*di2) - (dp2*ds3 - dp3*di2) * (di1*di2 - ds1*ds1);
    Dw = (ds2*di2 - ds1*ds3) * (ds1*ds3 - ds2*di2) - (ds3*ds3 - di2*di3) * (di1*di2 - ds1*ds1);

    u = Nu / Du;
    v = Nv / Dv;
    w = Nw / Dw;


    // Test to see whether constants are positive and sum to less than one (requirement for interior
    //  point).
    inside = 0;
    if (u > 0. && v > 0. && w > 0. && u+v+w < 1. && fabs(Du)>1e-20 && fabs(Dv)>1e-20 && fabs(Dw)>1e-20) {
        inside = 1;
    }


    return inside;
}


int point_in_polyhedron(real x[],real y[],real z[],real P[], int n) {


    int inside;
    int inTet;

    real coplanar;
    real D;
    real n01x02;
    real n03;
    real nD;

    real v01[3];
    real v02[3];
    real v03[3];
    real v01x02[3];

    real xTet[4];
    real yTet[4];
    real zTet[4];

    size_t i;
    size_t j;
    size_t k;
    size_t l;
```

```c
// Create virtual tetrahedrons between every combination of four non-coplanar points and run point-in-
//   tetrahedron routine for each.
inside = 0;
for (i = 0; i < n; ++i) {
    for (j = 0; j < n; ++j) {
        for (k = 0; k < n; ++k) {
            for (l = 0; l < n; ++l) {
                if ( i != j && i != k && i != l && j != k && j != l && k != l ) {

                    xTet[0] = x[i];
                    xTet[1] = x[j];
                    xTet[2] = x[k];
                    xTet[3] = x[l];

                    yTet[0] = y[i];
                    yTet[1] = y[j];
                    yTet[2] = y[k];
                    yTet[3] = y[l];

                    zTet[0] = z[i];
                    zTet[1] = z[j];
                    zTet[2] = z[k];
                    zTet[3] = z[l];


                    // Ensure that nodes make tetrahedron rather than quadrilateral.
                    v01[0] = xTet[1] - xTet[0];
                    v01[1] = yTet[1] - yTet[0];
                    v01[2] = zTet[1] - zTet[0];

                    v02[0] = xTet[2] - xTet[0];
                    v02[1] = yTet[2] - yTet[0];
                    v02[2] = zTet[2] - zTet[0];

                    v03[0] = xTet[3] - xTet[0];
                    v03[1] = yTet[3] - yTet[0];
                    v03[2] = zTet[3] - zTet[0];

                    v01x02[0] = v01[1] * v02[2] - v01[2] * v02[1];
                    v01x02[1] = v01[2] * v02[0] - v01[0] * v02[2];
                    v01x02[2] = v01[0] * v02[1] - v01[1] * v02[0];

                    n03 = norm(v03,3);
                    n01x02 = norm(v01x02,3);
                    D = dot(v03,v01x02,3);
                    nD = fabs(D) / (n03 * n01x02);

                    coplanar = nD < 0.01;

                    inTet = 0;
                    if ( !coplanar ) {
                        inTet = point_in_tetrahedron(xTet,yTet,zTet,P);

                    }


                    // If ray intersection is found to be within any virtual tetrahedrons, declare
                    //   the point inside the hexahedron.
                    if ( inTet ) {
                        inside = 1;
                        i = n; j = n; k = n; l = n;
                    }
                }
            }
        }
    }
}
```

```
    return inside;
}


real dot(real x[],real y[],size_t size) {

    real sum;
    size_t i;


    // Calculate dot product of two vectors.
    sum = 0.0;
    for (i = 0; i < size; ++i) {
        sum += x[i] * y[i];
    }

    return sum;
}


real norm(real x[],size_t size) {

    real root;
    real sumSq;
    size_t i;


    // Calculate 2-norm of vector
    sumSq = 0.0;
    for (i = 0; i < size; ++i) {
        sumSq += pow(x[i],2);
    }

    root = sqrt(sumSq);

    return root;
}
```

coupleHeader.h

```c
#ifndef COUPLEHEADER_H
    #define COUPLEHEADER_H

        // Functions
        int nodesync(int flag);
        void importMCRT(char *,int id,int threadType);
        void coupleSurfaceMCRT(real *, int *, real *,real *,int id,int N);
        void coupleVolumeMCRT(real *, int *, real *,real *,int id,int N);
        int point_in_triangle(real x[],real y[],real z[],real P[]);
        int point_in_quadrilateral(real x[],real y[],real z[],real P[]);
        int point_in_tetrahedron(real x[],real y[],real z[],real P[]);
        int point_in_polyhedron(real x[],real y[],real z[],real P[],int n);
        real dot(real x[],real y[],size_t size);
        real norm(real x[],size_t size);

        // Constants
        #define COUPLED_SURFACE_ID 5            // Face ID number of coupled surface
        // #define COUPLED_SURFACE2_ID [#]      // Face ID number of second coupled surface
        // #define COUPLED_SURFACE3_ID [#]      // Face ID number of third coupled surface
        //                  .                                 .
        //                  .                                 .
        //                  .                                 .
        // #define COUPLED_SURFACEN_ID [#]      // Face ID number of nth coupled surface

        #define COUPLED_VOLUME_ID 4            // Face ID number of coupled volume
        // #define COUPLED_VOLUME2_ID [#]       // Face ID number of second coupled volume
        // #define COUPLED_VOLUME3_ID [#]       // Face ID number of third coupled volume
        //                  .                                 .
        //                  .                                 .
        //                  .                                 .
        // #define COUPLED_VOLUMEN_ID [#]       // Face ID number of nth coupled volume

        #define WALL_THICKNESS 0.001           // Thickness [m] used for boundary source calculations

#endif
```

APPENDIX C. COMPOUND ENERGY MODEL DEFINITION

The compound energy formalism (CEF) is a powerful, highly-flexible method for thermodynamically representing solution phases with one or more sublattices. This appendix uses the conventions of a review article on the CEF [78] to derive a thermodynamic model for the perovskite oxides studied in Chapter 7.

The general form of the CEF for a given phase P of a system is given as:

$$G_m^P = \sum_i \left({}^\circ G_{end,i} \prod_{k \in S_i} y_k \right) + RT \sum_m \left(\nu_m \sum_{k \in S_m} y_k \ln y_k \right) + {}^E G_m^P \qquad (C.1)$$

The first term incorporates some representation of the Gibbs free energies of the constituents. This contribution is captured via a surface of reference s.r., the Gibbs free energy of which is defined via end members, or extrema compositions of the system, where each sublattice is wholly occupied by a single constituent rather than a mixture of constituents. The number of end states is dependent of the number of possible unique single-constituent-sublattice forms of the system. The surface of reference is defined as:

$$G_m^{s.r.} = \sum_i \left({}^\circ G_{end,i} \prod_{k \in S_i} y_k \right) \qquad (C.2)$$

where the summation is over the standard Gibbs free energies $^\circ G$ of all end states, each modulated by the product of the constituent site fractions y_k present in the respective end state on each sublattice, or $k \in S_i$.

A system Gibbs free energy will be a function of not only the Gibbs free energies of its components, but also a function of their mixing and interactions due to the entropic component of the Gibbs free energy. If a system can be assumed to have ideal mixing entropy, *i.e.*, mixing of its various constituents is random, and if the temperature is sufficiently high that entropy cannot be neglected, this entropic term is defined as:

$$-S_{\mathrm{m}}^{\mathrm{mix}}T = RT\sum_{\mathrm{m}}\left(\nu_{\mathrm{m}}\sum_{k\in S_{\mathrm{m}}} y_{k}\ln y_{k}\right) \tag{C.3}$$

where the contribution from each sublattice *m* includes terms for all y_{k} in the given sublattice, or $k \in S_{\mathrm{m}}$.

The final term is the excess Gibbs free energy, which is necessary for systems in which the coordination number (CN) varies from site to site. This is true for ideal cubic perovskites, as summarized below:

- A-site cations: 12-fold coordinated by O-site anions, 8-fold coordinated by B-site cations

- B-site cations: 6-fold coordinated by O-site anions, 8-fold coordinated by A-site cations

- O-site anions: 2-fold coordinated by B-site cations, 4-fold coordinated by A-site cations

The excess Gibbs formulation is dependent upon the form of the system in question: the number of sublattices present and the possible constituents that constitute each sublattice. For the general system, the excess Gibbs energy may be formulated as:

$$^{E}G_{m} = \prod_{s} y_{J}^{s} \sum_{B} y_{B}^{t} L_{A,B:D:G:...} + \prod_{s} y_{J}^{s} \sum_{B} \sum_{E} y_{B}^{t} y_{E}^{u} L_{A,B:D,E:G:...} + \cdots \qquad (C.4)$$

where the first and second summations are over each secondary constituent in a first sublattice represented by the stoichiometric parameter t, and the third summation is over a sublattice represented by the stoichiometric parameter u, and so on for an increasing number of sublattices. It should be noted that t and u serve as identifying superscripts for their respective sublattices, rather than power operations. The significance of the letter subscripts is described fully in [78]. As in the end-state definitions, the product terms include one term per sublattice, $e.g.$ for the above definition, $\prod_{s} y_{J}^{s} = y_{A}^{t} y_{D}^{u} y_{G}^{v} \cdots$. Redlich-Kister terms (CITE) are recommended functional forms for L, given as:

$$L_{A,B:D:G:...} = \sum_{n} {}^{n}L_{i}\left(y_{A}^{t} - y_{B}^{t}\right)^{n} \qquad (C.5)$$

where n is the term order, beginning at 0, and L_i is a polynomial of variable order depending on the available data and resulting fit quality. A modeling of the Ce–Y–O system used Redlich-Kister form for two-species and linear yL_i forms for three-species interactions [82].

Below, the compound energy formalism is set up to model thermodynamic equilibrium states for $SrFe_{1-y}Al_yO_{3-\delta}$ (SAF) in the perovskite phase, represented as $(Sr^{2+})(Fe^{4+},Fe^{3+},Al^{3+})(O^{2-},V_O)_3$. The full expression for the Gibbs free energy of SAF in the perovskite phase at one level of δ, assuming the differential form of the Gibbs free energy is to be used for calculations, may be represented relatively as:

$$
G_{SAF}^{P} = \begin{aligned}
&\left[y_{Sr^{2+}} y_{Fe^{4+}} y_{O^{2-}} \, {}^{\circ}G_{Sr^{2+}\,:\,Fe^{4+}\,:\,O^{2-}}^{P} \right] + \ldots \\
&\left[y_{Sr^{2+}} y_{Fe^{4+}} y_{V_O} \, {}^{\circ}G_{Sr^{2+}\,:\,Fe^{4+}\,:\,V_O}^{P} \right] + \ldots \\
&\left[y_{Sr^{2+}} y_{Fe^{3+}} y_{O^{2-}} \, {}^{\circ}G_{Sr^{2+}\,:\,Fe^{3+}\,:\,O^{2-}}^{P} \right] + \ldots \\
&\left[y_{Sr^{2+}} y_{Fe^{3+}} y_{V_O} \, {}^{\circ}G_{Sr^{2+}\,:\,Fe^{3+}\,:\,V_O}^{P} \right] + \ldots \\
&\left[y_{Sr^{2+}} y_{Al^{3+}} y_{O^{2-}} \, {}^{\circ}G_{Sr^{2+}\,:\,Al^{3+}\,:\,O^{2-}}^{P} \right] + \ldots \\
&\left[y_{Sr^{2+}} y_{Al^{3+}} y_{V_O} \, {}^{\circ}G_{Sr^{2+}\,:\,Al^{3+}\,:\,V_O}^{P} \right] + \ldots \\
&RT\left[y_{Sr^{2+}} \ln y_{Sr^{2+}} \right] + \ldots \\
&RT\left[y_{Fe^{4+}} \ln y_{Fe^{4+}} + y_{Fe^{3+}} \ln y_{Fe^{3+}} + y_{Al^{3+}} \ln y_{Al^{3+}} \right] + \ldots \\
&3RT\left[y_{O^{2-}} \ln y_{O^{2-}} + y_{V_O} \ln y_{V_O} \right] + \ldots \\
&{}^{E}G_{SAF}^{P}
\end{aligned}
\tag{C.6}
$$

However, because the site fractions of Sr ions on the SAF A-sublattice remain unity throughout the thermal reduction and oxidation reactions, the relationship simplifies to:

$$
G_{SAF}^{P} = \begin{aligned}
&\left[y_{Fe^{4+}} y_{O^{2-}} \, {}^{\circ}G_{Sr^{2+}\,:\,Fe^{4+}\,:\,O^{2-}}^{P} \right] + \left[y_{Fe^{3+}} y_{O^{2-}} \, {}^{\circ}G_{Sr^{2+}\,:\,Fe^{3+}\,:\,O^{2-}}^{P} \right] + \ldots \\
&\left[y_{Al^{3+}} y_{O^{2-}} \, {}^{\circ}G_{Sr^{2+}\,:\,Al^{3+}\,:\,O^{2-}}^{P} \right] + \left[y_{Fe^{4+}} y_{V_O} \, {}^{\circ}G_{Sr^{2+}\,:\,Fe^{4+}\,:\,V_O}^{P} \right] + \ldots \\
&\left[y_{Fe^{3+}} y_{V_O} \, {}^{\circ}G_{Sr^{2+}\,:\,Fe^{3+}\,:\,V_O}^{P} \right] + \left[y_{Al^{3+}} y_{V_O} \, {}^{\circ}G_{Sr^{2+}\,:\,Al^{3+}\,:\,V_O}^{P} \right] + \ldots \\
&RT\left[y_{Fe^{4+}} \ln y_{Fe^{4+}} + y_{Fe^{3+}} \ln y_{Fe^{3+}} + y_{Al^{3+}} \ln y_{Al^{3+}} \right] + \ldots \\
&3RT\left[y_{O^{2-}} \ln y_{O^{2-}} + y_{V_O} \ln y_{V_O} \right] + {}^{E}G_{SAF}^{P}
\end{aligned}
\tag{C.7}
$$

where it should be noted that the site fraction of non-reducing trivalent Al $y_{Al^{3+}}$ on the Fe sublattice is always equal to y from the chemical formula. The ionic sublattice site fractions are further governed by atomic conservation via:

$$
\sum_{k \in S_m} y_k^m n^m = n^m
\tag{C.8}
$$

where n^m is the number of formula units for the sublattice and which, with the principle of electroneutrality, produces the system of equations:

$$
\begin{aligned}
y_{Sr^{2+}} &= 1, \\
y_{Fe^{4+}} + y_{Fe^{3+}} + y_{Al^{3+}} &= 1, \\
3y_{V_O} + 3y_{O^{2-}} &= 3, \\
2y_{Sr^{2+}} + 3y_{Al^{3+}} + 3y_{Fe^{3+}} + 4y_{Fe^{4+}} &= 6y_{O^{2-}}
\end{aligned}
\tag{C.9}
$$

noting that the nonstoichiometry can be related to the O^{2-} site fraction, $i.e.$:

$$
\delta = 3y_{V_O}
\tag{C.10}
$$

the site fraction coefficients in terms of the experimentally-measured nonstoichiometry may be determined as:

$$
\begin{aligned}
y_{Fe^{4+}} &= 1 - 2\delta, & y_{Sr^{2+}} &= 1, \\
y_{Fe^{3+}} &= 2\delta - y, & y_{O^{2-}} &= 1 - \frac{\delta}{3}, \\
y_{Al^{3+}} &= y, & y_{V_O} &= \frac{\delta}{3}
\end{aligned}
\tag{C.11}
$$

Substituting these values for the site fractions in the overall form produces:

166

$$
G_{SAF}^P = \begin{array}{l}
\left[(1-2\delta)\left(1-\dfrac{\delta}{3}\right){}^\circ G_{Sr^{2+}\,:\,Fe^{4+}:\,O^{2-}}^P\right]+\dots \\[2em]
\left[(2\delta-y)\left(1-\dfrac{\delta}{3}\right){}^\circ G_{Sr^{2+}\,:\,Fe^{3+}:\,O^{2-}}^P\right]+\dots \\[2em]
\left[y\left(1-\dfrac{\delta}{3}\right){}^\circ G_{Sr^{2+}\,:\,Al^{3+}:\,O^{2-}}^P\right]+\dots \\[2em]
\left[\dfrac{\delta}{3}(1-2\delta){}^\circ G_{Sr^{2+}\,:\,Fe^{4+}:\,V_O}^P\right]+\dots \\[2em]
\left[\dfrac{\delta}{3}(2\delta-y){}^\circ G_{Sr^{2+}\,:\,Fe^{3+}:\,V_O}^P\right]+\dots \\[2em]
\left[y\dfrac{\delta}{3}{}^\circ G_{Sr^{2+}\,:\,Al^{3+}:\,V_O}^P\right]+\dots \\[2em]
RT\left[(1-2\delta)\ln(1-2\delta)+(2\delta-y)\ln(2\delta-y)+y\ln y\right]+\dots \\[1em]
3RT\left[\left(1-\dfrac{\delta}{3}\right)\ln\left(1-\dfrac{\delta}{3}\right)+\dfrac{\delta}{3}\ln\dfrac{\delta}{3}\right]+\dots \\[1em]
{}^E G_{SAF}^P
\end{array}
\tag{C.12}
$$

leaving the standard Gibbs free energy of the end states and the excess terms to be determined. The former can be estimated as the sums of the standard Gibbs free energies of well-measured binary metal oxides and a temperature-dependent power series fit of the form:

$$
{}^\circ G_i(T)=\sum_{n=0}^{N}\beta_{(n-1)i}T^{n-1}+\beta_{Ni}T\ln T
\tag{C.13}
$$

where, typically, $N\leq4$ and the $T\ln T$ term is optional. Here, as if often done, the fit equation is limited to a linear form.

The end state standard Gibbs free energies are defined as mixtures of stable binary metal oxides with similar or identical oxidation states as those attained by the metal cations

in the perovskite phase, and the same number of atoms of each ion per formula unit. The following expressions were therefore selected:

$$
{}^{\circ}G^P_{Sr^{2+} \,:\, Fe^{4+}:\, O^{2-}} = {}^{\circ}G_{SrO} + \frac{1}{2}\,{}^{\circ}G_{Fe_2O_3} + \frac{1}{4}\,{}^{\circ}G_{O_2(g)} + {}^{\circ}G_i(T),
$$

$$
{}^{\circ}G^P_{Sr^{2+} \,:\, Fe^{3+}:\, O^{2-}} = {}^{\circ}G_{SrO} + \frac{1}{2}\,{}^{\circ}G_{Fe_2O_3} + \frac{1}{4}\,{}^{\circ}G_{O_2(g)} + {}^{\circ}G_i(T),
$$

$$
{}^{\circ}G^P_{Sr^{2+} \,:\, Al^{3+}:\, O^{2-}} = {}^{\circ}G_{SrO} + \frac{1}{2}\,{}^{\circ}G_{Al_2O_3} + \frac{1}{4}\,{}^{\circ}G_{O_2(g)} + {}^{\circ}G_i(T),
$$

$$
{}^{\circ}G^P_{Sr^{2+} \,:\, Fe^{4+}:\, V_O} = {}^{\circ}G^P_{Sr^{2+} \,:\, Fe^{4+}:\, O^{2-}} - \frac{3}{2}\,{}^{\circ}G_{O_2(g)},
$$

$$
{}^{\circ}G^P_{Sr^{2+} \,:\, Fe^{3+}:\, V_O} = {}^{\circ}G^P_{Sr^{2+} \,:\, Fe^{3+}:\, O^{2-}} - \frac{3}{2}\,{}^{\circ}G_{O_2(g)},
$$

$$
{}^{\circ}G^P_{Sr^{2+} \,:\, Al^{3+}:\, V_O} = {}^{\circ}G^P_{Sr^{2+} \,:\, Al^{3+}:\, O^{2-}} - \frac{3}{2}\,{}^{\circ}G_{O_2(g)}
$$

(C.14)

Where, for the tetravalent Fe end state, the Gibbs free energy of iron (III) oxide Fe_2O_3 was selected instead of iron (IV) oxide FeO_2 because the latter seemingly does not exist in a stable, solid form like the lower-oxide forms and is not as well-characterized. Therefore, the power series fit term alone captured differences between the tetravalent and trivalent iron end states. The binary metal oxide standard Gibbs functions were obtained from the NIST Chemistry WebBook [146] which defines the properties as functions of temperature as:

$$
{}^{\circ}G(T) = H(T) - TS^{\circ}(T),
$$

$$
H(T) - \Delta_f^{\circ}H = +At + B\frac{t^2}{2} + C\frac{t^3}{2} + D\frac{t^4}{2} - \frac{E}{t} + F - H,
$$

$$
S^{\circ}(T) = A\ln t + Bt + C\frac{t^2}{2} + D\frac{t^3}{2} - \frac{E}{2t^2} + G,
$$

$$
t = \frac{T[K]}{1000}
$$

(C.15)

where the constants $A, \ldots, H$ are defined as tabular data over specified temperature ranges.

The excess terms are defined as:

$$
{}^{E}G_{SAF}^{P} =
\begin{aligned}
& y_{Fe^{4+}} y_{O^{2-}} \sum_{n} y_{Fe^{3+}} L^{n}_{Sr^{2+}:\{Fe^{4+},Fe^{3+}\}:O^{2-}} \left(y_{Fe^{4+}} - y_{Fe^{3+}} \right)^{n} + \dots \\[4pt]
& y_{Fe^{4+}} y_{O^{2-}} \sum_{n} y_{Al^{3+}} L^{n}_{Sr^{2+}:\{Fe^{4+},Al^{3+}\}:O^{2-}} \left(y_{Fe^{4+}} - y_{Al^{3+}} \right)^{n} + \dots \\[4pt]
& y_{Fe^{4+}} y_{O^{2-}} \sum_{n} y_{V_O} L^{n}_{Sr^{2+}:Fe^{4+}:\{O^{2-},V_O\}} \left(y_{O^{2-}} - y_{V_O} \right)^{n} + \dots \\[4pt]
& y_{Fe^{4+}} y_{O^{2-}} \sum_{n} y_{Fe^{3+}} y_{Al^{3+}} L^{n}_{Sr^{2+}:\{Fe^{4+},Fe^{3+},Al^{3+}\}:O^{2-}}
\end{aligned}
\qquad (C.16)
$$

where n typically ranges from 0 up to 2, and the empirical L terms are defined as:

$$
L_{i}^{n}(T) = \sum_{v=0}^{N} \beta_{(v-1)i} T^{v-1} + \beta_{Ni} T \ln T \qquad (C.17)
$$

where i is a placeholder for the interaction and where, typically, $N \leq 4$ and the $T\ln T$ term is optional. Often, the equation is limited to a linear or quadratic form and the term order to $N = 1$. Here, $N = 1$ for binary interactions and $N = 2$ for ternary interactions, as in [81, 82].

In general, the total number of terms for the nonlinear fit is determined by fit significance, but also first by the data resolution. Since the binary metal oxide standard Gibbs functions are assumed known, a Gibbs minimization procedure without accounting for sublattice interaction effects on the solid entropy would require anywhere from 6 to 18 fitted parameters assuming linear or 4th order-with-$T\ln T$ forms of L, respectively.

The fit equation relies on the concept of Gibbs energy minimization at the point of equilibrium in a system, where the system is governed by the reaction:

$$
SrFe_{1-y}Al_{y}O_{3-\delta} \rightarrow SrFe_{1-y}Al_{y}O_{3-\delta-\Delta\delta} + \frac{\Delta\delta}{2} O_{2(g)} \qquad (C.18)
$$
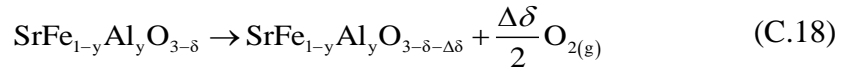
Therefore, the change in Gibbs energy of the system for a reduction at constant temperature and O_2 pressure, per mol SAF at an initial nonstoichiometry δ, may be described as:

$$\Delta G_{\mathrm{SrFe_{1-y}Al_yO_{3-\delta} \rightarrow SrFe_{1-y}Al_yO_{3-\delta-\Delta\delta} + \frac{\Delta\delta}{2}O_{2(g)}}} = \ldots$$

$$G^{\mathrm{P}}_{\mathrm{SAF}}(T,\delta+\Delta\delta) + \frac{\Delta\delta}{2}G_{\mathrm{O_{2(g)}}}(T,p_{\mathrm{O_2}}) - G^{\mathrm{P}}_{\mathrm{SAF}}(T,\delta) \tag{C.19}$$

Determining the Gibbs free energy of SAF as a function of temperature, pressure and nonstoichiometry may be achieved by applying the equilibrium nonstoichiometry measurements to the definition of chemical equilibrium at a constant temperature and pressure [167]. At chemical equilibrium, the total Gibbs free energy of a system is constrained by:

$$dG\big|_{\mathrm{T,p}} = 0 \tag{C.20}$$

where G, the *extensive* total SAF-O_2 redox system Gibbs free energy is:

$$\begin{aligned} G(T,p) &= \sum_i n_i \bar{G}_i \\ &= \sum_i n_i\,^{\circ}\bar{G}_i + \sum_i n_i RT \ln p_i \\ &= n_{\mathrm{SAF}}\bar{G}_{\mathrm{SAF}}(T,\delta) + n_{\mathrm{O_2}}\,^{\circ}\bar{G}_{\mathrm{O_2}}(T) + n_{\mathrm{O_2}}RT \ln p_{\mathrm{O_2}} \end{aligned} \tag{C.21}$$

where $\bar{G}$ notation, previously neglected, is used from here forward to emphasize that the Gibbs functions are on a molar basis. The Gibbs free energy of SAF is only a function of T and δ and does not have an $RT\ln$ term, as it is a solid phase, and any crystalline mixing/entropic terms are already captured within G_{SAF} by the compound energy formalism.

The definition of the Gibbs free energy may be applied to the reaction balance to obtain the differential of the SAF Gibbs function at equilibrium, given as:

$$
\begin{aligned}
dG\big|_{T,p} = {} & dn_{\text{SAF}}\bar{G}_{\text{SAF}}(T,\delta) + n_{\text{SAF}}d\bar{G}_{\text{SAF}}(T,\delta) + \dots \\
& dn_{O_2}{}^{\circ}\bar{G}_{O_2}(T) + d{}^{\circ}\bar{G}_{O_2}(T) + \dots \\
& dn_{O_2}RT\ln p_{O_2} + n_{O_2}R\,\cancelto{0}{dT}\ln p_{O_2} + n_{O_2}RTd\left(\ln p_{O_2}\right) \\
= {} & 0
\end{aligned}
\tag{C.22}
$$

Applying the definition of a total differential of a function of one or more variables produces:

$$
\begin{aligned}
dG\big|_{T,p} = {} & \bar{G}_{\text{SAF}}(T,\delta)\,dn_{\text{SAF}} + \dots \\
& n_{\text{SAF}}\left[\frac{\partial \bar{G}_{\text{SAF}}}{\partial T}\cancelto{0}{dT} + \frac{\partial \bar{G}_{\text{SAF}}}{\partial \delta}\,d\delta\right] + \dots \\
& \left[{}^{\circ}\bar{G}_{O_2}(T) + RT\ln p_{O_2}\right]dn_{O_2} + \left[\frac{\partial {}^{\circ}\bar{G}_{O_2}}{\partial T}\cancelto{0}{dT}\right] + \dots \\
& n_{O_2}RT\left[\frac{1}{p}\frac{\partial p}{\partial p}\cancelto{0}{dp}\right] \\
= {} & 0
\end{aligned}
\tag{C.23}
$$

which highlights two characteristics of SAF which differ from stoichiometric materials: 1) the Gibbs free energy of SAF is not just a function of temperature but δ, and 2) as SAF reacts, the number of moles is unchanged, even as the number of atoms per formula unit varies as δ becomes smaller/larger. While this may at first appearance seem to violate conservation of mass, it is actually consistent, which can be more clearly demonstrated by dividing each term of the equation by $d\delta$:

$$\bar{G}_{SAF}\left(T,\delta\right)\frac{dn_{SAF}}{d\delta}^{0}+\frac{\partial\bar{G}_{SAF}}{\partial\delta}+\ldots$$

$$\left[\,^{\circ}\bar{G}_{O_2}\left(T\right)+RT\ln p_{O_2}\right]n_{SAF}\frac{dn_{O_2}}{d\delta}^{\frac{1}{2}}=0 \tag{C.24}$$

While n_{SAF} does not change with δ, n_{O2} does at a rate of 0.5 mol O_2 per unit change in δ of 1 mol SAF. The definition then simplifies to:

$$\frac{\partial\bar{G}_{SAF}}{\partial\delta}=-\frac{1}{2}\left[\,^{\circ}\bar{G}_{O_2}\left(T\right)+RT\ln p_{O_2}\right] \tag{C.25}$$

or, in differential form for the fixed T and p:

$$d\bar{G}_{SAF}\Big|_{T,p}=-\frac{1}{2}\left[\,^{\circ}\bar{G}_{O_2}\left(T\right)+RT\ln p_{O_2}\right]d\delta \tag{C.26}$$

which may be estimated via a central difference approximation for numerical fitting:

$$\bar{G}_{SAF}\left(T,\delta^+\right)-\bar{G}_{SAF}\left(T,\delta^-\right)=-\frac{\left(\delta^+-\delta^-\right)}{2}\left[\,^{\circ}\bar{G}_{O_2}\left(T\right)+RT\ln p_{O_2}\right] \tag{C.27}$$

where δ^+ and δ^- are an experimentally-measured δ perturbed by some small $\pm\Delta\delta$ in order to approximate the differential at that point.

REFERENCES

1. Schieber, G.L., et al., *H_2O splitting via a two-step solar thermoelectrolytic cycle based on non-stoichiometric ceria redox reactions: Thermodynamic analysis.* International Journal of Hydrogen Energy, 2017. **42**(30): p. 18785-18793.

2. Muroyama, A., et al., *Modeling of a Dynamically-Controlled Hybrid Solar/Autothermal Steam Gasification Reactor.* Energy & Fuels, 2014. **28**(10): p. 6520-6530.

3. Muroyama, A.P., et al., *Design and demonstration of a prototype 1.5 kW_{th} hybrid solar/autothermal steam gasifier.* Fuel, 2018. **211**: p. 331-340.

4. Muroyama, A.P. and P.G. Loutzenhiser, *Kinetic Analyses of Gasification and Combustion Reactions of Carbonaceous Feedstocks for a Hybrid Solar/Autothermal Gasification Process To Continuously Produce Synthesis Gas.* Energy & Fuels, 2016. **30**(5): p. 4292-4299.

5. Loutzenhiser, P.G., O. Tuerk, and A. Steinfeld, *Production of Si by vacuum carbothermal reduction of SiO_2 using concentrated solar energy.* JOM, 2010. **62**(9): p. 49-54.

6. Steinfeld, A., P. Kuhn, and J. Karni, *High-temperature solar thermochemistry: Production of iron and synthesis gas by Fe_3O_4-reduction with methane.* Energy, 1993. **18**(3): p. 239-249.

7. Wang, K., Q. Yu, and Q. Qin, *The thermodynamic method for selecting oxygen carriers used for chemical looping air separation.* Journal of Thermal Analysis and Calorimetry, 2013. **112**(2): p. 747-753.

8. Meredig, B. and C. Wolverton, *First-principles thermodynamic framework for the evaluation of thermochemical H_2O- or CO_2-splitting materials.* Physical Review B, 2009. **80**(24): p. 245119.

9. Wong, B., *Thermochemical Heat Storage for Concentrated Solar Power, Final Report for the US Department of Energy.* 2011: San Diego, CA, USA.

10. McDaniel, A.H., et al., *Nonstoichiometric Perovskite Oxides for Solar Thermochemical H_2 and CO Production.* Energy Procedia, 2014. **49**(0): p. 2009-2018.

11. Parida, B., S. Iniyan, and R. Goic, *A review of solar photovoltaic technologies.* Renewable and Sustainable Energy Reviews, 2011. **15**(3): p. 1625-1636.

12. Zhang, H.L., et al., *Concentrated solar power plants: Review and design methodology.* Renewable and Sustainable Energy Reviews, 2013. **22**: p. 466-481.

13.   Ho, C.K. and B.D. Iverson, *Review of high-temperature central receiver designs for concentrating solar power.* Renewable and Sustainable Energy Reviews, 2014. **29**: p. 835-846.

14.   Steinfeld, A., *Solar thermochemical production of hydrogen—a review.* Solar Energy, 2005. **78**(5): p. 603-615.

15.   Loutzenhiser, P.G., A. Meier, and A. Steinfeld, *Review of the Two-Step H_2O/CO_2-Splitting Solar Thermochemical Cycle Based on Zn/ZnO Redox Reactions.* Materials, 2010. **3**(11): p. 4922-4938.

16.   Miller, J.E., et al., *Advancing Oxide Materials for Thermochemical Production of Solar Fuels.* Energy Procedia, 2014. **49**(0): p. 2019-2026.

17.   Agrafiotis, C., M. Roeb, and C. Sattler, *A review on solar thermal syngas production via redox pair-based water/carbon dioxide splitting thermochemical cycles.* Renewable & Sustainable Energy Reviews, 2015. **42**: p. 254-285.

18.   Dry, M.E., *The Fischer–Tropsch process: 1950–2000.* Catalysis Today, 2002. **71**(3–4): p. 227-241.

19.   Schrader, A.J., A.P. Muroyama, and P.G. Loutzenhiser, *Solar electricity via an Air Brayton cycle with an integrated two-step thermochemical cycle for heat storage based on Co_3O_4/CoO redox reactions: Thermodynamic analysis.* Solar Energy, 2015. **118**: p. 485-495.

20.   Carrillo, A.J., et al., *Thermochemical heat storage based on the Mn_2O_3/Mn_3O_4 redox couple: influence of the initial particle size on the morphological evolution and cyclability.* Journal of Materials Chemistry A, 2014. **2**(45): p. 19435-19443.

21.   Pagkoura, C., et al., *Cobalt oxide based structured bodies as redox thermochemical heat storage medium for future CSP plants.* Solar Energy, 2014. **108**: p. 146-163.

22.   Loutzenhiser, P.G., et al., *CO2 Splitting via Two-Step Solar Thermochemical Cycles with Zn/ZnO and FeO/Fe_3O_4 Redox Reactions II: Kinetic Analysis.* Energy & Fuels, 2009. **23**(5): p. 2832-2839.

23.   Muroyama, A.P., A.J. Schrader, and P.G. Loutzenhiser, *Solar electricity via an Air Brayton cycle with an integrated two-step thermochemical cycle for heat storage based on Co_3O_4/CoO redox reactions II: Kinetic analyses.* Solar Energy, 2015. **122**: p. 409-418.

24.   Abu Hamed, T., et al., *Study of a Quench Device for the Synthesis and Hydrolysis of Zn Nanoparticles: Modeling and Experiments.* Journal of Solar Energy Engineering, 2009. **131**(3): p. 9.

25. Agrafiotis, C., et al., *Exploitation of thermochemical cycles based on solid oxide redox systems for thermochemical storage of solar heat. Part 1: Testing of cobalt oxide-based powders.* Solar Energy, 2014. **102**: p. 189-211.

26. Hutchings, K.N., et al., *Kinetic and thermodynamic considerations for oxygen absorption/desorption using cobalt oxide.* Solid State Ionics, 2006. **177**(1): p. 45-51.

27. Neises, M., et al., *Solar-heated rotary kiln for thermochemical energy storage.* Solar Energy, 2012. **86**(10): p. 3040-3048.

28. Alonso, E., et al., *Kinetics of Mn_2O_3–Mn_3O_4 and Mn_3O_4–MnO Redox Reactions Performed under Concentrated Thermal Radiative Flux.* Energy & Fuels, 2013. **27**(8): p. 4884-4890.

29. Alonso, E., et al., *First experimental studies of solar redox reactions of copper oxides for thermochemical energy storage.* Solar Energy, 2015. **115**: p. 297-305.

30. Deutsch, M., et al., *High-Temperature Energy Storage: Kinetic Investigations of the CuO/Cu_2O Reaction Cycle.* Energy & Fuels, 2017. **31**(3): p. 2324-2334.

31. Haseli, P., M. Jafarian, and G.J. Nathan, *High temperature solar thermochemical process for production of stored energy and oxygen based on CuO/Cu_2O redox reactions.* Solar Energy, 2017. **153**: p. 1-10.

32. Bowrey, R.G. and J. Jutsen, *Energy storage using the reversible oxidation of barium oxide.* Solar Energy, 1978. **21**(6): p. 523-525.

33. Carrillo, A.J., et al., *Revisiting the BaO_2/BaO redox cycle for solar thermochemical energy storage.* Physical Chemistry Chemical Physics, 2016. **18**(11): p. 8039-8048.

34. Imponenti, L., et al., *Thermochemical energy storage in strontium-doped calcium manganites for concentrating solar power applications.* Solar Energy, 2017. **151**: p. 1-13.

35. Babiniec, S.M., et al., *Investigation of $La_xSr_{1-x}Co_yM_{1-y}O_{3-\delta}$ (M = Mn, Fe) perovskite materials as thermochemical energy storage media.* Solar Energy, 2015. **118**: p. 451-459.

36. Babiniec, S.M., et al., *Doped calcium manganites for advanced high-temperature thermochemical energy storage.* International Journal of Energy Research, 2016. **40**(2): p. 280-284.

37. Zhang, Z., L. Andre, and S. Abanades, *Experimental assessment of oxygen exchange capacity and thermochemical redox cycle behavior of Ba and Sr series perovskites for solar energy storage.* Solar Energy, 2016. **134**: p. 494-502.

38.   Schrader, A.J., et al., *Solar electricity via an Air Brayton cycle with an integrated two-step thermochemical cycle for heat storage based on Co₃O₄/CoO redox reactions III: Solar thermochemical reactor design and modeling.* Solar Energy, 2017. **150**: p. 584-595.

39.   SIGMA-ALDRICH, *Safety Data Sheet: Cobalt(II) oxide [1308-06-1].* 2017, Darmstadt, Germany: Sigma-Aldrich, Inc.

40.   Steinfeld, A. and R. Palumbo, *Solar thermochemical process technology.* Encyclopedia of physical science and technology, 2001. **15**(1): p. 237-56.

41.   Smith, K.S. and H.L. Huyck, *An overview of the abundance, relative mobility, bioavailability, and human toxicity of metals.* The environmental geochemistry of mineral deposits, 1999. **6**: p. 29-70.

42.   Steinfeld, A. and E.A. Fletcher, *Theoretical and Experimental Investigation of the Carbothermic Reduction of Fe₂O₃ using Solar-Energy.* Energy, 1991. **16**(7): p. 1011-1019.

43.   Steinfeld, A., A. Frei, and P. Kuhn, *Thermoanalysis of the combined Fe₃O₄-reduction and CH₄-reforming processes.* Metallurgical and Materials Transactions B, 1995. **26**(3): p. 509-515.

44.   Tamaura, T., et al., *The Solar-Driven Coal/Fe₃O₄ Redox System.* J. Phys. IV France, 1997. **07**(C1): p. C1-685-C1-686.

45.   Halmann, M. and A. Steinfeld, *Fuel saving, carbon dioxide emission avoidance, and syngas production by tri-reforming of flue gases from coal- and gas-fired power stations, and by the carbothermic reduction of iron oxide.* Energy, 2006. **31**(15): p. 3171-3185.

46.   Galvez, M., et al., *CO2 splitting via two-step solar thermochemical cycles with Zn/ZnO and FeO/Fe₃O₄ redox reactions: thermodynamic analysis.* Energy & Fuels, 2008. **22**(5): p. 3544-3550.

47.   Nakamura, T., *Hydrogen production from water utilizing solar heat at high temperatures.* Solar Energy, 1977. **19**(5): p. 467-475.

48.   Sibieude, F., et al., *High temperature experiments with a solar furnace: The decomposition of Fe₃O₄, Mn₃O₄, CdO.* International Journal of Hydrogen Energy, 1982. **7**(1): p. 79-88.

49.   Stamatiou, A., P.G. Loutzenhiser, and A. Steinfeld, *Solar Syngas Production via H₂O/CO₂-Splitting Thermochemical Cycles with Zn/ZnO and FeO/Fe₃O= Redox Reactions.* Chemistry of Materials, 2010. **22**(3): p. 851-859.

50. Block, T., N. Knoblauch, and M. Schmücker, *The cobalt-oxide/iron-oxide binary system for use as high temperature thermochemical energy storage material.* Thermochimica Acta, 2014. **577**(Supplement C): p. 25-32.

51. Block, T. and M. Schmücker, *Metal oxides for thermochemical energy storage: A comparison of several metal oxide systems.* Solar Energy, 2016. **126**(Supplement C): p. 195-207.

52. André, L., S. Abanades, and L. Cassayre, *High-temperature thermochemical energy storage based on redox reactions using Co-Fe and Mn-Fe mixed metal oxides.* Journal of Solid State Chemistry, 2017. **253**(Supplement C): p. 6-14.

53. Smith, A.R. and J. Klosek, *A review of air separation technologies and their integration with energy conversion processes.* Fuel Processing Technology, 2001. **70**(2): p. 115-134.

54. Grande, C.A., *Advances in pressure swing adsorption for gas separation.* ISRN Chemical Engineering, 2012. **2012**.

55. Kosinov, N., et al., *Recent developments in zeolite membranes for gas separation.* Journal of Membrane Science, 2016. **499**: p. 65-79.

56. Murali, R.S., T. Sankarshana, and S. Sridhar, *Air Separation by Polymer-based Membrane Technology.* Separation & Purification Reviews, 2013. **42**(2): p. 130-186.

57. Modak, J.M., *Haber process for ammonia synthesis.* Resonance, 2002. **7**(9): p. 69-77.

58. Snyder, C.S., et al., *Review of greenhouse gas emissions from crop production systems and fertilizer management effects.* Agriculture, Ecosystems & Environment, 2009. **133**(3): p. 247-266.

59. Steinfeld, A., et al., *Solar-processed metals as clean energy carriers and water-splitters.* International Journal of Hydrogen Energy, 1998. **23**(9): p. 767-774.

60. Bush, H.E. and P.G. Loutzenhiser, *Solar electricity via an Air Brayton cycle with an integrated two-step thermochemical cycle for heat storage based on Fe_2O_3/Fe_3O_4 redox reactions: Thermodynamic and kinetic analyses.* Solar Energy, 2018. **174**: p. 617-627.

61. Brendelberger, S., et al., *Vacuum pumping options for application in solar thermochemical redox cycles – Assessment of mechanical-, jet- and thermochemical pumping systems.* Solar Energy, 2017. **141**: p. 91-102.

62. Moghtaderi, B., *Application of Chemical Looping Concept for Air Separation at High Temperatures.* Energy & Fuels, 2010. **24**(1): p. 190-198.

63.   Ezbiri, M., et al., *Design Principles of Perovskites for Thermochemical Oxygen Separation.* ChemSusChem, 2015. **8**(11): p. 1966-1971.

64.   Vieten, J., et al., *Perovskite oxides for application in thermochemical air separation and oxygen storage.* Journal of Materials Chemistry A, 2016. **4**(35): p. 13652-13659.

65.   Bulfin, B., et al., *Redox chemistry of $CaMnO_3$ and $Ca_{0.8}Sr_{0.2}MnO_3$ oxygen storage perovskites.* Journal of Materials Chemistry A, 2017. **5**(17): p. 7912-7919.

66.   Mizusaki, J., *Nonstoichiometry, diffusion, and electrical properties of perovskite-type oxide electrode materials.* Solid State Ionics, 1992. **52**(1): p. 79-91.

67.   Falcón, H., et al., *$SrFeO_{3-\delta}$ Perovskite Oxides: Chemical Features and Performance for Methane Combustion.* Chemistry of Materials, 2002. **14**(5): p. 2325-2333.

68.   Marek, E., et al., *The use of strontium ferrite in chemical looping systems.* Applied Energy, 2018. **223**: p. 369-382.

69.   Xiao, G., et al., *Synthesis and characterization of Mo-doped $SrFeO_{3-\delta}$ as cathode materials for solid oxide fuel cells.* Journal of Power Sources, 2012. **202**: p. 63-69.

70.   Vieten, J., et al., *Redox thermodynamics and phase composition in the system $SrFeO_{3-\delta}$ — $SrMnO_{3-\delta}$.* Solid State Ionics, 2017. **308**: p. 149-155.

71.   Vieten, J., et al., *Redox Behavior of Solid Solutions in the $SrFe_{1-x}Cu_xO_{3-\delta}$ System for Application in Thermochemical Oxygen Storage and Air Separation.* Energy Technology, 2018. **0**(0).

72.   Van Roosmalen, J.A.M. and E.H.P. Cordfunke, *A new defect model to describe the oxygen deficiency in perovskite-type oxides.* Journal of Solid State Chemistry, 1991. **93**(1): p. 212-219.

73.   Yoo, J., et al., *Determination of oxygen nonstoichiometry in $SrFeO_{3-\delta}$ by solid-state Coulometric titration.* Journal of the American Ceramic Society, 2017. **100**(6): p. 2690-2699.

74.   Diethelm, S., A. Closset, and K. Nisancioglu, *Oxygen transport and nonstoichiometry in $SrFeO_{3-\delta}$.* Electrochemistry-Tokyo-, 2000. **68**(EPFL-ARTICLE-166896): p. 444-450.

75.   Bakken, E., et al., *Redox energetics of $SrFeO_{3-\delta}$ — a coulometric titration study.* Solid State Ionics, 2004. **167**(3): p. 367-377.

76.   Lankhorst, M.H.R., H.J.M. Bouwmeester, and H. Verweij, *Thermodynamics and Transport of Ionic and Electronic Defects in Crystalline Oxides.* Journal of the American Ceramic Society, 1997. **80**(9): p. 2175-2198.

77.   Bucher, E. and W. Sitte, *Defect Chemical Modeling of (La, Sr)(Co, Fe)O₃ ₋ δ.* Journal of Electroceramics, 2004. **13**(1): p. 779-784.

78.   Hillert, M., *The compound energy formalism.* Journal of Alloys and Compounds, 2001. **320**(2): p. 161-176.

79.   Grundy, A.N., et al., *Calculation of defect chemistry using the CALPHAD approach.* Calphad, 2006. **30**(1): p. 33-41.

80.   Bork, A.H., E. Povoden-Karadeniz, and J.L.M. Rupp, *Modeling Thermochemical Solar-to-Fuel Conversion: CALPHAD for Thermodynamic Assessment Studies of Perovskites, Exemplified for (La,Sr)MnO₃.* Advanced Energy Materials, 2017. **7**(1): p. 1601086.

81.   Zinkevich, M., D. Djurovic, and F. Aldinger, *Thermodynamic modelling of the cerium–oxygen system.* Solid State Ionics, 2006. **177**(11): p. 989-1001.

82.   Djurovic, D., M. Zinkevich, and F. Aldinger, *Thermodynamic modeling of the cerium–yttrium–oxygen system.* Solid State Ionics, 2008. **179**(33): p. 1902-1911.

83.   Schunk, L.O. and A. Steinfeld, *Kinetics of the Thermal Dissociation of ZnO Exposed to Concentrated Solar Irradiation Using a Solar-Driven Thermogravimeter in the 1800-2100 K Range.* Aiche Journal, 2009. **55**(6): p. 1497-1504.

84.   Takacs, M., et al., *Splitting CO₂ with a ceria-based redox cycle in a solar-driven thermogravimetric analyzer.* AIChE Journal, 2017. **63**(4): p. 1263-1271.

85.   Scheffe, J.R., et al., *Kinetics and mechanism of solar-thermochemical H₂ production by oxidation of a cobalt ferrite-zirconia composite.* Energy & Environmental Science, 2013. **6**(3): p. 963-973.

86.   Alonso, E. and M. Romero, *A directly irradiated solar reactor for kinetic analysis of non-volatile metal oxides reductions.* International Journal of Energy Research, 2015. **39**(9): p. 1217-1228.

87.   Modest, M.F., *Radiative Heat Transfer.* 3rd ed. 2013, Oxford, UK: Academic Press. 882.

88.   Neumann, A., *Procedures for flux measurements for solar receivers using video cameras and Lambertian targets.* SolarPACES, 1997. **3**(3): p. 213-225.

89.   Erickson, B. and J. Petrasch, *Inverse identification of intensity distributions from multiple flux maps in concentrating solar applications*, in *Eurotherm Conference No. 95: Computational Thermal Radiation in Participating Media IV, 18-20 April 2012*. 2012, IOP Publishing Ltd.: UK. p. 012014 (10 pp.).

90.   Gardon, R., *An instrument for the direct measurement of intense thermal radiation.* Review of Scientific Instruments, 1953. **24**: p. 366-370.

91.   Ballestrin, J., et al., *Heat flux sensors: Calorimeters or radiometers?* Solar Energy, 2006. **80**(10): p. 1314-20.

92.   Ballestrin, J., et al., *Systematic error in the measurement of very high solar irradiance.* Solar Energy Materials and Solar Cells, 2003. **80**(3): p. 375-81.

93.   Ballestrin, J., et al., *High-heat-flux sensor calibration using calorimetry.* Metrologia, 2004. **41**(4): p. 314-18.

94.   Alxneit, I. and H. Schmit, *Spectral Characterization of PSI's High-Flux Solar Simulator.* Journal of Solar Energy Engineering, 2012. **134**(1): p. 011013 (5 pp.).

95.   Blackmon, J.B., *Development and Performance of a Digital Image Radiometer for Heliostat Evaluation at Solar One.* Journal of Solar Energy Engineering, 1985. **107**(4): p. 315-321.

96.   Ballestrín, J. and R. Monterreal, *Hybrid heat flux measurement system for solar central receiver evaluation.* Energy, 2004. **29**(5–6): p. 915-924.

97.   Johnston, G., *Focal region measurements of the 20 m^2 tiled dish at the Australian National University.* Solar Energy, 1998. **63**(2): p. 117-24.

98.   Jaramillo, O.A., et al., *A flat-plate calorimeter for concentrated solar flux evaluation.* Renewable Energy, 2008. **33**(10): p. 2322-2328.

99.   Estrada, C.A., et al., *Heat transfer analysis in a calorimeter for concentrated solar radiation measurements.* Solar Energy, 2007. **81**(10): p. 1306-13.

100.   Groer, U. and A. Neumann, *Development and test of a high flux calorimeter at DLR Cologne.* Journal De Physique. IV : JP, 1999. **9**(3): p. Pr3-643 - Pr3-648.

101.   Modest, M.F., *Radiative Heat Transfer.* 2nd ed. 2003, San Diego: Academic Press. 822.

102.   Alxneit, I., *Error analysis of the radiative power determined from flux distributions measured with a camera in a Xe arc lamp-based solar simulator.* Journal of Solar Energy Engineering, Transactions of the ASME, 2012. **134**(4).

103.   Estrada, C.A., et al. *Experiments with CAVICAL in the solar furnace of the PSA.* in *ISES Solar World Congress 2007. Solar Energy and Human Settlement, 18-21 Sept. 2007.* 2007. Berlin, Germany: Springer-Verlag.

104.   Ulmer, S., et al., *Beam characterization and improvement with a flux mapping system for dish concentrators.* Transactions of the ASME. Journal of Solar Energy Engineering, 2002. **124**(2): p. 182-8.

105. Ho, C.K. and S.S. Khalsa, *A photographic flux mapping method for concentrating solar collectors and receivers.* Journal of Solar Energy Engineering, Transactions of the ASME, 2012. **134**(4).

106. ANSYS, *ANSYS Fluent*. 2017, ANSYS, Inc.: Canonsburg, PA.

107. Mecit, A.M.M., F., *A Comparison Between the Monte Carlo Ray Trace and the FLUENT Discrete Ordinates Methods for Treating Solar Input to a Particle Receiver.* ASME 2014 8th International Conference on Energy Sustainability collocated with the ASME 2014 12th International Conference on Fuel Cell Science, Engineering and Technology, 2014. Volume 1: Combined Energy Cycles, CHP, CCHP, and Smart Grids; Concentrating Solar Power, Solar Thermochemistry and Thermal Energy Storage; Geothermal, Ocean, and Emerging Energy Technologies; Hydrogen Energy Technologies; Low/Zero Emission Power Plants and Carbon Sequestration; Photovoltaics; Wind Energy Systems and Technologies: p. V001T02A013.

108. Craig, K.J., et al., *Finite-volume ray tracing using Computational Fluid Dynamics in linear focus CSP applications.* Appl. Energ., 2016. **183**: p. 241-256.

109. Wang, F., et al., *Thermal performance analyses of porous media solar receiver with different irradiative transfer models.* International Journal of Heat and Mass Transfer, 2014. **78**: p. 7-16.

110. Bush, H.E., et al., *Design and Characterization of a Novel Upward Flow Reactor for the Study of High-Temperature Thermal Reduction for Solar-Driven Processes.* Journal of Solar Energy Engineering, 2017. **139**(5): p. 051004-051004-11.

111. Qiu, Y., et al., *A comprehensive model for opitcal and thermal characterization of a linear Fresnel solar reflector with a trapezoidal cavity receiver.* Renewable Energy, 2016. **97**: p. 129-144.

112. Qiu, Y., et al., *Study on optical and thermal perforamance of a linear Fresnel solar reflector using molten salt as HTF with MCRT and FVM methods.* Appl. Energ., 2015. **146**: p. 162-173.

113. He, Y.-L., et al., *A MCRT and FVM coupled simulation method for energy conversion process in parabolic trough solar collector.* Renewable Energy, 2010. **36**: p. 976-985.

114. Lapp, J., J.H. Davidson, and W. Lipiński, *Heat Transfer Analysis of a Solid-Solid Heat Recuperation System for Solar-Driven Nonstoichiometric Redox Cycles.* Journal of Solar Energy Engineering, 2013. **135**(3): p. 031004-031004-11.

115. Koepf, E., et al., *A novel beam-down, gravity-fed, solar thermochemical receiver/reactor for direct solid particle decomposition: Design, modeling, and experimentation.* International Journal of Hydrogen Energy, 2012. **37**(22): p. 16871-16887.

116. Furler, P., et al., *Solar Thermochemical CO$_2$ Splitting Utilizing a Reticulated Porous Ceria Redox System.* Energy & Fuels, 2012. **26**(11): p. 7051-7059.

117. MathWorks, *Camera Calibrator: Estimate camera intrinsic and extrinsic parameters.* 2013.

118. MathWorks, *extrinsics: Compute location of calibrated camera.* 2014.

119. MathWorks, *imwarp: Apply geometric transformation to image.*

120. Petrasch, J. *A free and open source Monte Carlo ray tracing program for concentrating solar energy research.* in *ASME 2010 4th International Conference on Energy Sustainability, ES 2010, May 17, 2010 - May 22, 2010.* 2010. Phoenix, AZ, United states: American Society of Mechanical Engineers.

121. Gill, R., et al., *Characterization of a 6 kW high-flux solar simulator with an array of xenon arc lamps capable of concentrations of nearly 5000 suns.* Review of Scientific Instruments, 2015. **86**(12): p. 8.

122. Ghiassiaan, S.M., *Convective Heat and Mass Transfer.* 1st ed. 2011, New York: Cambridge University Press. 524.

123. MathWorks, *fminsearch: Find minimum of unconstrained multivariable function using derivative-free method.* 2006.

124. Müller, R. and A. Steinfeld, *Band-approximated radiative heat transfer analysis of a solar chemical reactor for the thermal dissociation of zinc oxide.* Solar Energy, 2007. **81**(10): p. 1285-1294.

125. *ANSYS Fluent.* 2013, ANSYS, Inc.: Canonsburg, PA.

126. NETZSCH, *Operating Instructions: Simultaneous TG-DTA/DSC Apparatus, STA 449 F3 Jupiter.* p. 3.30.

127. Company, M.C.S., *Extreme-Chemical O-Ring FEP with Viton® Core.* 2015.

128. Schlichting, K.-P., *Parametric Study of the Temperature Distribution of a Packed-Bed Subjected to Concentrated Irradiation*, in *Department of Mechanical Engineering.* 2015, Eidgenössische Technische Hochschule Zürich (Swiss Federal Institute of Technology). p. 142.

129. Gill, R., et al., *Characterization of a 6 kW high-flux solar simulator with an array of xenon arc lamps capable of concentrations of nearly 5000 suns.* Review of Scientific Instruments, 2015. **86**(12): p. 125107.

130. Andraka, C.E., et al., *Rapid Reflective Facet Characterization Using Fringe Reflection Techniques.* J Sol Energ, 2014. **136**(1).

131.   Smith, D., E. Shiles, and M. Inokuti, *The optical properties of metallic aluminum*. Handbook of optical constants of solids. Vol. 1. 1985, Cambridge, Massachusetts: Academic Press. 369-406.

132.   Products, T.G. *Fused Quartz Average Transmittance Curves*. Available from: https://www.technicalglass.com/fused_quartz_transmission.html.

133.   *tricobalt tetraoxide*. Chemistry WebBook, 2016.

134.   Tsotsas, E. and H. Martin, *Thermal conductivity of packed beds: A review*. Chemical Engineering and Processing: Process Intensification, 1987. **22**(1): p. 19-37.

135.   Kim, S.J. and S.P. Jang, *Effects of the Darcy number, the Prandtl number, and the Reynolds number on local thermal non-equilibrium*. International Journal of Heat and Mass Transfer, 2002. **45**(19): p. 3885-3896.

136.   Singh, B.P. and M. Kaviany, *Modelling radiative heat transfer in packed beds*. International Journal of Heat and Mass Transfer, 1992. **35**(6): p. 1397-1405.

137.   Zehner, P. and E.U. Schlünder, *Einfluß der Wärmestrahlung und des Druckes auf den Wärmetransport in nicht durchströmten Schüttungen*. Chemie Ingenieur Technik, 1972. **44**(23): p. 1303-1308.

138.   Sahoo, P., H. Djieutedjeu, and P.F.P. Poudeu, *Co_3O_4 nanostructures: the effect of synthesis conditions on particles size, magnetism and transport properties*. Journal of Materials Chemistry A, 2013. **1**(47): p. 15022-15030.

139.   Lewis, F.B. and N.H. Saunders, *The thermal conductivity of NiO and CoO at the Neel temperature*. Journal of Physics C: Solid State Physics, 1973. **6**(15): p. 2525.

140.   Ghiaasiaan, S.M., *Convective Heat and Mass Transfer*. 1st ed. 2011, New York: Cambridge University Press. 524.

141.   LeFevre, E.J. *Laminar free convection from a vertical plane surface*. in *Proceedings of the 9th International Congress on Applied Mechanics*. 1956. Brussels.

142.   Cook, J.G. and M.P. van der Meer, *The optical properties of sputtered Co_3O_4 films*. Thin Solid Films, 1986. **144**(2): p. 165-176.

143.   Sumin Sih, S. and J.W. Barlow, *The Prediction of the Emissivity and Thermal Conductivity of Powder Beds*. Particulate Science and Technology, 2004. **22**(3): p. 291-304.

144.   Levenspiel, O., *Chemical Reaction Engineering*. 3rd ed. 1999: Wiley. 668.

145.   MathWorks, *fft: Fast Fourier Transform*. 2016.

146. Linstrom, P.J. and W.G. Mallard, *The NIST Chemistry WebBook: A Chemical Data Resource on the Internet.* Journal of Chemical & Engineering Data, 2001. **46**(5): p. 1059-1063.

147. Gorman, B.T., et al., *Thermodynamic Investigation of Concentrating Solar Power With Thermochemical Storage.* 2015(56840): p. V001T05A026.

148. Alper, J.S. and R.I. Gelb, *Standard errors and confidence intervals in nonlinear regression: comparison of Monte Carlo and parametric statistics.* Journal of Physical Chemistry, 1990. **94**(11): p. 4747-4751.

149. Vyazovkin, S., et al., *ICTAC Kinetics Committee recommendations for performing kinetic computations on thermal analysis data.* Thermochimica Acta, 2011. **520**(1): p. 1-19.

150. Friedman, H.L., *Kinetics of thermal degradation of char-forming plastics from thermogravimetry. Application to a phenolic plastic.* Journal of Polymer Science Part C: Polymer Symposia, 1964. **6**(1): p. 183-195.

151. Kissinger, H.E., *Reaction Kinetics in Differential Thermal Analysis.* Analytical Chemistry, 1957. **29**(11): p. 1702-1706.

152. Tiernan, M.J., P.A. Barnes, and G.M.B. Parkes, *Reduction of Iron Oxide Catalysts: The Investigation of Kinetic Parameters Using Rate Perturbation and Linear Heating Thermoanalytical Techniques.* The Journal of Physical Chemistry B, 2001. **105**(1): p. 220-228.

153. Yu, J., et al., *Mechanism and Kinetics of the Reduction of Hematite to Magnetite with $CO–CO_2$ in a Micro-Fluidized Bed.* Minerals, 2017. **7**(11): p. 209.

154. Gallagher, K.J., W. Feitknecht, and U. Mannweiler, *Mechanism of Oxidation of Magnetite to γ-Fe2O3.* Nature, 1968. **217**(5134): p. 1118.

155. Feitknecht, W. and K.J. Gallagher, *Mechanisms for the Oxidation of Fe_3O_4.* Nature, 1970. **228**: p. 548.

156. SK Sahoo, K.A., AK Singh, BG Polke, KC Raha, *Characterization of γ- and α-Fe_2O_3 nano powders synthesized by emulsion precipitation-calcination route and rheological behaviour of α-Fe_2O_3.* International Journal of Engineering, Science and Technology, 2010. **2**(8): p. 118-126.

157. Shebanova, O.N. and P. Lazor, *Raman study of magnetite (Fe_3O_4): laser-induced thermal effects and oxidation.* Journal of Raman Spectroscopy, 2003. **34**(11): p. 845-852.

158. Parkinson, G.S., *Iron oxide surfaces.* Surface Science Reports, 2016. **71**(1): p. 272-365.

159.   Becker, K.D., V. von Wurmb, and F.J. Litterst, *Disorder and diffusional motion of cations in magnetite, $Fe_{3-\delta}O_4$, studied by Mössbauer spectroscopy at high temperatures.* Journal of Physics and Chemistry of Solids, 1993. **54**(8): p. 923-935.

160.   Sidhu, P.S., R.J. Gilkes, and A.M. Posner, *Mechanism of the low temperature oxidation of synthetic magnetites.* Journal of Inorganic and Nuclear Chemistry, 1977. **39**(11): p. 1953-1958.

161.   Papanastassiou, D. and G. Bitsianes, *Mechanisms and kinetics underlying the oxidation of magnetite in the induration of iron ore pellets.* Metallurgical Transactions, 1973. **4**(2): p. 487-496.

162.   Monazam, E.R., R.W. Breault, and R. Siriwardane, *Kinetics of Magnetite (Fe_3O_4) Oxidation to Hematite (Fe_2O_3) in Air for Chemical Looping Combustion.* Industrial & Engineering Chemistry Research, 2014. **53**(34): p. 13320-13328.

163.   ICDD, *PDF-4+ 2016*. 2016, International Centre for Diffraction Data: Newtown Square, PA, USA.

164.   Vieten, J., et al., *Citric acid auto-combustion synthesis of Ti-containing perovskites via aqueous precursors.* Solid State Ionics, 2018. **315**: p. 92-97.

165.   Redlich, O. and A.T. Kister, *Algebraic Representation of Thermodynamic Properties and the Classification of Solutions.* Industrial & Engineering Chemistry, 1948. **40**(2): p. 345-348.

166.   Merkulov, O.V., et al., *Oxygen nonstoichiometry and defect chemistry of perovskite-structured $SrFe_{1-x}Mo_xO_{3-\delta}$ solid solutions.* Solid State Ionics, 2016. **292**: p. 116-121.

167.   Moran, M.J., H.N. Shapiro, and D.D. Boettner, *Fundamentals of Engineering Thermodynamics, 7th Edition*. 2010: Wiley Global Education.